

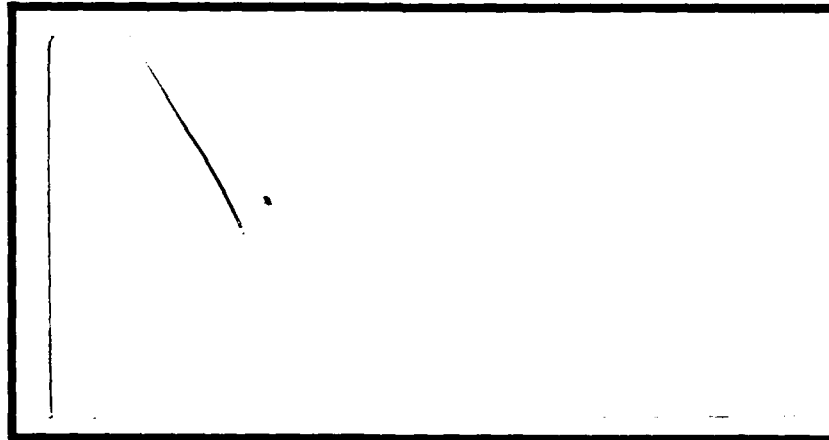
FILE COPY

①

AD-A202 663



DTIC  
 ELECTE  
 JAN 17 1989  
 S D  
 CS D



**DISTRIBUTION STATEMENT**  
 Approved for public release;  
 Distribution Unlimited

DEPARTMENT OF THE AIR FORCE  
 AIR UNIVERSITY

**AIR FORCE INSTITUTE OF TECHNOLOGY**

Wright-Patterson Air Force Base, Ohio

89 1 17 124

AFIT/GSO/ENP/88D-4

AN ANALYSIS OF PLATINUM SILICIDE AND  
INDIUM ANTIMONIDE FOR REMOTE SENSORS  
IN  
THE 3 TO 5 MICROMETER WAVELENGTH BAND

THESIS

Neil F. Schoon  
Captain, USAF  
AFIT/GSO/ENP/88D-4

Approved for public release; distribution unlimited

1

SEARCHED  
SERIALIZED  
INDEXED  
FILED

S

D.  
a

AFIT/GSO/ENP/88D-4

AN ANALYSIS OF PLATINUM SILICIDE AND  
INDIUM ANTIMONIDE FOR REMOTE SENSORS IN  
THE 3 TO 5 MICROMETER WAVELENGTH BAND

THESIS

Presented to the Faculty of the School of Engineering  
of the Air Force Institute of Technology  
Air University  
In Partial Fulfillment of  
Master of Science in Space Operations

Neil F. Schoon, B. S.  
Captain, USAF

December 1988

Accession For	
NTIS CP-61	J
DTIC 115	13
University of	11
J. S. ...	
By	
Date	
Date	
A-1	

Approved for public release; distribution unlimited

### Acknowledgements

This thesis would have been much more difficult to finish without the assistance of several people. First, a heartfelt thank you goes to my faculty advisor, Major James Lange, for the guidance and insight he has provided during the past six months of research. Thanks also go to Colonel Matthew Nichols for the confidence he showed in me. Finally, and most important, I thank my wife, [REDACTED] and [REDACTED] sons, [REDACTED] for the love, understanding, and cooperation they showed and without which I would never have finished this research.

Neil Schoon

## Table of Contents

	Page
Acknowledgements .....	ii
List of Figures .....	v
List of Tables .....	viii
Abstract .....	ix
I. Introduction .....	1
II. Background .....	4
Remote Sensing .....	4
Infrared Spectrum .....	5
Thermal Radiation .....	6
Gaseous Radiation .....	12
Atmospheric Windows .....	12
Atmospheric Transmission Factors .....	16
Atmospheric Absorption .....	19
Atmospheric Scattering .....	20
Source Emissions .....	21
8 - 12 $\mu\text{m}$ Band .....	22
3 - 5 $\mu\text{m}$ Band .....	24
Detectors .....	26
Detector Materials .....	27
Indium Antimonide .....	28
Mercury Cadmium Telluride .....	28
Platinum Silicide .....	29
Iridium Silicide .....	30
Detector Types .....	30
Charge Coupled Devices .....	30
Schottky Barrier Detectors .....	32
III. Methodology .....	35
Quantum Efficiency .....	37
Target Spectral Emittance .....	38
Reflected Solar Energy .....	40
Target Thermal Emittance .....	41
Atmospheric Transmission .....	44
Scenarios .....	44
Baseline Scenario .....	44
Target Temperature Scenarios .....	45
Target Reflectance Scenarios .....	45
Atmospheric Scenarios .....	47

	Page
IV. Analysis of Results .....	52
Baseline Scenario .....	52
PtSi .....	52
InSb .....	54
PtSi vs InSb .....	56
288K Target Temperature Scenario .....	59
308K Target Temperature Scenario .....	60
-1 Standard Deviation Reflectance Scenario ....	61
+1 Standard Deviation Reflectance Scenario ....	62
Rural 5 Km Visibility Scenario .....	63
Urban 5 Km Visibility Scenario .....	64
Increased Humidity Scenario .....	64
V. Conclusions and Recommendations .....	67
Conclusions .....	67
Recommendations .....	69
Point Source Target .....	69
Actual Sensor .....	69
Noise .....	70
Appendix: Sensitivity Analysis Graphs .....	A1
Bibliography .....	BIB-1
Vita .....	VIT-1

## List of Figures

Figure	Page
1. Blackbody Radiation For T = 298K .....	8
2. Blackbody Radiation For T = 600K .....	9
3. Blackbody Radiation For T = 3000K .....	10
4. Blackbody Radiation For T = 6000K .....	11
5. Atmospheric Transmission For SWIR .....	13
6. Atmospheric Transmission For MWIR .....	15
7. Atmospheric Transmission For LWIR .....	17
8. Atmospheric Transmission For Extreme IR .....	18
9. Platinum Silicide Quantum Efficiency .....	39
10. Reflectance Data For 20 Coatings .....	43
11. Target Greybody and Reflected Solar Emittance .....	46
12. Atmospheric Transmission For Rural 5 Km Visibility vs Baseline .....	49
13. Atmospheric Transmission For Urban 5 Km Visibility vs Baseline .....	50
14. Atmospheric Transmission For Increased Humidity Profile vs Baseline .....	51
15. PtSi Baseline Scenario, Day vs Night (Both Curves Normalized To A Maximum Of 1.0) .....	53
16. InSb Baseline Scenario, Day vs Night .....	55
17. Day Baseline Scenario, PtSi vs InSb .....	57
18. Night Baseline Scenario, PtSi vs InSb .....	58
A1. PtSi 288K Scenario, Day vs Night .....	A2
A2. InSb 288K Scenario, Day vs Night .....	A3
A3. Day 288K Scenario, PtSi vs InSb .....	A4
A4. Night 288K Scenario, PtSi vs InSb .....	A5

	Page
A5. PtSi 308K Scenario, Day vs Night .....	A6
A6. InSb 308K Scenario, Day vs Night .....	A7
A7. Day 308K Scenario, PtSi vs InSb .....	A8
A8. Night 308K Scenario, PtSi vs InSb .....	A9
A9. PtSi -1 Standard Deviation Reflectance Scenario, Day vs Night .....	A10
A10. InSb -1 Standard Deviation Reflectance Scenario, Day vs Night .....	A11
A11. Day -1 Standard Deviation Reflectance Scenario, PtSi vs InSb .....	A12
A12. Night -1 Standard Deviation Reflectance Scenario, PtSi vs InSb .....	A13
A13. PtSi +1 Standard Deviation Reflectance Scenario, Day vs Night .....	A14
A14. InSb +1 Standard Deviation Reflectance Scenario, Day vs Night .....	A15
A15. Day +1 Standard Deviation Reflectance Scenario, PtSi vs InSb .....	A16
A16. Night +1 Standard Deviation Reflectance Scenario, PtSi vs InSb .....	A17
A17. PtSi Rural 5 Km Visibility Scenario, Day vs Night .....	A18
A18. InSb Rural 5 Km Visibility Scenario, Day vs Night .....	A19
A19. Day Rural 5 Km Visibility Scenario, PtSi vs InSb .....	A20
A20. Night Rural 5 Km Visibility Scenario, PtSi vs InSb .....	A21
A21. PtSi Urban 5 Km Visibility Scenario, Day vs Night .....	A22

	Page
A22. InSb Urban 5 Km Visibility Scenario, Day vs Night .....	A23
A23. Day Urban 5 Km Visibility Scenario, PtSi vs InSb .....	A24
A24. Night Urban 5 Km Visibility Scenario, PtSi vs InSb .....	A25
A25. PtSi Increased Humidity Scenario, Day vs Night .....	A26
A26. InSb Increased Humidity Scenario, Day vs Night .....	A27
A27. Day Increased Humidity Scenario, PtSi vs InSb .....	A28
A28. Night Increased Humidity Scenario, PtSi vs InSb .....	A29

List of Tables

Table	Page
I. Coatings and Avg Reflectance .....	42
II. Baseline Humidity Profile .....	45
III. Increased Humidity Profile .....	48
III. PtSi Total Integrated Count Rates .....	67
IV. InSb Total Integrated Count Rates .....	68

Abstract

Platinum Silicide and Indium Antimonide are compared as detector materials in a space based remote sensor using the 3 to 5 micrometer wavelength band. The comparison is based on a scaled count rate involving the material's quantum efficiency, a target's reflected solar and thermal emittances, the atmospheric transmission, and the wavelength. The comparison is made using a baseline scenario and seven sensitivity analysis scenarios. The baseline scenario uses a target at 298°K and a vertical line-of-sight from the target to the remote sensor in space. The atmospheric transmission is calculated using the 1962 U. S. Standard atmospheric model resident in LOWTRAN 6, with a 23 kilometer rural visibility and no cloud cover. A sensitivity analysis was performed by varying the target temperature, target reflectance, and finally the atmospheric properties.

## I. Introduction

For the past several years, Air Force Systems Command has expressed an interest in the use of the three to five micrometer ( $\mu\text{m}$ ), or Medium Wave Infrared (MWIR), wavelength band for remote sensing. This interest has been spurred by the recent advances in producing two dimensional arrays of detector cells. Multiband remote sensing techniques currently operate in the visible and near infrared utilizing ground target signatures dominated by reflected light. Multiband remote sensing techniques have been investigated in the thermal infrared. Weather satellites currently use a multiband scheme using one visible band and one thermal infrared band (8 - 12  $\mu\text{m}$ ). However, detectors operating in the 3 - 5  $\mu\text{m}$  band sense both reflected and thermal radiation from a ground target.

Much has been written on using the 3 - 5  $\mu\text{m}$  band for obtaining thermal images of objects within several hundred meters of the sensor. There is also a large amount of data available on the different types of detectors that can be used in an MWIR remote sensor. But there is nothing in the open literature which evaluates the performance of a space based sensor operating in this spectral region; which is the objective of this research.

A background on remote sensing, reviewing some of the pertinent information identified above, is presented in Chapter II. Included here is a definition of remote

sensing, followed by a discussion of the infrared spectrum, including the two classes of radiation making up the spectrum. Next is a look at the atmospheric windows and how these windows are created. Some typical source emissions are covered next, including several examples in two of the atmospheric windows. Finally the detectors are discussed, emphasizing several detector materials that are currently in use or in research for use in the MWIR band and two types of detectors.

Chapter III explains the methodology used to evaluate the performance of platinum silicide and indium antimonide in a space based remote sensor. The evaluation is based on integrating an equation to calculate the count rate, or number of electrons being produced by the sensor in a set amount of time. This equation considers a target's spectral emissions, atmospheric transmission, sensor optics, and detector material responsivity. To keep the calculations generic and unclassified, all factors concerning the sensor's optics are neglected, thereby creating a scaled count rate, focusing on the target and atmospheric properties. The initial method for evaluating the integral involved writing Fortran code. However, upon further review, it was determined a spreadsheet program was sufficient to accomplish the calculations. Borland's QUATTRO was eventually selected for use due to availability and the author's past experience with the program.

Following the development of the integral to be evaluated in QUATTRO, each of the terms required for the equation is discussed. Finally, the chapter closes with a description of the eight scenarios used to evaluate the two materials.

Chapter IV analyzes the results obtained from the eight scenarios. Each scenario is discussed individually with the main emphasis being on the comparison of platinum silicide and indium antimonide.

The thesis closes with the conclusions reached after analyzing the results and identifies some recommendations for further research in Chapter V.

## II. Background

### Remote Sensing

What is remote sensing? In the broadest sense, remote sensing is collecting and interpreting information about an object/target without being in contact with the object (22:1). Under this definition, remote sensing is hardly a new process, it has been ongoing since there has been animal life on earth. Animals, humans included, have been using remote sensing, i.e., their sight, hearing, etc., since the beginning of time. For this research however, remote sensing will be restricted to the methods employing electromagnetic energy as the means of detecting and measuring target characteristics. With this restriction, some of the most common examples of remote sensing are cameras using visible light, radars using radio waves, and infrared (IR) detectors sensing temperature differences. It is the latter of these which is the particular emphasis in this research.

One of the possible applications for a remote sensor detecting temperature differences is a space based remote sensor. This sensor would be a spacecraft in orbit around the earth acquiring images of the earth itself. These images would then be used to support many missions, three

of the most important of which are earth resources, weather forecasting, reconnaissance and surveillance, and early warning. Earth resources involves the sensing of the earth's natural resources and can be applied to many areas. One such area is the farming industry, where the remote sensor can be used to help determine the health of crops. Reconnaissance and surveillance is used mainly by the military to watch the actions of a potential adversary. In the same token, early warning is used to detect the launch of missiles to provide enough time for the civilian and military leaders of the target country to respond appropriately. All these applications can use sensors detecting differences in target temperatures or reflectivity.

#### Infrared Spectrum

To better define IR remote sensing, IR wavelengths must be delineated. These wavelengths range from 0.75 micrometers ( $\mu\text{m}$ ) to 1,000  $\mu\text{m}$ . Because it encompasses such a wide range of wavelengths, the IR spectrum is usually divided into four bands, the near or short wave IR (SWIR) from 0.75 to 3  $\mu\text{m}$ , the middle or medium wave IR (MWIR) from 3 to 6  $\mu\text{m}$ , the far or long wave IR from 6 to 15  $\mu\text{m}$ , and the extreme IR from 15 to 1000  $\mu\text{m}$ . (For comparison, the visible wavelength band is 0.4 to 0.75  $\mu\text{m}$ ). Common to all

four portions of the IR spectrum, are two classes of target radiation, thermal and gaseous spectra.

Thermal Radiation. Thermal radiation is created by bodies at a certain temperature and a plot of the spectrum emitted is continuous. Ideally, all bodies at the same temperature emit the same spectrum of electromagnetic energy. For this ideal situation to exist, three conditions must be met. First, the body must be in a steady-state condition. Second, the kinetic temperature, the measure of atomic activity, for the body must be well established. Finally, all radiation falling on the object is absorbed. Any body exhibiting these characteristics is called a blackbody (6:6). In reality, there are no blackbodies. However, the radiation from many solid bodies approximate the radiation of a blackbody at the same temperature quite closely.

Scientists and physicists have been able to determine equations for rapidly calculating the wavelength at which the radiation from a solid body is a maximum and the effect of changes in temperature of the body. These equations are derived from the Planck blackbody function,  $B_{\lambda}(\lambda, T)$ , which provides the power per unit area per unit wavelength interval being emitted by a substance at a given

temperature,  $T$ , and at wavelength  $\lambda$ .

$$B_{\lambda}(\lambda, T) = X/Y Z \quad (1)$$

where

$$x = 2\pi h c^2,$$

$$y = \lambda^5,$$

$$z = e^a - 1,$$

$$a = hc/\lambda k T,$$

$$c = 3 \times 10^8 \text{ meters/second,}$$

$$h = 6.63 \times 10^{-34} \text{ joule - seconds,}$$

$$k = 1.38 \times 10^{-23} \text{ joule/Kelvin,}$$

$\lambda$  is wavelength in meters, and

$T$  is temperature in Kelvins (7:1-13).

Several plots of the Planck function appear in Figures 1 through 4. From these plots and Equation 1, two things are apparent. First, as the temperature increases, the total amount of power emitted by the blackbody, integrated across all wavelengths, increases. Second, as the temperature rises, the peak of the curve shifts to the lower wavelengths.

These results are derivable from Equation 1. Wien's displacement law provides the wavelength,  $\lambda_{max}$ , at which the Planck function reaches its maximum value and is given by:

$$T \lambda_{max} = 2897.8 \quad (2)$$

where  $T$  is in Kelvins and  $\lambda_{max}$  in micrometers. The Stefan-Boltzmann law provides the total area under the curve in

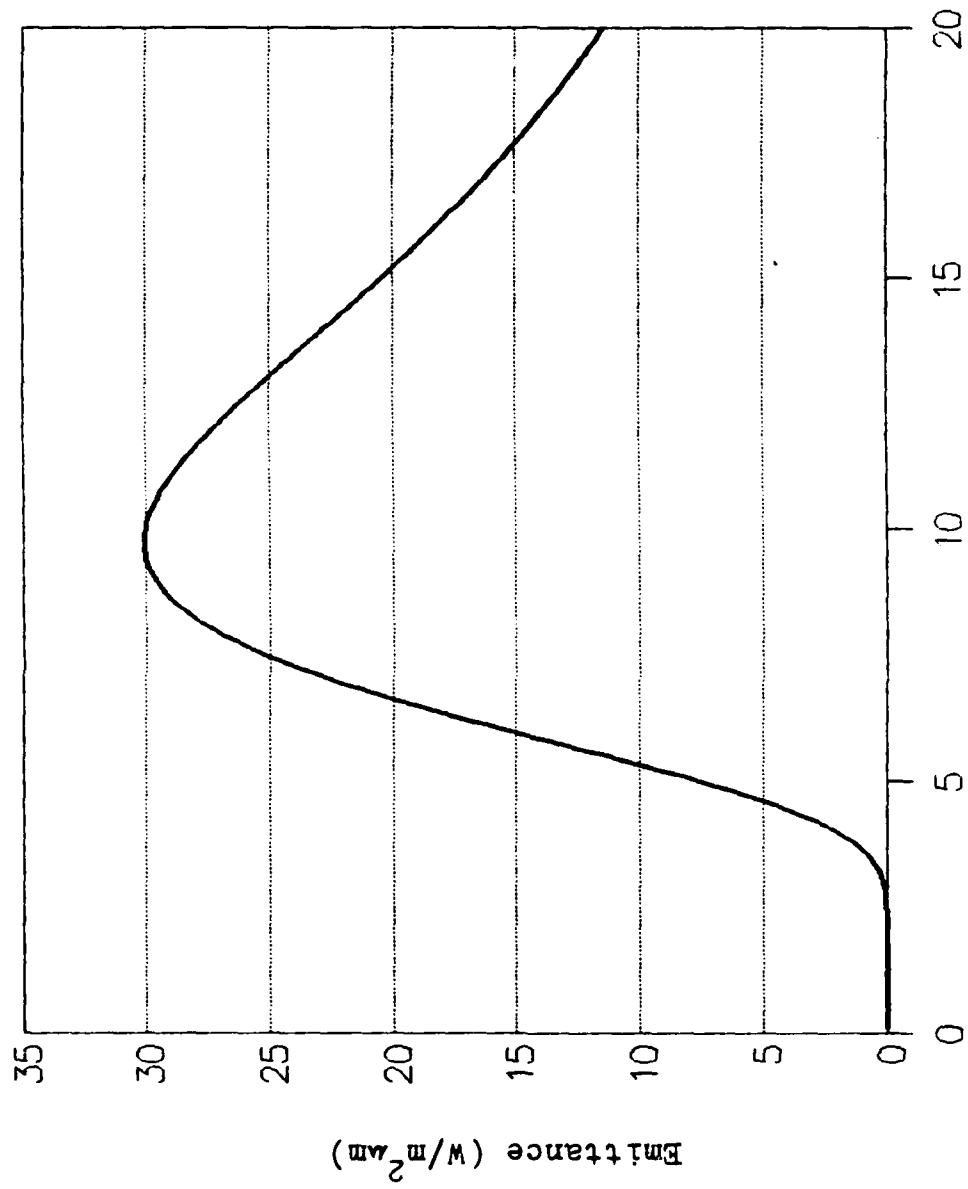


Figure 1. Blackbody Radiation For  $T = 298\text{K}$

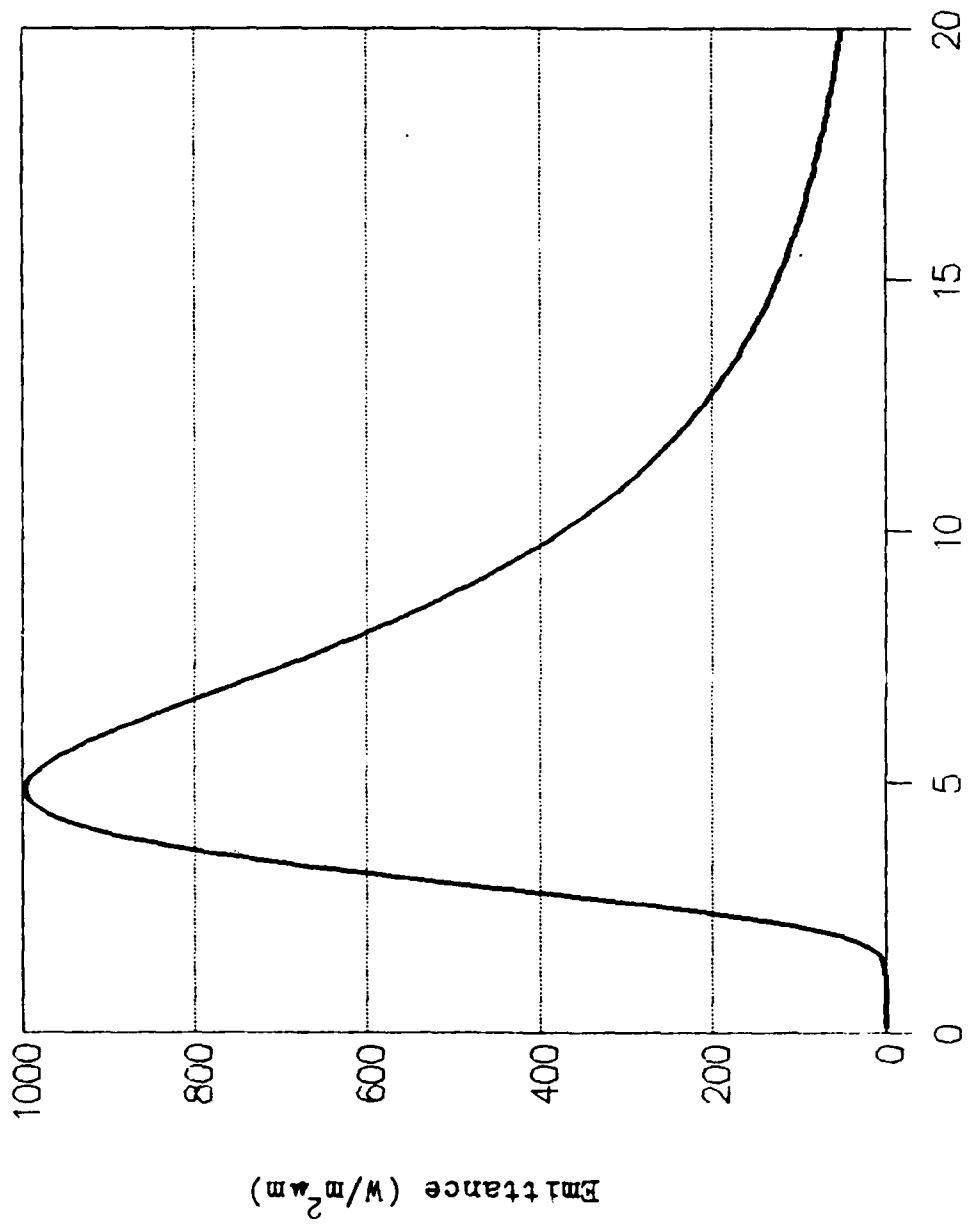


Figure 2. Blackbody Radiation For  $T = 600\text{K}$

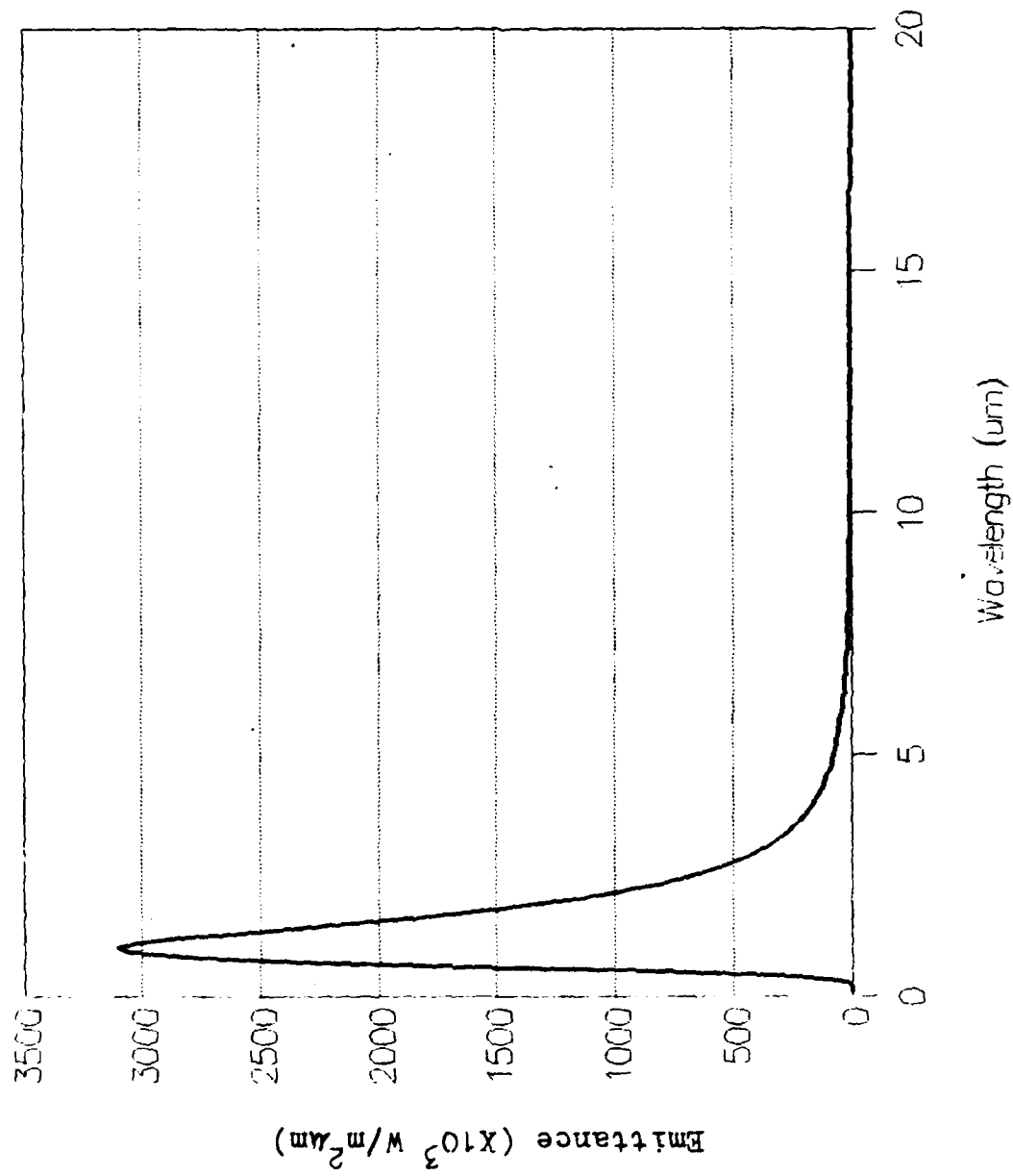


Figure 3. Blackbody Radiation For T = 3000K

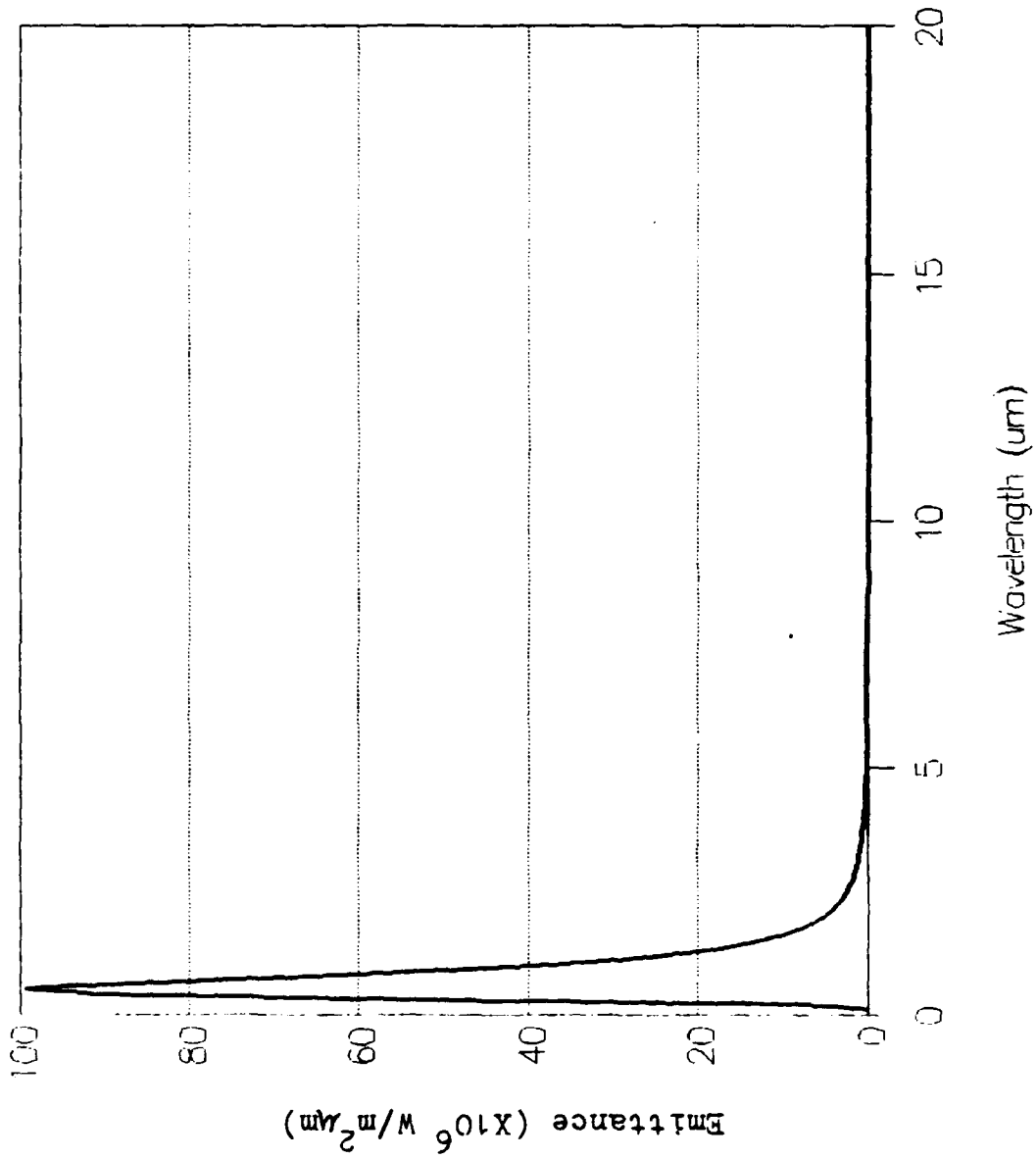


Figure 4. Blackbody Radiation For T = 6000K

any of Figures 1 through 4, and is given by:

$$B = 5.67 \times 10^{-8} T^4 \quad (3)$$

where B is expressed in Watts/meter squared, and T in Kelvins (11:18).

Gaseous Radiation. While thermal radiation is continuous, gaseous may not be. Gases generally emit at particular wavelengths. These emissions are caused by gaseous molecules moving between energy states. Each molecule type, such as water, carbon dioxide, etc., has its own characteristic vibrational and rotational energy levels and therefore can provide an emission spectrum by which to discriminate between molecules (2:297-298).

#### Atmospheric Windows

If an object is emitting either type of radiation identified above and is either on the earth's surface or in the lower regions of the atmosphere, the energy must travel through the earth's atmosphere before it can be detected by a space based sensor. For reasons which will be expounded on later, the earth's atmosphere absorbs much of the IR radiation, however, it also supplies several "windows" through which space based sensors can look. These windows fall neatly into the four bands of the IR spectrum.

The first window coincides with the SWIR band and exists between 0.75 and 2.5 $\mu$ m. A plot of this window is shown in Figure 5. The data was obtained from the LOWTRAN 6 computer code (13:81-100). From the plot, this window can

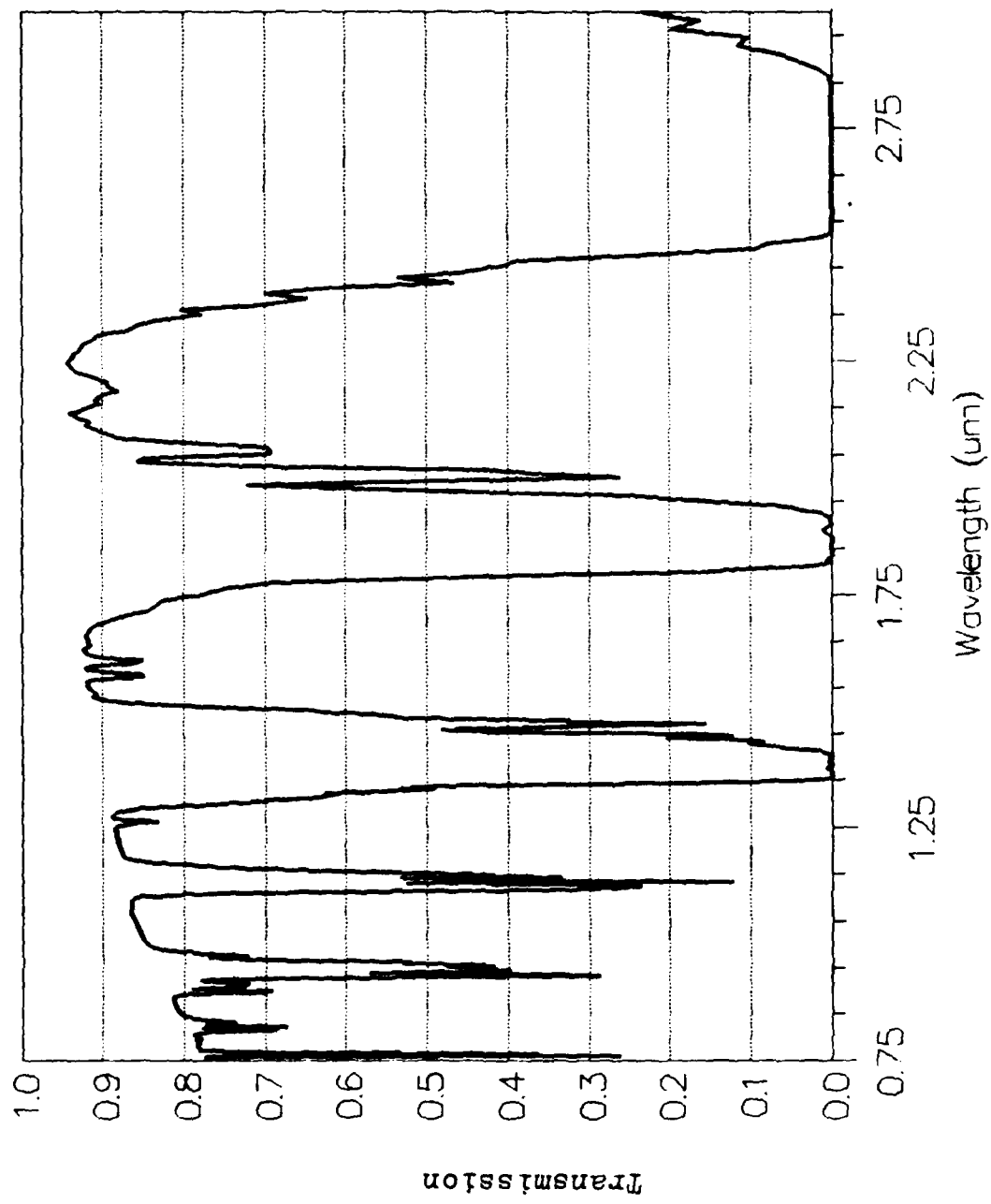


Figure 5. Atmospheric Transmission For SWIR

be subdivided into three parts due to atmospheric absorption characteristics. These sub-bands are 0.75 to 1.3, 1.5 to 1.9, and 2.05 to 2.5  $\mu\text{m}$ . The transmission, or amount of energy transmitted, through the atmosphere for the first sub-band ranges from about 70% to 90% with a few holes with lower transmittance in the middle. In the second sub-band, the transmittance ranges between 85% and 90% at its peak level. The final sub-band has transmittance values from approximately 60% at 2.05  $\mu\text{m}$  to 95% at 2.15 and 2.3  $\mu\text{m}$ . While these sub-bands provide extremely small ranges of wavelengths, they have been used for space based remote sensing.

The second window provided by the atmosphere falls in the MWIR band and is between 3.0 and 5.0  $\mu\text{m}$ . Again LOWTRAN 6 was used to obtain data for this window, and is plotted in Figure 6. As in the first window, this window can also be subdivided; however, there are only 2 sub-bands. The first of the sub-bands lies between 3.4 and 4.2  $\mu\text{m}$  and has an atmospheric transmittance of approximately 90% at 3.5  $\mu\text{m}$ , 60% at 4.15  $\mu\text{m}$  and dropping off quickly to 0% at 4.2  $\mu\text{m}$ . The second sub-band is the 4.5 to 5.0  $\mu\text{m}$  wavelength area. The transmittance of this area reaches a peak of about 68% at about 4.6  $\mu\text{m}$ . While this window is affected more by atmospheric absorption, it is still useful and, as will be shown later, can provide a look at some very interesting targets.

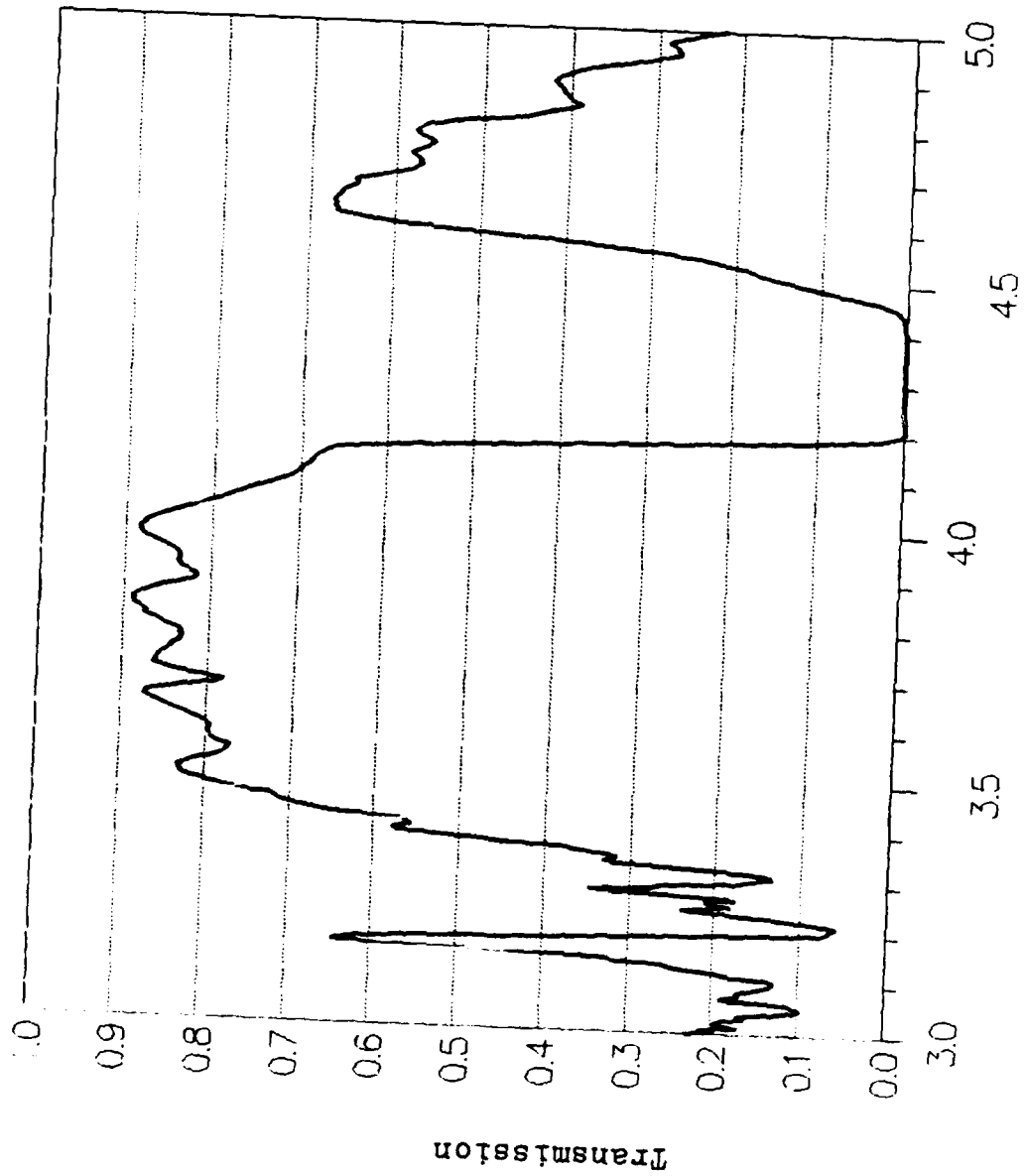


Figure 6. Atmospheric Transmission For MWIR

Falling into the LWIR band is the third window between 8.0 and 14  $\mu\text{m}$ . Like the last window, the LWIR can be subdivided into two sub-bands, and data obtained from LOWTRAN 6 is plotted in Figure 7. The first of these is between 8.0 to 9.5  $\mu\text{m}$ . Here the atmospheric transmittance reaches a peak of approximately 80% at about 8.8 to 9.2  $\mu\text{m}$ . The second sub-band falls between 10.0 and 13.2  $\mu\text{m}$  and has a transmittance above 60% between 10.2 and 12.2  $\mu\text{m}$  and falling off gradually until it reaches about 50% at 13.2  $\mu\text{m}$ . Again, this is a very useful window, not just because of the high atmospheric transmission, but also because of the interesting targets emitting in this spectral region, as will be shown later.

The final window lies in the extreme IR band between 17.0 and 22.0  $\mu\text{m}$ . LOWTRAN 6 data is plotted in Figure 8. This window provides only very limited transmission with a peak just above 10% at about 18  $\mu\text{m}$ . Beyond 18  $\mu\text{m}$ , there is little atmospheric transmission until beyond 1000  $\mu\text{m}$ .

#### Atmospheric Transmission Factors

As was stated before, energy emitted at the surface of the earth or in the lower regions of the atmosphere must travel through the atmosphere to be detected by a space based sensor. The transmission windows identified above are created by a combination of two factors: atmospheric absorption and scattering. The latter can be divided into

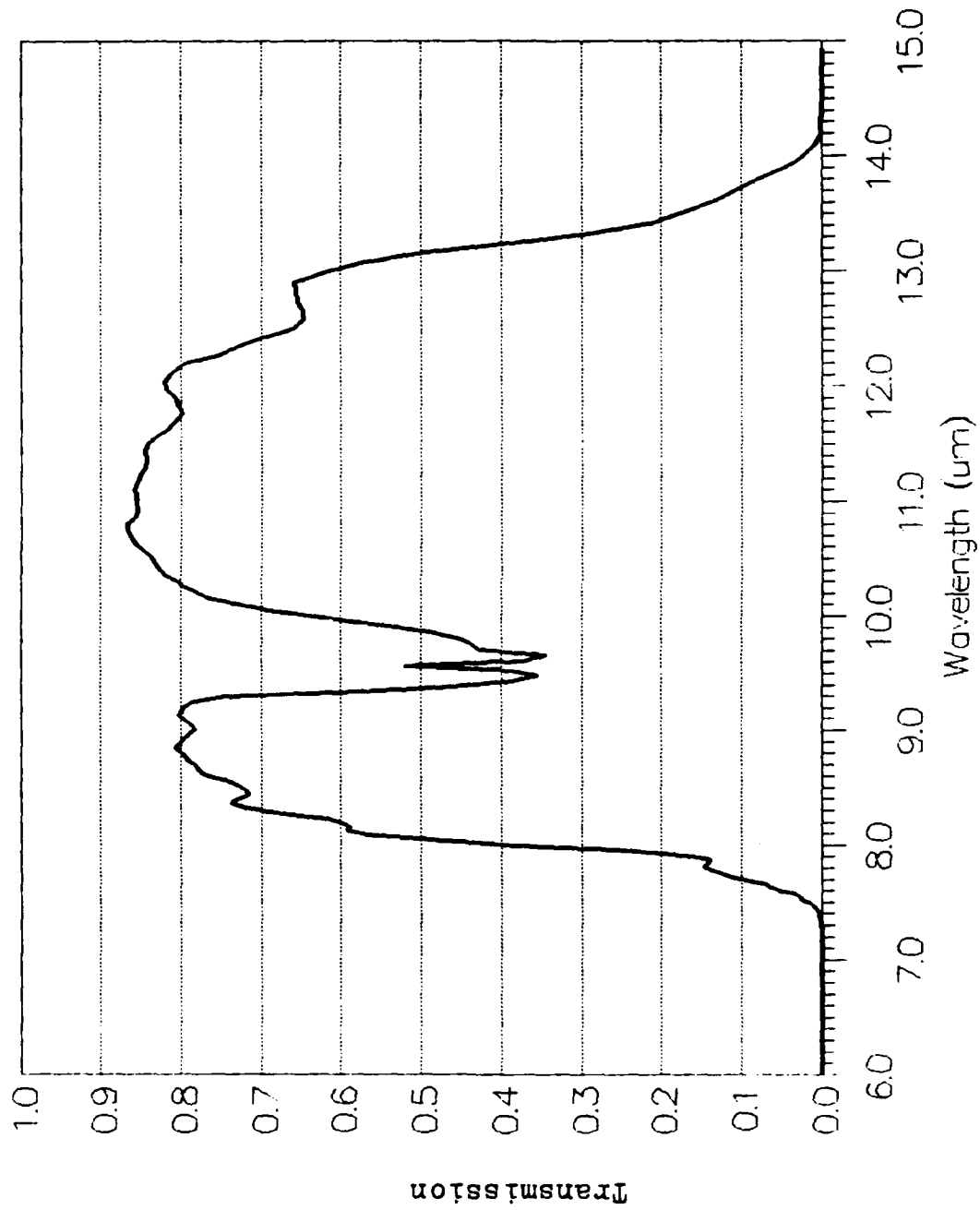


Figure 7. Atmospheric Transmission For LWIR

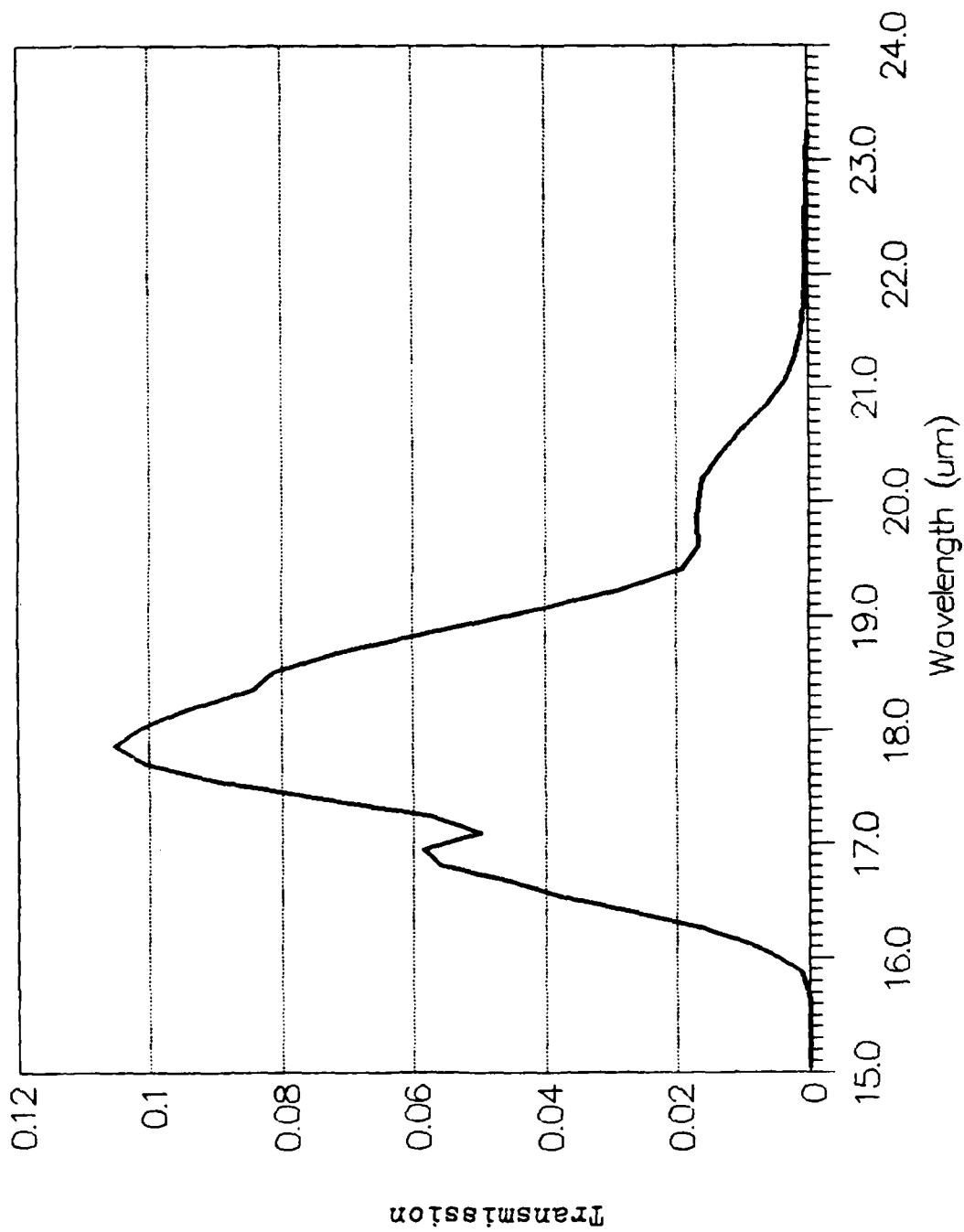


Figure 8. Atmospheric Transmission For Extreme IR

Rayleigh, non-selective, and Mie scattering. Each of the two factors will be discussed in more detail in the following paragraphs.

Atmospheric Absorption. The main factor creating the transmission windows is the absorption characteristics of the atmospheric constituents. The earth's atmosphere is made-up of molecules of numerous gases, primarily nitrogen, oxygen, argon, carbon dioxide, water vapor, and ozone, with numerous trace constituents. For the earth's atmosphere, the major absorbers are molecules of ozone, carbon dioxide, water vapor, and the constituent molecules of "Los Angeles gas" or smog (3:8-1 - 8-12).

The degree to which the target's radiated energy gets absorbed is a function of two things. First, the number of molecular absorbers in the lower energy state. The Boltzmann distribution function provides a good estimate of the number of molecules in the lower energy state. This function states that the number of molecules in the higher energy states decreases exponentially as a function of energy above the ground, or lowest, energy state and the temperature. For atmospheric temperatures, most molecules are in the ground state (10:38). The second function is the number or density of the absorbing molecules between the target and the detector. The density of atmospheric molecules decreases exponentially as the altitude increases (16:39). For most situations, this molecular absorption

has benefited the inhabitants of earth by absorbing much of the sun's harmful radiation. However, this creates problems for remote sensing in that only the windows identified earlier can be used.

Atmospheric Scattering. The second atmospheric transmission factor is scattering of the emitted energy. Whenever radiation encounters particles, it may be absorbed but it is usually redirected. The end result is very much the same as with molecular absorption; energy transmitted from a target toward a sensor is lost in the process. The amount of scattering depends on the number of particles present, the length of the path through the particles, and the size of the particles. The number of particles generally present decreases as altitude increases. The longer the path length to the detector at a fixed altitude, the higher the chances of encountering a particle. These probabilities also increase as the size of the particle increases relative to the wavelength of the radiation. If the wavelength is at least a factor of ten larger than the radius of the particle, the energy will be Rayleigh scattered. Here, some of the energy is essentially absorbed and immediately re-emitted in a different direction. The effect is large only when the number of particles is large. If the radius is at least a factor of ten larger than the wavelength, non-selective scattering occurs. This is similar to hitting a golf ball into a

forest. Between these cases is Mie scattering, where the wavelength and radius are approximately the same.

As previously stated, the atmosphere is made up of many particles, with wide variations in sizes. The number of molecules, with the exception of water vapor and ozone, stays relatively constant from day to day but does vary with altitude. On the other hand, the number of many other particles varies from day to day, and these are the particles causing the main loss of energy in emitted radiation in the atmospheric windows. Representative particles of this type are smoke and haze with sizes ranging from  $10^{-3}$  to  $0.1 \mu\text{m}$ , dust and soot in the 1 to  $100 \mu\text{m}$  size range, and fogs and clouds with particulate sizes of 5 to  $50 \mu\text{m}$  (26:5-22,5-23). Consequently, when these types of particles are abundant, the atmosphere is essentially opaque in the IR; hence, space based remote sensing, using the IR spectrum, can never have a true all-weather capability.

With a knowledge of how the emissions can be generated and how these emissions are affected as they are transmitted through the atmosphere, attention can be given to some typical sources of emissions.

#### Source Emissions

As identified earlier, the following sections will be limited to reviewing properties of the 8 to  $12 \mu\text{m}$  and 3 to  $5 \mu\text{m}$  wavelength bands. Discussion will focus on the

temperature range of blackbody radiation and the energy ranges required for the molecular energy level transitions discussed earlier. Following this will be a discussion of some typical emitters for the appropriate region.

8 to 12  $\mu\text{m}$  Band. The 8 to 12  $\mu\text{m}$  wavelength band is used to detect thermal radiation coming from targets of low to moderate temperatures. Using Wien's displacement law, Equation 2, a target emitting maximum radiation at a wavelength of 8  $\mu\text{m}$ , can be found to be at a temperature of about 362°K. This is equivalent to about 192°F. In a similar fashion, an object emitting its peak radiation at 12  $\mu\text{m}$ , has a temperature of about 241°K or about -25°F. In order to calculate the energy of molecular transitions, the following equation is needed,

$$w = hc/\lambda \quad (4)$$

where:

w is the energy of the transition,

h = 6.63 X 10<sup>-34</sup> joule-seconds,

c = 3 X 10<sup>8</sup> meters/second, and

$\lambda$  is the wavelength in meters (2:298).

Using this equation, radiation with a wavelength of 8  $\mu\text{m}$  would provide 2.49X10<sup>-20</sup> joules, or more appropriately .155 electron volts (eV) for molecular transitions. Likewise, radiation of 12  $\mu\text{m}$  wavelength, provides .104 eV for the

transitions. With these figures, a discussion of emitters is in order. First, a look at the thermal, blackbody radiators.

A major source of blackbody radiation in the 8 to 12  $\mu\text{m}$  wavelength band is the earth itself. The earth receives most of its energy from the sun. The sun, while made of gaseous substances, exhibits a spectrum similar to a blackbody at a temperature of about 5900°K. The Stefan-Boltzmann law, Equation 3, is used to find the total power emitted by the sun is approximately  $6.87 \times 10^7$  Watts/square meter. At the earth's orbit, this power has been reduced to about  $1.48 \times 10^3$  Watts/square meter, since the power received is inversely proportional to the square of the distance from the source. The steady state temperature of the earth based on detailed energy balance calculations is approximately 250°K (8:355). Using Wien's displacement law, Equation 2, the earth then radiates the most power at about 9.66  $\mu\text{m}$ , well inside the 8 to 12  $\mu\text{m}$  band. Therefore, any space based remote sensor looking down at the earth in this band will have a bright background.

Another group of sources derives its blackbody emission characteristics from absorption of solar radiation, vegetation. The leaves of trees are a good example. The major constituents of tree leaves are water and cellulose, because of this, trees absorb most of the radiation falling on them. However, during the day, trees evaporate large

amounts of water through pores in their leaves. At night, these pores close up and the temperature of the leaves closely follows the ambient air temperature. Frequently, the air temperature near the ground is significantly less than it is several meters above the ground (28:3-130). Therefore, the power emitted by a canopy of trees at night is usually greater than the low lying grass surrounding the trees.

Another example of an emitter in this region is the human body. With an internal temperature of 98.6°F, or 310°K, the human body emits its peak radiation at about 9.3  $\mu\text{m}$ . Therefore a remote sensor looking in the 8 to 12  $\mu\text{m}$  band could detect a human. These are just a few of the emitters in this region, there are also many substances that reflect large amounts of energy in this band and also many more emitting here also.

3 to 5  $\mu\text{m}$  Band. In the 3 to 5  $\mu\text{m}$  wavelength band, blackbodies at a temperature of about 580°K (585°F) have maximum radiation at 5  $\mu\text{m}$  and 966°K (1279°F) at 3  $\mu\text{m}$ . Also, using Equation 4 to determine the energy supplied to molecular level transitions, radiation with a wavelength of 3  $\mu\text{m}$  provides .41 eV and radiation at 5  $\mu\text{m}$  provides .25 eV for molecular transitions.

Since these temperatures are so high, the earth's radiation is considerably lower in the 3 to 5  $\mu\text{m}$  band than it is in the 8 to 12  $\mu\text{m}$  band. One source emitting in this

region is of particular interest to pilots. This source is the engines of their aircraft. One typical example is the Pratt and Whitney JT4A-9 flown on Boeing 707s. At most of the stages within the engine, the temperature is within the range detectable by a sensor using the 3-5  $\mu\text{m}$  region (28:2-81). While the nacelle around the engine usually provides enough insulation to keep the hot temperatures inside, the tailpipe and exhaust nozzle are clearly visible and emitting in this band.

Another typical source in this region is fire. A common material involved in many fires is wood or it's products. The minimum temperature to which wood must be heated to initiate a self-contained combustion independent of the heating source is between 380°F and 500°F. Once ignited, wood may burn at over 930°F (17:3-4 - 3-5). Forest rangers would gain a great amount of time and save vast amounts of trees if they had a remote sensor looking for fires in the backwoods where they could neither go nor see.

Finally, a source of radiation in this region that is critical to the security of this nation to be able to detect, missile exhaust. While the propellants of missiles usually burn between 2400°K and 4400°K, the exhaust gases are highly excited and emit vast amounts of line emissions in this region (25:140). For example, the space shuttle main engines burn liquid oxygen and liquid hydrogen. The by-products produced are water vapor, hydrogen molecules,

hydrogen atoms, and hydroxyls. Of these, only the water vapor and hydroxyl molecules (OH) have emission bands in this region (27:67). The water vapor band emission is at 4.3  $\mu\text{m}$  where the atmospheric transmission is reduced to 0. However, the intense heat of the exhaust causes this line to spread out and spill into the region (20:107-108). The hydroxyls have three emission bands within this region. So, a space based remote sensor would be able to detect missiles in the 3 to 5  $\mu\text{m}$  band by looking for the line emissions of the gaseous exhaust.

#### Detectors

The most common detectors found today are semiconductor devices (6:23). The name "semiconductor" comes from the use of semi-metal elements such as silicon, germanium, and antimony in the detectors. These elements are generally considered good insulators, yet they have been found to serve as light-sensitive components of electronic circuits. Common to all semiconductor detectors are the concepts of the valence and conduction bands of the semiconductor material. The electrons in the semiconductor crystals are allowed to populate only discrete energy levels that are determined by quantum physics. The highest energy levels in which electrons are still tightly bound to the atom are called the valence band. The next highest energy levels, in which the electrons are freed from the atoms and allowed to move about the semiconductor crystal are called the

conduction band. The energy difference between these two levels is called the band gap of the semiconductor (6:24). Of the many semiconductor materials available for use in detectors only a few will be discussed.

### Detector Materials

There are two detector materials currently seeing extensive use in infrared MWIR remote sensors, with heavy research being conducted on two other materials. A discussion of these four materials will follow, but first, a definition is required to evaluate each of the materials on an equal basis. The quantum efficiency is "the ratio of the number of countable output events to the number of incident photons" (28:11,16). In other words, the quantum efficiency is a measure of the ability of a detector material to convert incoming infrared radiation into electrons. These electrons are then used by the sensor. The quantum efficiency of a material can take a value from a low of 0 to a high of 1.

As was mentioned earlier, there are two detector materials currently seeing extensive use, with two more receiving heavy research. The two materials currently being used are indium antimonide and mercury cadmium telluride. The materials currently in the research departments are platinum silicide and iridium silicide (4:3-4).

Indium Antimonide. One of the popular materials over the past decade for astronomical MWIR applications has been indium antimonide (12:50). Indium antimonide's popularity is based on several characteristics of the material. First, indium antimonide detectors have a high quantum efficiency of about 0.6 across the MWIR band (4:13,12:51). Also, individual indium antimonide detectors are inexpensive and have a fairly linear response over a wide dynamic range (12:50). Because of these material characteristics, indium antimonide is receiving attention as a detector material for a space based remote sensor.

Mercury Cadmium Telluride. Another popular material is mercury cadmium telluride. As with indium antimonide, mercury cadmium telluride has a high quantum efficiency of about 0.5 across the MWIR spectrum (4:13). While this is good, mercury cadmium telluride detectors do not receive much attention in the MWIR band, because of the properties of the material itself. Mercury cadmium telluride is a semiconductor and is hard to form in a pure state. Therefore, when it is used in a detector array, each individual detector cell has a different response curve. This creates problems when building the large focal plane arrays required for a space based remote sensor by causing significant cell-to-cell nonuniformities. This in turn decreases the sensitivity of the overall sensor (23:42).

Because of this, mercury cadmium telluride is not considered a good material for MWIR detectors for remote sensing.

Platinum Silicide. While indium antimonide and mercury cadmium telluride have been used extensively for remote sensing applications, platinum silicide's popularity has grown recently with the maturation of the Schottky Barrier detector focal plane arrays (19:93). The lack of popularity without the Schottky Barrier technology is due to the low quantum efficiency of the material in the MWIR band. Kosonocky and Elabd state the quantum efficiency for platinum silicide in this band is only several percent (14:167). Cantella's results of the quantum efficiency for a number of materials, including platinum silicide, gives a quantum efficiency for platinum silicide of about 0.05 for 3 micrometer wavelength radiation, decreasing rapidly to about 0.003 for 5 micrometer radiation (4:13). In spite of the poor quantum efficiency, both sources agree that the Schottky Barrier detector focal plane array, with all of its advantages, offsets the low quantum efficiency for platinum silicide (4:12-14,14:167-178). The effect of the Schottky Barrier detector focal plane array offsetting the low quantum efficiency of platinum silicide is further supported by Mooney, et al., and Pellegrini, et al. (18:99-107,19:93-98). Because of the advantages of the Schottky

Barrier detector, platinum silicide will continue to be researched as a material for infrared detectors.

Iridium Silicide. The final detector material, iridium silicide, has been in research since 1982 (19:93). The results of Cantella give a quantum efficiency of about 0.1 for the 3 micrometer radiation, dropping to about 0.04 for the 5 micrometer radiation (4:13). As with platinum silicide, iridium silicide's low quantum efficiency is offset by using Schottky Barrier detector cells in a focal plane array (19:95). Before iridium silicide can be used to a large degree in the focal plane arrays of space based remote sensors, more research is required on the internal workings of iridium silicide and the complex process of forming an iridium silicide layer on a silicon substrate (19:95-96). So, even though iridium silicide has a better quantum efficiency than platinum silicide, it will be some time before iridium silicide begins to replace the platinum silicide. Of the many types of semiconductor detectors available using these materials, the discussion will be limited to two of the most common detectors used in remote sensing, charge coupled devices and Schottky Barrier detectors.

#### Detector Types

Charge Coupled Devices. Charge coupled devices (CCDs) are a very popular type of detector (6:186-188). Sensors using CCDs are made up of varying numbers of individual

cells interconnected into either a one- or two-dimensional focal plane array. In a one-dimensional array, the detectors form a single row or column. In contrast, a two-dimensional array consists of detectors formed into an  $m \times n$  matrix.

All of the CCD cells in a sensor are specially designed semiconductor detectors and work in the following manner. Infrared radiation impinges in a cell, causing electrons to leave the valence band of the semiconductor. The semiconductor is attached to an integration well, a capacitor, which stores the accumulated charge. When the electrons leave the valence band of the semiconductor, they fill the integration well. After a certain amount of time, the integration time, the gate into the well is closed. Essentially the detector is switched off. The well is then electronically scanned by a register which transfers the accumulated charge into the integration well of the next charge coupled device cell. Eventually the charge is transferred out of the array to a signal processor and the process is repeated (9:4).

While CCDs are very popular using silicon for detection, they have several limitations when applied in the MWIR. First, when used in the staring mode for MWIR use, CCDs do not have sufficient storage capacity to accommodate the total possible charge accumulation for the entire integration time (21:135). Also, when compared to the

Schottky Barrier detectors discussed later, CCD focal plane arrays are harder to manufacture, more expensive, and have 100 times more cell to cell photoresponse nonuniformities (23:42). A derivation from, and improvement over, the CCD cell is the Schottky Barrier detector cell.

Schottky Barrier Detectors. Schottky Barrier detectors (SBDs) were developed in the early 1970's; however, due to recent progress, they are now receiving a great deal of attention. The advantages of using an SBD cell over a charge coupled device cell are addressed later, after a discussion of the design and workings of the Schottky Barrier detector.

The principles of Schottky Barrier detection rely on the basic photodiode structure. The diode consists of a metal, usually a very thin silicide film, deposited onto a semiconductor, usually silicon, to provide photoemission. The metal is then connected to a series of charge coupled device cells for readout (4:2). As in CCD arrays, varying numbers of SBD cells are interconnected into one- and two-dimensional focal plane arrays. The current state of the art in SBD focal plane arrays, as illustrated with PtSi as the detector material, is to put a 512 x 512 matrix of SBD cells onto a single chip. One-year-old technology is represented by a 256 x 256 focal plane array, while two-year-old technology is a matrix of 244 x 160 SBD cells (19:93).

Each SBD cell works in the following way. The incident infrared radiation passes through the semiconductor and interacts with the electrons in the metal to raise the electrons' energy above the Fermi level. The Fermi level is the energy level where the probability of an electron occupying either the valence or the conduction band is one half. A portion of the electrons have enough energy to exceed the Schottky barrier, the energy required to transfer a positive charge from the metal to the semiconductor. Thus, a number of positive charges are transferred to the semiconductor, leaving the metal with a net negative charge. This charge is then scanned electronically and read-out through the CCD cells (4:2).

There are a number of reasons why SBD focal plane arrays are being developed for MWIR remote sensing applications. First, Cantella states that Schottky Barrier detectors offer adequate sensitivity in this band (4:11). In addition, Shepherd identifies the following advantages of Schottky Barrier cells over other infrared technologies: 1) elimination of moving electronics; 2) less complex support electronics; 3) lower cost; 4) easier manufacturing; and 5) 100 times better uniformity in cell to cell photoresponse (19:42). The cell to cell uniformity, lower cost, and ease in manufacture are also

mentioned by Kosonocky and Elabd (14:167,185,187). The ease of fabrication and cell to cell uniformity advantages are also mentioned by Aquilera (1:108).

### III. METHODOLOGY

In this chapter, the approach used to evaluate the performance of platinum silicide (PtSi) and indium antimonide (InSb) is explained. The evaluation is based on an equation which calculates the number of electrons created by a sensor, given the target fills the sensor's field of view. This equation is:

$$N = \int_{\lambda_1}^{\lambda_2} \eta(\lambda) G [M_\lambda(\lambda) \Omega_R \tau_{ATM}(\lambda) / \pi h c] A_R (1 - A^2) \tau_{OPT}(\lambda) \lambda d\lambda \quad (5)$$

where

- N is the count rate,
- $\eta(\lambda)$  is the quantum efficiency of the detector material in the spectral bandpass between the limits  $\lambda_1$  and  $\lambda_2$ ,
- G is the gain of the sensor,
- $M_\lambda(\lambda)$  is the spectral emittance of the target, assuming a Lambertian or diffuse emission,
- $\Omega_R$  is the field of view of the sensor,
- $\tau_{ATM}(\lambda)$  is the atmospheric transmission in the spectral bandpass between the limits  $\lambda_1$  and  $\lambda_2$ ,
- h is Planck's constant,
- c is the speed of light,
- $A_R$  is the collecting area of the sensor's front-end optics,

$(1-A^2)$  is the obscuration factor where  $A$  is the ratio of the diameter of a obscuring object in the optics to the diameter of the primary aperture, and  $\tau_{opt}(\lambda)$  is the transmission of all sensor optics in the spectral bandpass (5:222).

In order to keep the calculations generic, i.e., not applied to a single sensor, all factors in Equation 5 relating to the optics are not considered, and  $\tau_{opt}(\lambda)$  is assumed a constant. Hence two useful quantities, the scaled count rate  $SCR$  and the scaled spectral count rate,  $SCR_{\lambda}(\lambda)$ , are defined below using Equation 5.

$$\begin{aligned}
 SCR &\equiv \frac{Nhc\pi}{G\Omega_R A_R (1-A^2)\tau_{opt}(\lambda)} = \int_{\lambda_1}^{\lambda_2} \eta(\lambda) M_{\lambda}(\lambda) \tau_{ATM}(\lambda) \lambda d\lambda \\
 &= \int_{\lambda_1}^{\lambda_2} SCR_{\lambda}(\lambda) d\lambda \quad (6)
 \end{aligned}$$

The integral in Equation 6 can be evaluated using the following:

$$SCR \approx \sum_{i=1}^N \eta(\lambda_i) M_{\lambda}(\lambda_i) \tau_{ATM}(\lambda_i) \lambda_i \Delta\lambda_i \approx \sum_{i=1}^N SCR_{\lambda}(\lambda_i) \Delta\lambda_i \quad (7)$$

When using Equation 7 in Quattro to evaluate the integral, the 3 to 5  $\mu\text{m}$  band was divided into many subbands, each no more than 0.0125  $\mu\text{m}$  wide. Since each of the subbands is small, the average wavelength of each subband is used for the wavelength and to calculate the three terms in Equation 7 that are wavelength dependent.

To compare PtSi and InSb on a wavelength by wavelength basis, using  $SeR_{\lambda}(\lambda)\Delta\lambda$ , the  $\Delta\lambda$  was made extremely small, 0.0005  $\mu\text{m}$ . This provided the count rate for each material basically at individual wavelengths within the 3 to 5  $\mu\text{m}$  band. The total integrated SCR across the entire 3 to 5  $\mu\text{m}$  band used a larger  $\Delta\lambda$  so each subband touched the subbands on either side. The total integrated SCR was then calculated by summing the individual subband SCRs. The rest of this chapter will explain each of the three terms on the right-hand side of Equation 7 followed by the scenarios used to evaluate the detector materials.

#### Quantum Efficiency

The quantum efficiency, as defined in Chapter 2, is a measure of the ability of a detector material to convert incoming radiation into electrons. These electrons are then used by the sensor to obtain an image of the target. The graph of quantum efficiencies presented in Cantella's Space Surveillance technical report, while good for background and rule-of-thumb approaches, is inappropriate for the detailed calculations required here. In a telephone conversation with Cantella, the following equation was cited to calculate the quantum efficiency of a

PtSi Schottky Barrier detector:

$$\eta(\lambda) = \left[ 0.31 \left( 1 - \frac{0.21\lambda}{1.24} \right)^2 \right] \left( \frac{hc}{e\lambda} \right) \quad (8)$$

where

$h$  is Planck's constant,  
 $c$  is the speed of light,  
 $e$  is the charge of an electron in coulombs, and  
 $\lambda$  is the wavelength in  $\mu\text{m}$  (5).

Figure 9 is a plot of the PtSi quantum efficiency calculated from Equation 8. Also, during the same telephone conversation, Mr Cantella verified the quantum efficiency for InSb is constant at 0.65 across the 3 to 5  $\mu\text{m}$  band. He also stated the quantum efficiencies for both materials have been verified with state-of-the-art detectors in the laboratories (5).

#### Target Spectral Emittance

The target spectral emittance is the power exiting a unit surface area of the target. For a target on the earth' surface, the total target emittance can consist of two parts, the emittance due to reflected solar energy from the target and the emittance due to the target's temperature. For this thesis, these are the only sources of energy contributing to the total target emittance.

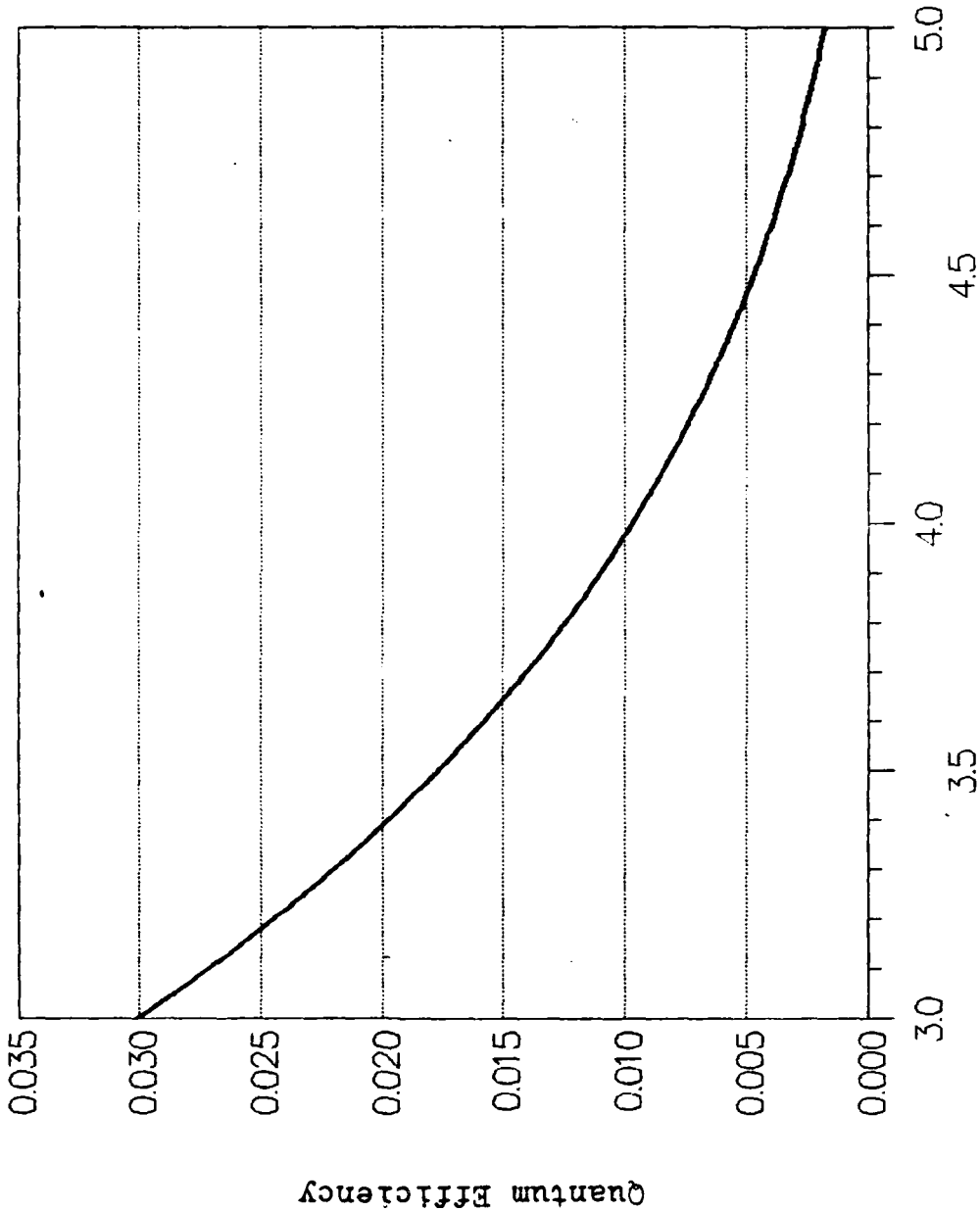


Figure 9. Platinum Silicide Quantum Efficiency

Reflected Solar Energy. The sun is essentially a backbody radiator at a temperature of about 6000°K. Equation 1 was used to calculate the spectral emittance of the sun,  $\beta_{\lambda}(\lambda, T_{sun})$ . However, not all this energy is reflected by the target, some is dissipated by three factors.

The first of the dissipating factors is distance. The sun's energy must travel a distance of about  $R_{1AU} \approx 1.5 \times 10^8$  kilometers to reach the earth's orbit and energy is dissipated during the trip. The amount of energy dissipated is inversely proportional to the square of the distance travelled.

Once the sun's energy reaches the earth, it must pass through the atmosphere to reach the earth's surface. As was stated in Chapter 2, the earth's atmosphere does not allow all the sun's energy through to the surface. The method of calculating the atmospheric transmission  $\tau_{ATM}(\lambda)$  will be addressed in a later section. Now that the sun's energy is at the target, not all the energy is reflected.

To calculate the amount of the sun's energy reflected by the target, the target was assumed to be painted. To keep the calculations generic and unclassified, reflectance data for 20 different coatings were obtained from Touloukian. Table I below lists these coatings as well as an average reflectance for the MWIR band. While there were many data points available, the source did not have a data

point for every coating at every wavelength used in the calculations. To fill the gaps in the data, a straight-line interpolation process was used. Once the appropriate data points were available, an average of the 20 coatings was calculated at each wavelength. Also, the standard deviation for the 20 coatings was calculated at each wavelength and then used to create plus and minus one standard deviation curves. Figure 10 plots the average and standard deviation reflectance,  $R(\lambda)$ , curves for the twenty coatings. The target's reflected emittance  $M_{\lambda R}(\lambda)$  can then be calculated from the following formula:

$$M_{\lambda R}(\lambda) = B_{\lambda}(\lambda, T_{SUN}) \left( \frac{R_{SUN}}{R_{1AU}} \right)^2 R(\lambda) \tau_{ATM}(\lambda) \quad (9)$$

Target Thermal Emittance. As stated in Chapter 2, any object will emit energy characteristic of its temperature. For this research, it is assumed the target is at thermal equilibrium and is emitting as a greybody radiator. A greybody's spectral emittance is calculated by multiplying the blackbody emittance calculated using Equation 1 by the greybody's emissivity,  $\epsilon(\lambda)$ . The emissivity is calculated from the equation  $\epsilon(\lambda) = 1.0 - R(\lambda)$ . The target's thermal spectral emittance is then added to the reflected solar emittance to get the total target emittance. For a space based remote sensor to collect the target's energy, the energy must pass through the earth's atmosphere (See Equation 5).

Table I. Coatings and Avg Reflectance

Coating	Avg Ref
Alkyd Resin	.181
Epoxy Resin	.614
Lacquer Resin	.615
Nylon Resin	.277
Polyurethane Resin	.608
Polyvinyl Chloride Resin	.921
Titanium Dioxide	.108
Lead Molybdenum Tetraoxide	.152
Manganese Oxide	.522
Silicon Nitride	.428
Vanadium Oxide	.254
Zirconium Oxide	.506
Zirconium Silicate	.365
Titanium Dioxide Pigmented	.076
Aluminum Pigmented	.408
Antimony Oxide Pigmented	.055
Carbon Pigmented	.075
Strontium Molybdate Pigmented	.235
Zinc Chromate Pigmented	.147
Zinc Oxide Pigmented	.202

(From 24:14-338, 913-1029, 1111-1151)

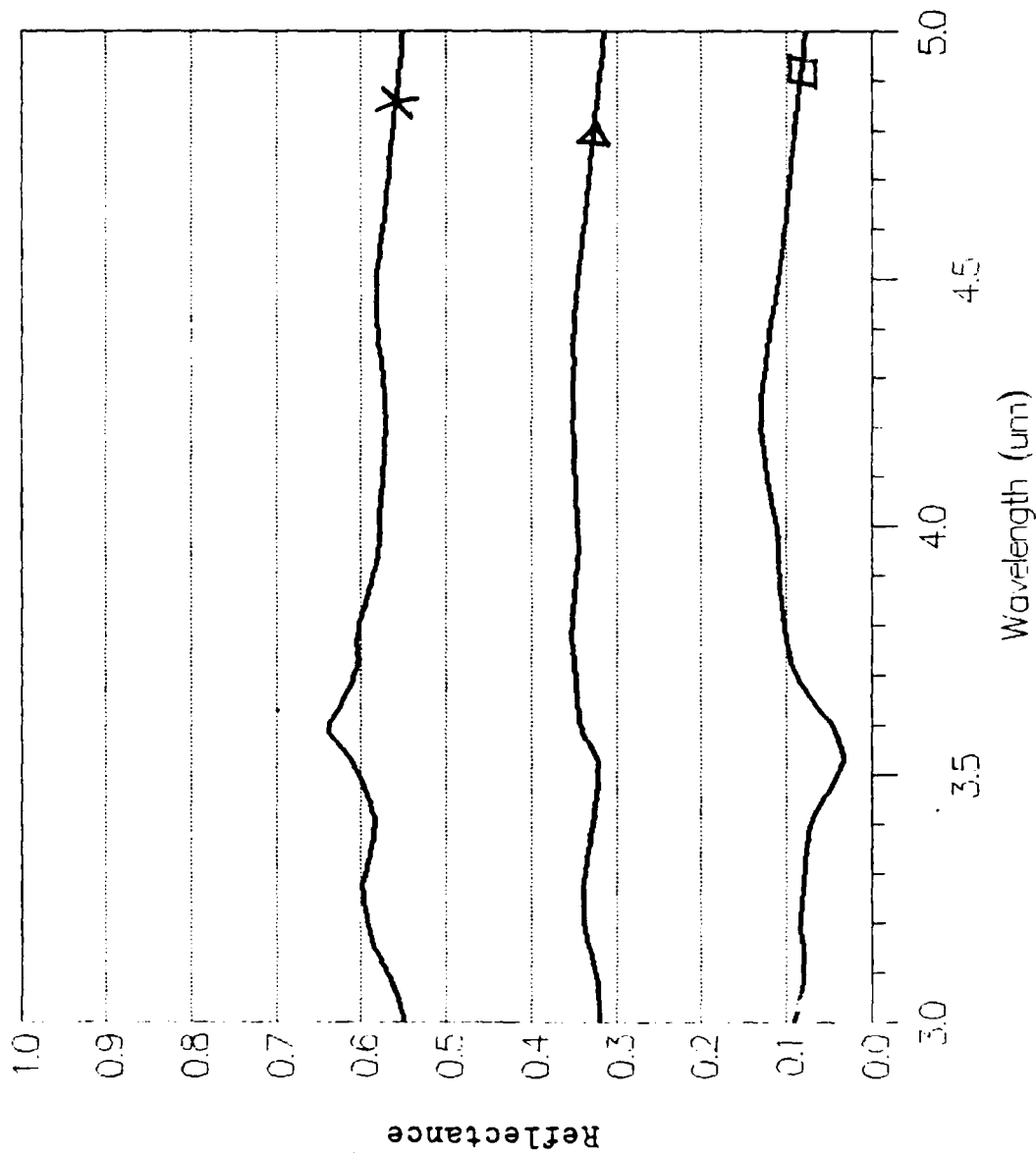


Figure 10. Reflectance Data For 20 Coatings

### Atmospheric Transmission

To calculate the amount of energy reaching a space based remote sensor, an IBM PC version of LOWTRAN 6 was used to calculate the atmospheric transmittance for each wavelength required.

### Scenarios

For all the scenarios identified below, two separate cases were run. The first case involves daylight conditions and incorporates the reflected solar energy. The second case is for night conditions and differs from the first in the lack of the reflected solar energy.

Baseline Scenario. For the baseline scenario, the target's temperature was set at 298°K. The 298°k temperature was selected for three reasons. First, 298°K is about room temperature. Second, this is also the temperature of an average summer day in the U.S. Finally, the majority of data on coatings was obtained with the coating at 298°K.

The atmospheric transmission for these scenarios was calculated for a 1962 U.S. Standard atmospheric model resident in LOWTRAN 6. It also included a directly vertical path from the target to the remote sensor in space. The visibility was set at 23 kilometers in a rural setting with no cloud cover. The humidity profile, as determined in LOWTRAN 6, is listed in Table II below.

Table II. Baseline Humidity Profile

Altitude (Km)	Relative Humidity, %
0.000	46
1.000	49
2.000	52
3.000	51
4.000	50
5.000	48
6.000	49
7.000	48
8.000	51
9.000	37
10.000	29

Target Temperature Scenarios. To evaluate the affect of varying the target's temperature, two more scenarios were used here. In these scenarios, only the temperature changes, all other factors are the same as in the baseline. In the first scenario, the target's temperature is set at 288°K. The second scenario has a target with a temperature of 308°K. Figure 11 plots this target's spectral emittance as well as the 288°K and 298°K emittance curves against the reflected solar component.

Target Reflectance Scenarios. To evaluate the affect of varying the target's reflectance, two scenarios were set

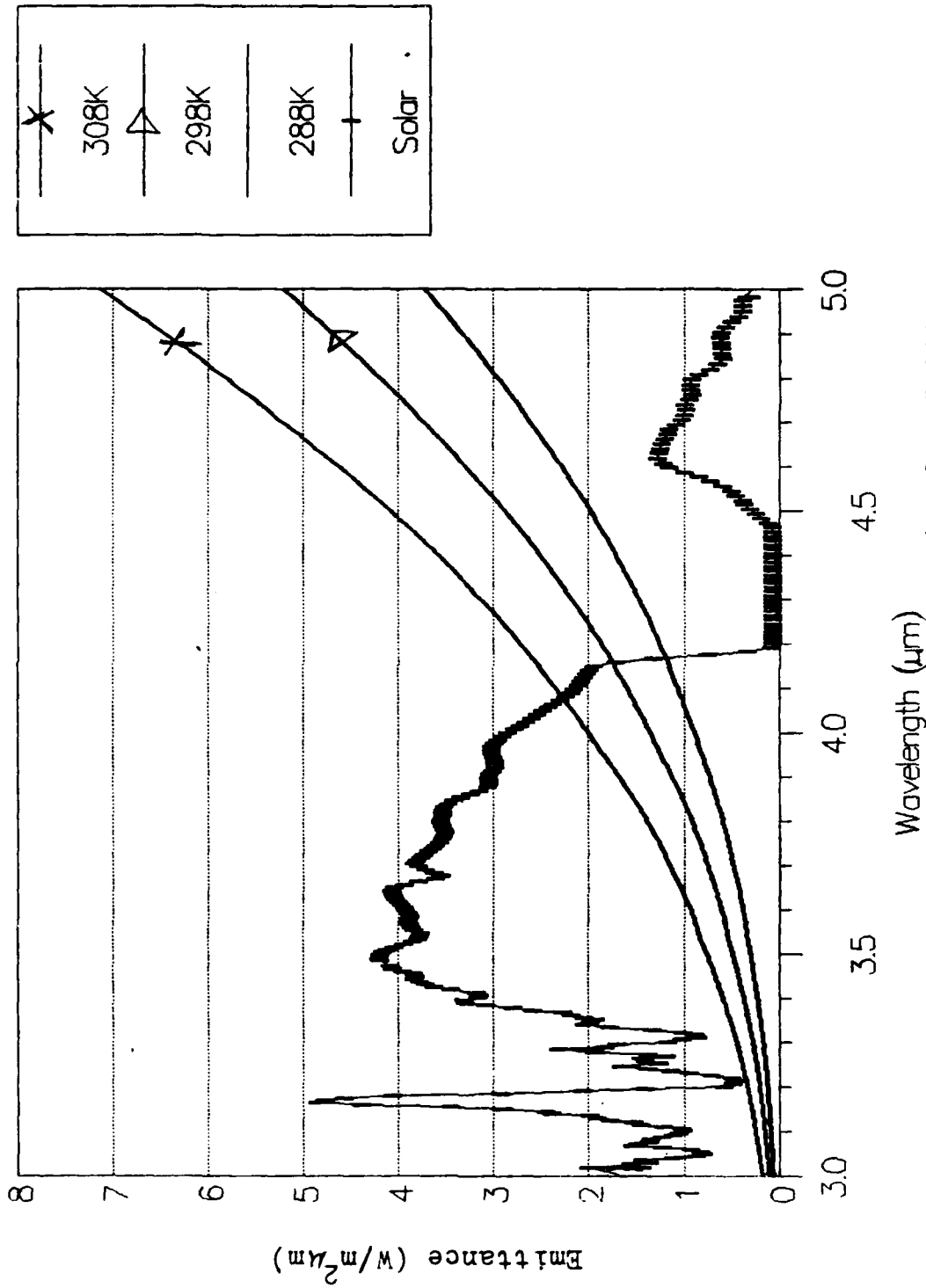


Figure 11. Target Greybody and Reflected Solar Emissance

up where the only change from the baseline is the target reflectance. The first scenario uses the minus one standard deviation curve from Figure 10. The second scenario uses the plus one standard deviation reflectance curve from the same figure.

Atmospheric Scenarios. Three scenarios were developed to look at the influence of the atmosphere on the scaled count rate. The first scenario of this group uses a five kilometer rural visibility. This change only causes more material to be resident in the atmosphere, which causes more absorption and scattering. The atmospheric transmission for this scenario is plotted in Figure 12. The second scenario changes the setting from rural to urban and retains the five kilometer visibility from the previous scenario. This changes the nature of the atmospheric absorbers and scatterers from the natural sources in the rural setting to man-made sources in the urban. Figure 13 is a plot of the transmission for this scenario. The last scenario returns to the baseline and increases the atmospheric humidity from that listed in Table II to the Air Force Geophysics Laboratory tropical humidity profile listed in Table III. The results from the LOWTRAN 6 run for this scenario are plotted in Figure 14.

Table III. Increased Humidity Profile

Altitude (Km)	Increased Water Vapor Density (g/cm <sup>3</sup> )	Baseline Water Vapor Density (g/cm <sup>3</sup> )
0.000	1.94 x 10 <sup>-5</sup>	5.79 x 10 <sup>-6</sup>
1.000	1.18 x 10 <sup>-5</sup>	3.69 x 10 <sup>-6</sup>
2.000	7.54 x 10 <sup>-6</sup>	2.28 x 10 <sup>-6</sup>
3.000	3.40 x 10 <sup>-6</sup>	1.26 x 10 <sup>-6</sup>
4.000	1.41 x 10 <sup>-6</sup>	6.84 x 10 <sup>-7</sup>
5.000	8.45 x 10 <sup>-7</sup>	3.53 x 10 <sup>-7</sup>
6.000	4.20 x 10 <sup>-7</sup>	1.85 x 10 <sup>-7</sup>
7.000	2.03 x 10 <sup>-7</sup>	9.00 x 10 <sup>-8</sup>
8.000	9.40 x 10 <sup>-8</sup>	4.51 x 10 <sup>-8</sup>
9.000	3.92 x 10 <sup>-8</sup>	1.51 x 10 <sup>-8</sup>
10.000	1.41 x 10 <sup>-8</sup>	5.16 x 10 <sup>-9</sup>

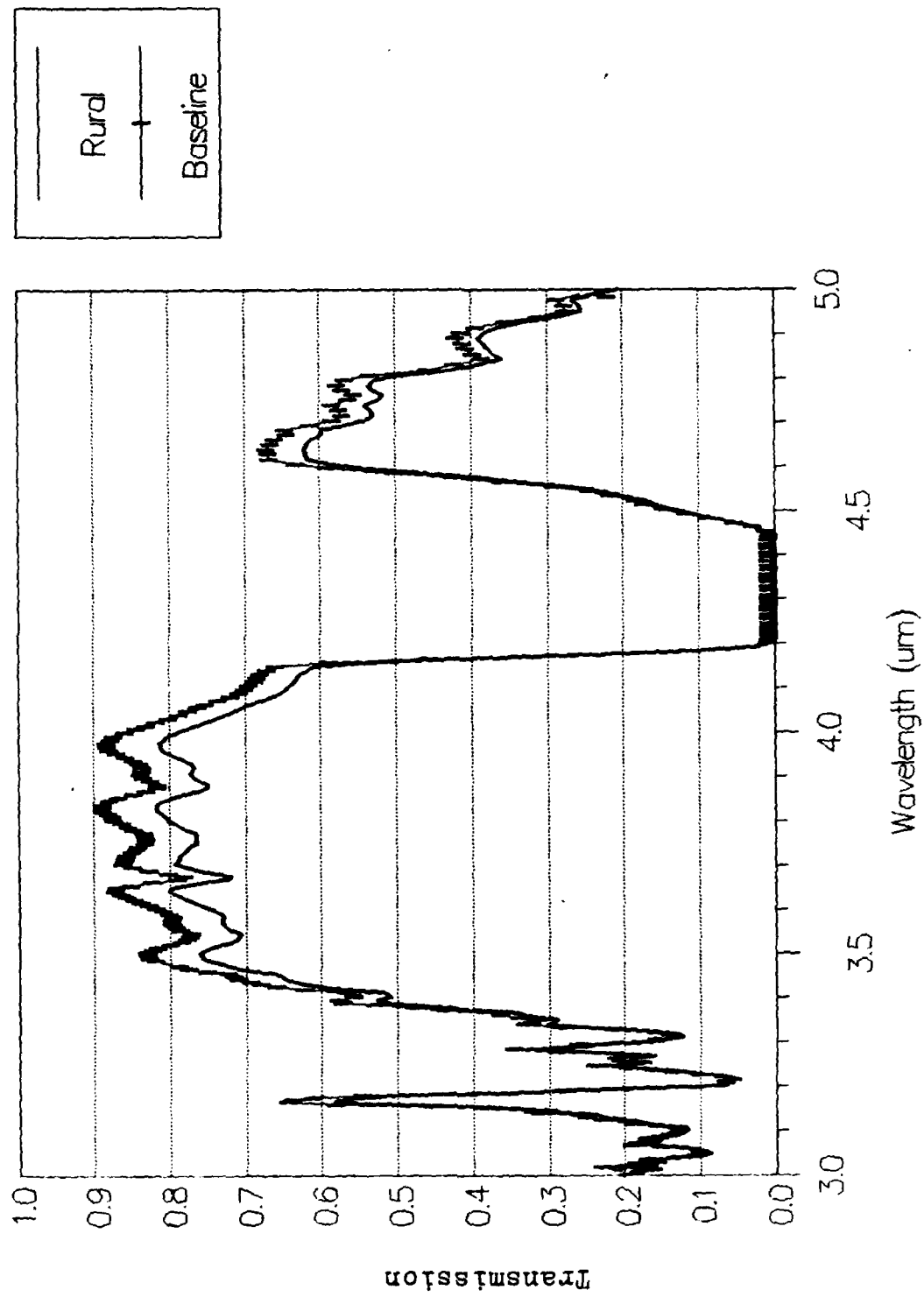


Figure 12. Atmospheric Transmission For Rural 5 Km Visibility vs Baseline

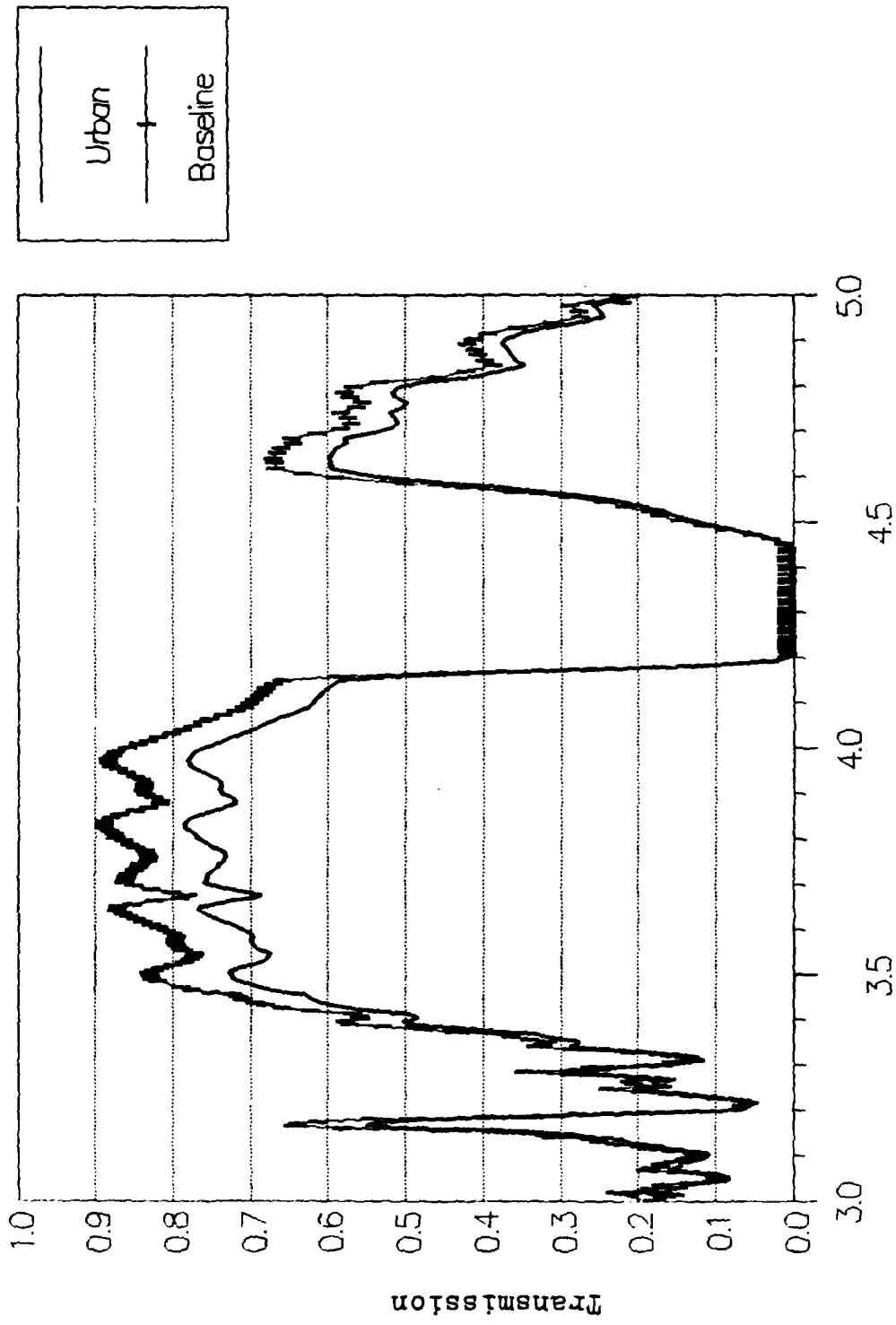


Figure 13. Atmospheric Transmission For Urban 5 km Visibility vs Baseline

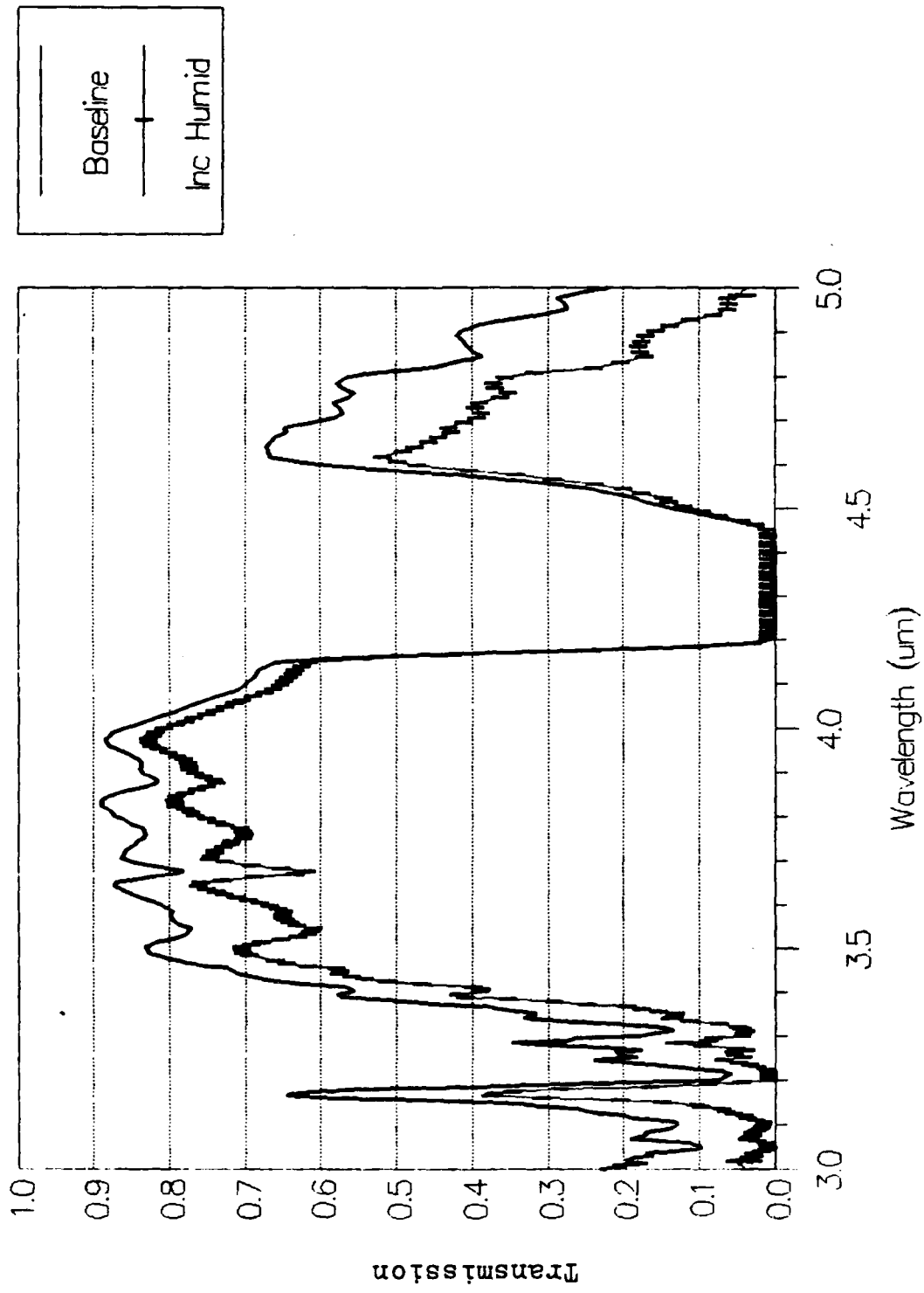


Figure 14. Atmospheric Transmission For Increased Humidity Profile vs Baseline

#### IV. Analysis of Results

The results obtained from Equation 7 for each of the scenarios listed in the previous chapter will be covered in this chapter. First, the baseline scenario will be discussed, followed by the target temperature, target reflectance, and atmospheric scenarios. Each scenario will discuss the day and night responses of each of the two detector materials, PtSi and InSb, as well as compare the two materials against each other. In order to identify gross trends, the two material's normalized count rates are plotted on a wavelength by wavelength basis. These normalized count rates are calculated by dividing the spectral scaled count rate at individual wavelengths by the maximum spectral scaled count rate for that scenario. For instance, in the baseline day scenario using PtSi, the spectral scaled count rate for each wavelength is divided by the maximum value of the spectral scaled count rate. This process yields a normalized count rate between 0.0 and 1.0. This was required because the count rates for InSb turned out to be almost two orders of magnitude greater than those for PtSi.

##### Baseline Scenario

PtSi. Figure 15 shows the day and night normalized count rates for PtSi. The peak of the day curve occurs at about 3.15  $\mu\text{m}$ . Looking at Figure 11, this is also where

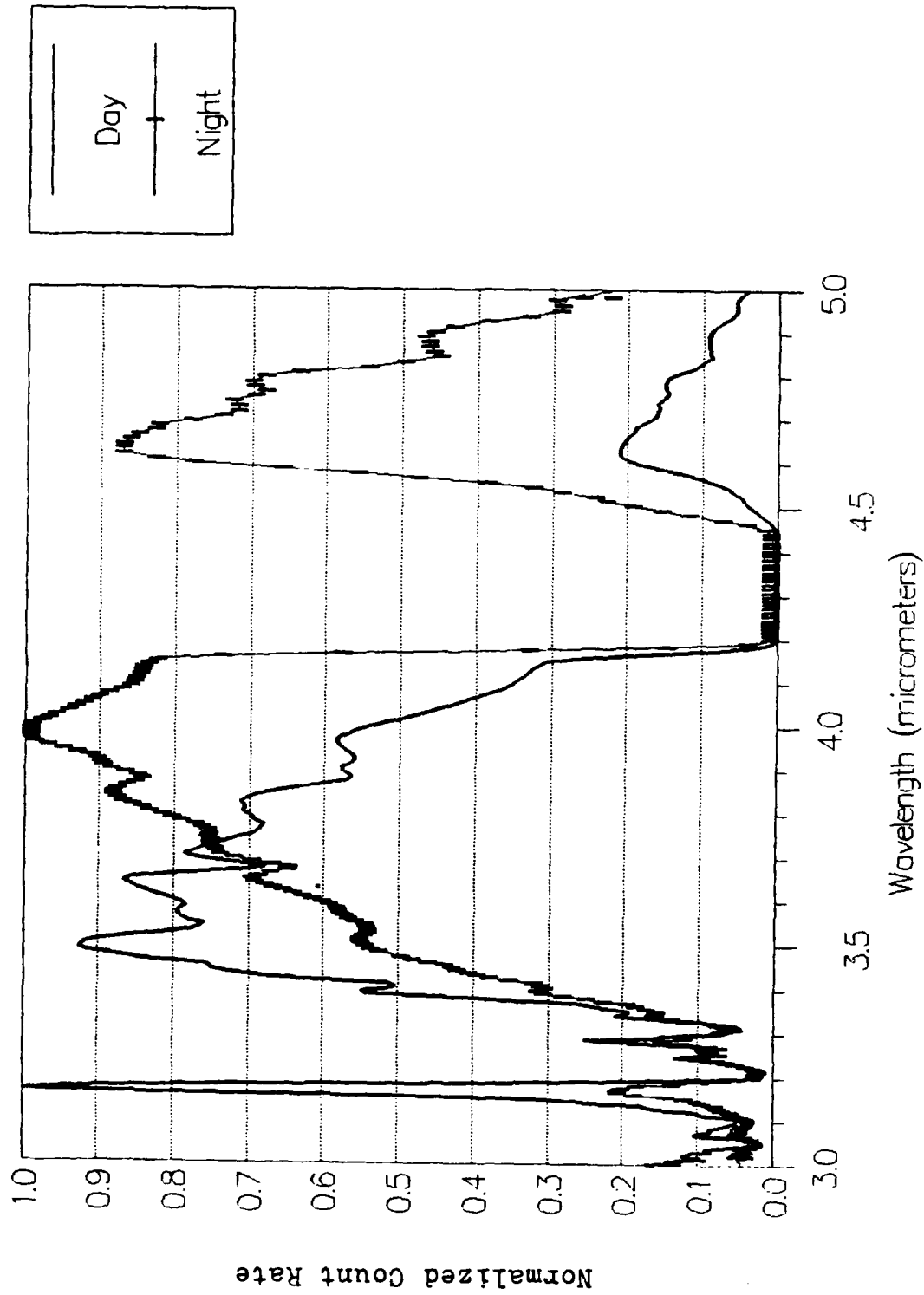


Figure 15. PtSi Baseline Scenario, Day vs Night (Both Curves Normalized To A Maximum of 1.0)

the reflected solar curve peaks. The rest of the day curve drops off because of two reasons. First, and foremost is the quantum efficiency for PtSi drops an order of magnitude between 3.0 and 5.0  $\mu\text{m}$ . Second, from Figure 6, the atmospheric transmission also quickly falls in the 4.5 to 5.0  $\mu\text{m}$  region. The night curve peaks at about 4.0  $\mu\text{m}$  because of the combination of high atmospheric transmission and increasing thermal radiation. Here again the count rate falls off in the 4.5  $\mu\text{m}$  to 5.0  $\mu\text{m}$  region because of the atmosphere and the quantum efficiency of PtSi. The total integrated count rates for PtSi are 0.1654 in daylight and 0.0411 at night. This says that about 75 % of the detector output during the day results from reflected sunlight. This fact, when put with the curves in Figure 15, suggest that PtSi is well suited to picking up reflected solar radiation.

InSb. The normalized count rates for InSb are plotted in Figure 16. The day curve shows a large amount of radiation being detected in the 3.5  $\mu\text{m}$  to 4.0  $\mu\text{m}$  region. This can be attributed to the quantum efficiency for InSb remaining constant at 0.65 across the region as well as the thermal radiation increasing as the reflected solar radiation decreases. The day curve also shows a high count rate in the 4.5  $\mu\text{m}$  to 5.0  $\mu\text{m}$  region for these same reasons. Since the quantum efficiency is constant across the entire region, the night count rate for InSb reflects the changes

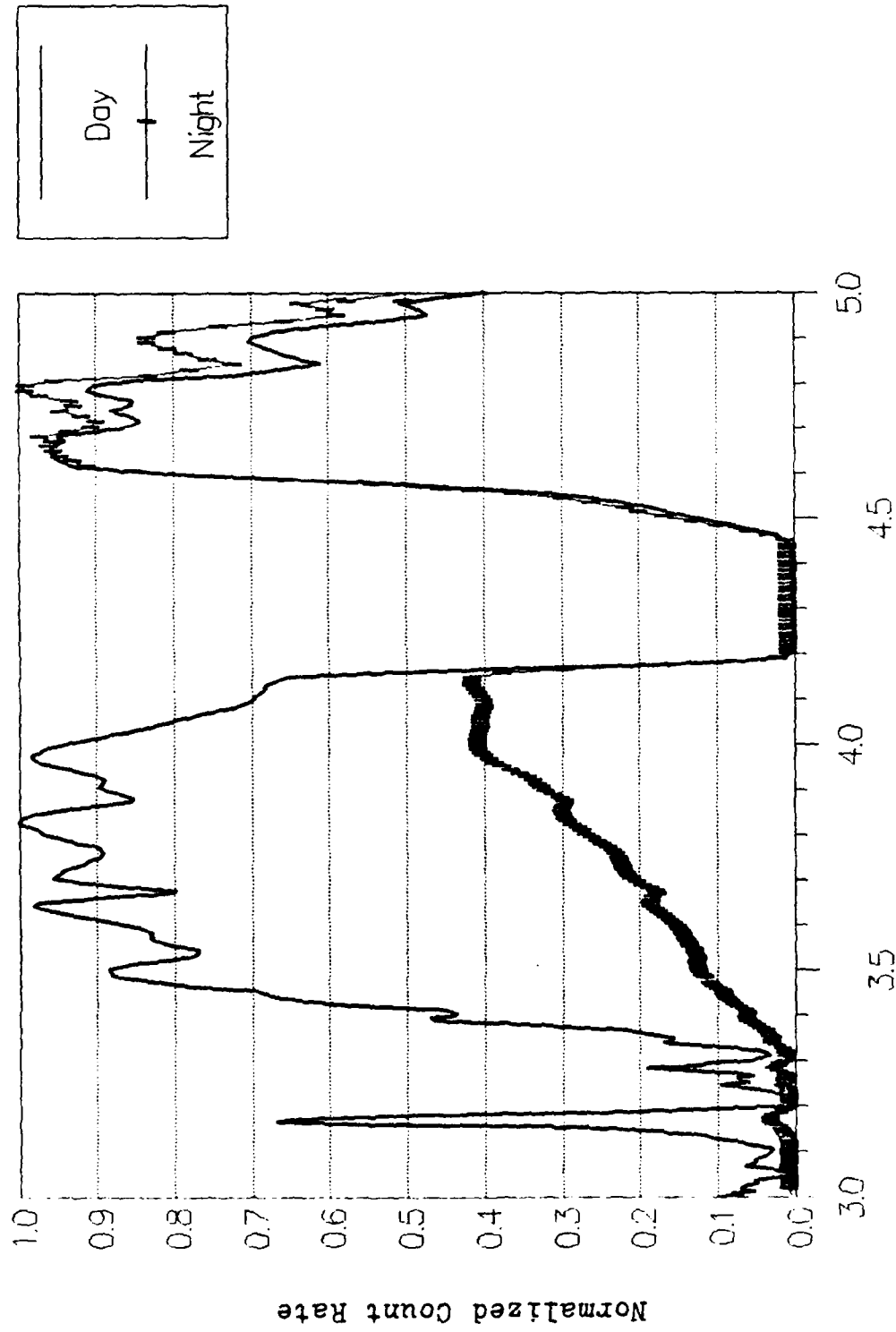


Figure 16. InSb Baseline Scenario, Day vs Night

of the atmospheric transmission and the thermal radiation. In the 3.0 to 4.5  $\mu\text{m}$  region, while the atmospheric transmission is high, the thermal emittance starts low and increases. In the 4.5 to 5.0  $\mu\text{m}$  region, the thermal radiation still increases but the atmospheric transmission reaches a peak at about 4.65  $\mu\text{m}$  and then falls off. The total integrated count rates for InSb are 10.448 in daylight and 4.343 at night. Hence, about 60 % of InSb's response in daylight comes from reflected solar radiation, and 40 % from thermal radiation. This hints that InSb is better able to detect the thermal radiation than PtSi. (Further results and discussion of this point follow.)

PtSi vs. InSb. The day and night cases for PtSi vs InSb are shown in Figures 17 and 18 respectively. Figure 17 shows that during the day, both materials have relatively high count rates between 3.0  $\mu\text{m}$  and 4.0  $\mu\text{m}$ , enabling detection of reflected solar radiation. But it also shows a very high count rate for InSb in the 4.5  $\mu\text{m}$  to 5.0  $\mu\text{m}$  region where PtSi has a low count rate. This again suggests InSb could be better suited to detecting the thermal radiation in this region. Figure 18 shows that for PtSi, there are two regions where the count rate is relatively high, between 3.5  $\mu\text{m}$  and 4.1  $\mu\text{m}$  and between 4.5  $\mu\text{m}$  and 5.0  $\mu\text{m}$ . On the other hand, InSb has a higher count rate in the 4.5  $\mu\text{m}$  to 5.0  $\mu\text{m}$  region than it does between 3.8  $\mu\text{m}$  and 4.1  $\mu\text{m}$ .

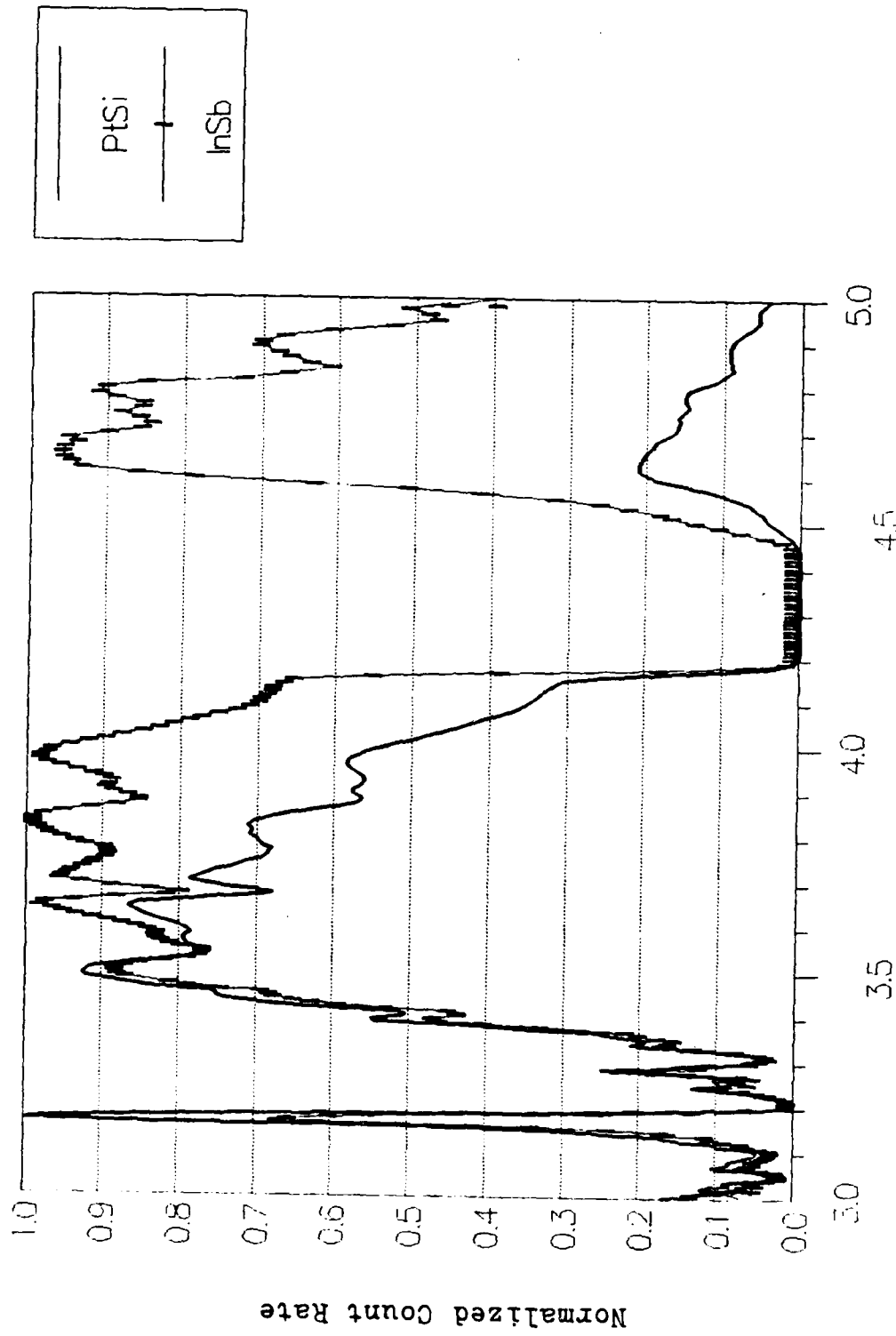


Figure 17. Day Baseline Scenario, PtSi vs InSb

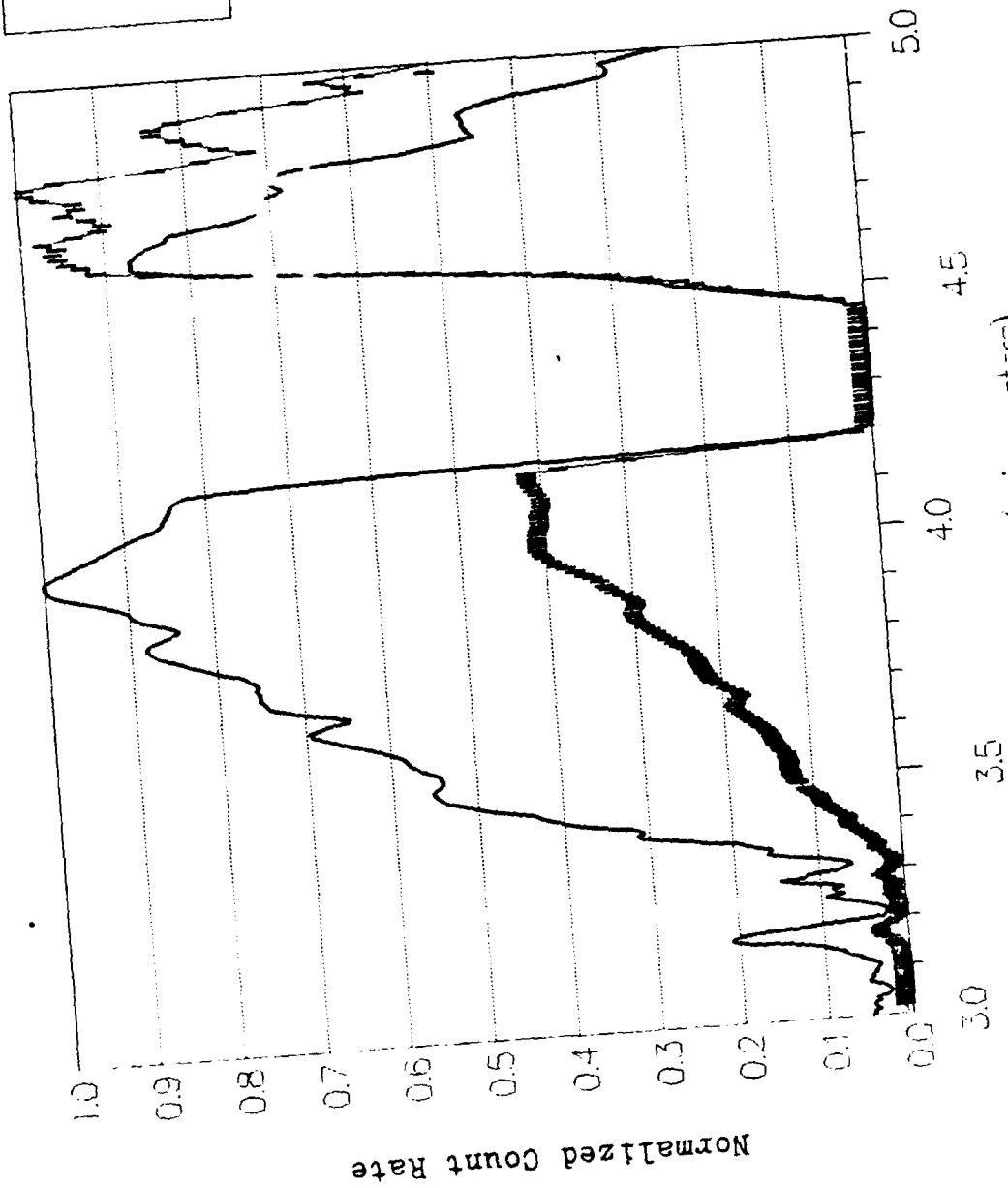
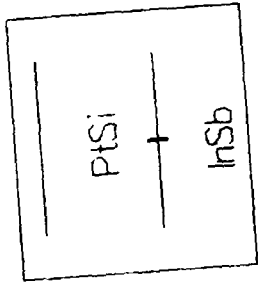


Figure 18. Night Baseline Scenario, PtSi vs InSb

### 288 K Target Temperature Scenario

Figures A1 through A4 in the Appendix plot the normalized count rates for this scenario. Looking at these figures, a change from the baseline is apparent. In the day PtSi case, outside the peak between 3.1  $\mu\text{m}$  and 3.2  $\mu\text{m}$ , the remainder of the curve is lower, reflecting the lower temperature of the target. The total integrated count rate for this case shows only an 8.44 % change from the baseline, down from 0.1654 in the baseline to 0.1515 here. The night spectral curve shows very little difference between the baseline and this case. However, the total integrated count rate for this case is down 33.95 % from the baseline, clearly showing the change in target temperature. Also, the large difference between the percent change for the day and the night cases, shows that PtSi is dominated by the reflected solar radiation in the day.

InSb also shows the same changes as PtSi on the graphs in that the curves are reduced from the baseline except at the maximum values. Again, the amount of change is not realized until looking at the total integrated count rates and the percent change from the baseline. For the day case, the count rate decreased to 9.071 from 10.448, a percent change of 13.18. At night, the rate fell to 2.966 from 4.343, a change of 31.7 %. This shows the reflected solar radiation is again a dominant source during the day.

However, in comparing PtSi and InSb, the percent change for PtSi during the day is lower than InSb. This is caused primarily by the fact that PtSi is somewhat more sensitive to the reflected solar radiation than InSb is. In the night case, the percent change is 31.7 % for InSb and 33.95 % for PtSi.

#### 308 K Target Temperature Scenario

The normalized count rates for this scenario are plotted in Figures A5 through A8 in the Appendix. Comparing these figures to those of the baseline, the same general conclusion is apparent. The curve for PtSi in daylight more closely follows the reflected solar radiation, while the curve for InSb reflects the influence of the thermal radiation more. The total integrated count rates again tend to concur with the conclusion above. For daylight, PtSi increases to 0.185, an increase of 11.85 % over the baseline. The InSb day count rate increases by 17.91 % over the baseline to 12.319. While both are affected by the increased target temperature, PtSi is affected less because of the dominance of the reflected solar radiation.

At night, the PtSi rate is increased 47.7 % from the baseline, while InSb is increased only 43.09 %. Why these changes in night rate are comparable between PtSi and InSb is not immediately obvious. However, in Figure A8, the normalized night count rates for PtSi and InSb, the PtSi

curve peaks at about 4.0  $\mu\text{m}$  and the InSb curve peaks between 4.7  $\mu\text{m}$  and 4.8  $\mu\text{m}$ . Referring back to Figure 6, the atmospheric transmission curve, at 4.0  $\mu\text{m}$ , the atmosphere transmits about 90 % of the radiation incident on it. Between 4.7  $\mu\text{m}$  and 4.8  $\mu\text{m}$ , the atmospheric transmission has fallen to about 0.6. Hence, the total effect is a result of the combination of all these elements - target emittance, atmospheric transmission, and quantum efficiency.

#### -1 Standard Deviation Reflectance Scenario

By decreasing the target reflectance, the amount of solar radiation detected should decrease, and the thermal detection should increase. Figures A9 through A12 plot the results for this scenario. In both day plots, one each for PtSi and InSb, the changes from the baseline are apparent. In both materials, the day plots follow the night plots for the respective material more closely, influenced by the increased thermal radiation. The count rates also show the increased thermal effects. The counts for PtSi show a decrease of 48.53 % for day and an increase of 37.23 % at night. InSb's day count is affected less, with a decrease of only 28.9 % from the baseline. This suggests PtSi is better for detecting the reflected solar radiation than InSb is. The fact that InSb's day count rate is affected less than PtSi's also hints that InSb is influenced more by

the target's thermal radiation. However, InSb's night count rate increases by a similar percentage (36.02 %) to PtSi's night rate.

#### +1 Standard Deviation Reflectance Scenario

In this scenario, just the opposite of the previous scenario happens. With the increased reflectance, the detection of reflected solar radiation should increase. Looking at Figures A13 through A16, this appears to be the case. The day PtSi curve looks very similar to the baseline but from about 3.6  $\mu\text{m}$  through to 5.0  $\mu\text{m}$ , the entire curve is lower by about 0.1 from the baseline. While the PtSi curve's shape remains essentially the same, the InSb day curve is changed dramatically.

In the baseline scenario, the day InSb curve stays above 0.9 between 3.7  $\mu\text{m}$  and 4.0  $\mu\text{m}$ . However, for this scenario, the curve only barely gets above 0.9 at 3.7  $\mu\text{m}$  and 3.85  $\mu\text{m}$  and at 4.0  $\mu\text{m}$  has fallen to 0.8. But the most dramatic change is in the 4.5  $\mu\text{m}$  to 5.0  $\mu\text{m}$  region. Throughout this region, the curve for this scenario is about 55 % that of the baseline. The shape of the day InSb curve now looks very much like the reflected solar emittance curve in Figure 11.

To see the actual effects, the total integrated count rates have to be looked at. The day PtSi count increases 48.5 % over the baseline and the night rate decreases 37.2 %. On the other hand, the day InSb count rate

increases only 28.9 % while the night rate decreases 36.02 %. The difference between the InSb and PtSi day count rates points to PtSi as being more influenced by the reflected solar radiation.

#### Rural 5 Km Visibility Scenario

Referring back to Figure 12, the transmittance curve for this scenario, it is apparent the transmittance is affected more in the 3  $\mu\text{m}$  to 4.2  $\mu\text{m}$  region than it is in the 4.5  $\mu\text{m}$  to 5.0  $\mu\text{m}$  region. This should show up in the count rates as a larger decrease in reflected solar than thermal radiation. The total integrated count rates show this trend. The day PtSi count rate decreases 14.12 % from the baseline while the night rate changes only about 8 %. The InSb day count rate also decreases more than the night rate, a change of 12.41 % for the day vs. 7.61 % for the night rate. The fact that the PtSi day rate decreases more than the InSb day rate again shows PtSi is affected more by the reflected solar radiation. This is also seen in the plots of the normalized count rates for this scenario, which are shown in Figures A17 through A20. In comparing the shapes of these curves against the baseline figures, there is very little difference. Therefore, the discussion of the factors leading to the shape of the baseline scenario also applies to the curves for this scenario and will not be repeated here. Suffice it to say that it appears from the graphs that PtSi is dominated by the

reflected solar radiation during the day, and InSb has a region where the reflected solar radiation is dominant and a region where the thermal radiation is dominant.

#### Urban 5 Km Visibility Scenario

Looking at Figure 13, the atmospheric transmittance for this scenario is affected more in the 3.0  $\mu\text{m}$  to 4.2  $\mu\text{m}$  region than in the 4.5  $\mu\text{m}$  to 5.0  $\mu\text{m}$  region, just as in the last scenario. In this scenario, the total integrated count rates again show a larger decrease in the day count rates than in the night rates. The day rate for PtSi decreases by 20.4 % while the night count rate decreases only 11.61 %. Similarly, the day InSb count rate goes down by 17.87 % compared to 11.04 % for the night count rate. As with all the other scenarios, PtSi is influenced more by the reflected solar radiation and InSb by the thermal radiation.

Figures A21 through A24, the plots of the normalized count rates for this scenario, also show similar results compared to the last scenario. Again PtSi follows the general shape of the reflected solar radiation, while InSb has a region where each of the types of radiation is dominant.

#### Increased Humidity Scenario

Figures A25 through A28 plot the normalized count rates associated with an atmosphere with the increased

humidity profile as shown in Table III and transmittance as plotted in Figure 14. Comparing these figures with the baseline, several changes can be seen. First, in the day PtSi curve for this scenario, the initial spike between 3.1  $\mu\text{m}$  and 3.2  $\mu\text{m}$  has been cut in half. Second, the day InSb curve is drastically reduced in both the 3.5  $\mu\text{m}$  to 4.0  $\mu\text{m}$  and 4.5  $\mu\text{m}$  to 5.0  $\mu\text{m}$  regions. In the first region, the baseline stays above 0.8 for almost the entire band; whereas with the increased humidity, the normalized count rate does not reach 0.8 until 3.5  $\mu\text{m}$  and stays above 0.8 only between 3.8  $\mu\text{m}$  and 4.1  $\mu\text{m}$ . The second region's peak in this scenario has been decreased to about 0.75 from 0.95 in the baseline. Finally, the count rate after this lower peak falls off more quickly for this scenario than it does for the baseline. In spite of these changes, the general shapes still suggest that PtSi is dominated by the reflected solar radiation and InSb is influenced more by the target's thermal radiation.

The total integrated count rates again tend to support this conclusion. The day PtSi count rate is reduced 20.95 % from the baseline compared to 25.04 % for InSb. The night cases also show this difference. The night PtSi count rate is down only 21.55 % while InSb is down 31.02 %. Looking at Figure 14, the difference in the atmospheric transmittance between the baseline and this scenario is

greatest between 4.6  $\mu\text{m}$  and 5.0  $\mu\text{m}$ , right where the target's thermal radiation is increasing rapidly and a significant portion of the InSb count rate is generated.

## V. Conclusions and Recommendations

### Conclusions

The goal of this research was to evaluate PtSi and InSb as detector materials for a space based remote sensor. To this end, the total integrated count rates for both materials were calculated as described in Chapter III. The PtSi total integrated count rates and percent change from the baseline for each of the eight scenarios are presented below in Table IV. Table V lists the InSb total integrated count rates and percent change from the baseline for each of the scenarios.

Table IV. PtSi Scaled Count Rates, SCR

Scenario	Day	% Change From B/L	Night	% Change From B/L
Baseline	.1654	0.0	.0411	0.0
288 K	.1515	- 8.44	.0272	-33.95
308 K	.1850	+11.85	.0607	+47.70
Rural 5 Km	.1421	-14.12	.0378	- 7.96
Urban 5 Km	.1317	-20.40	.0363	-11.61
-1 SD Ref.	.0855	-48.53	.0564	+37.23
+1 SD Ref.	.2457	+48.53	.0258	-37.23
Inc Humidity	.1140	-20.95	.0322	-21.55

Table V. InSb Scaled Count Rates, SCR

Scenario	Day	% Change From B/L	Night	% Change From B/L
Baseline	10.4477	0.0	4.343	0.0
288 K	9.0709	-13.18	2.966	-31.70
308 K	12.3188	+17.91	6.214	+43.09
Rural 5 Km	9.151	-12.41	4.012	- 7.61
Urban 5 Km	8.581	-17.87	3.863	-11.04
-1 SD Ref.	7.429	-28.90	5.907	+36.02
+1 SD Ref.	13.467	+28.90	2.779	-36.02
Inc Humidity	7.159	-25.04	2.982	-31.02

It is interesting to note that in the day count rates for both materials, that those factors affecting the thermal contribution, the target temperature and atmospheric humidity, show a greater influence on the rates of InSb. Conversely, those factors affecting the reflected contribution, atmospheric visibility and target reflectance, show a greater influence on PtSi. The night count rates for the increased humidity scenario also tend to show the InSb relationship above.

In summary, the results obtained from this study point toward PtSi as the better detector material to use to

detect reflected solar radiation and InSb for detecting the target's thermal radiation (except for high humidity conditions).

### Recommendations

This research is not a complete analysis of a space based remote sensor application. As such, there are three areas warranting further research: 1) use of a point source for the target; 2) use of an actual sensor; and 3) considerations of the effects of noise. Each of these areas will be discussed below.

Point Source Target. The first assumption made in the methodology was that the target filled the sensor's field of view. Another option is to have the target not fill the field of view, in which case the target can be modelled as a point source. This change brings in an important factor for a space based remote sensor, the range from the target to the sensor. This is important because the count rate for a point source target is inversely proportional to the square of the range. Another factor created by the use of a point source is the inclusion of background radiation. The target's radiation, thermal and/or reflected solar, must be sufficiently different from the background to have the sensor pick up and detect the target.

Actual Sensor. The methodology used here was to address only the target, atmosphere, and detector material quantum efficiency, not the sensor optical design. This

moved eight sensor design factors to the left-hand side of the scaled count rate equation. These eight factors could have an effect on the performance of the PtSi and InSb detectors evaluated here. To actually see if the two materials are good for a particular sensor combination, the actual sensor optic factors must be considered. While the results from this thesis suggest that both materials can be used in a space based remote sensor, the final analysis comes down to the sensor optics.

Noise. Again, it appears from this research that PtSi and InSb are good for detecting different types of infrared radiation. But before a sensor can detect and classify a target with any degree of confidence, the sensor must be able to identify this radiation over a number of noise sources. If the noise sources are creating a larger signal than the target, the target will go undetected. Therefore, in future research, some noise considerations are appropriate.

Appendix

Sensitivity Analysis Graphs

Figures A1 through A28 plot the normalized count rates for all scenarios other than the baseline.

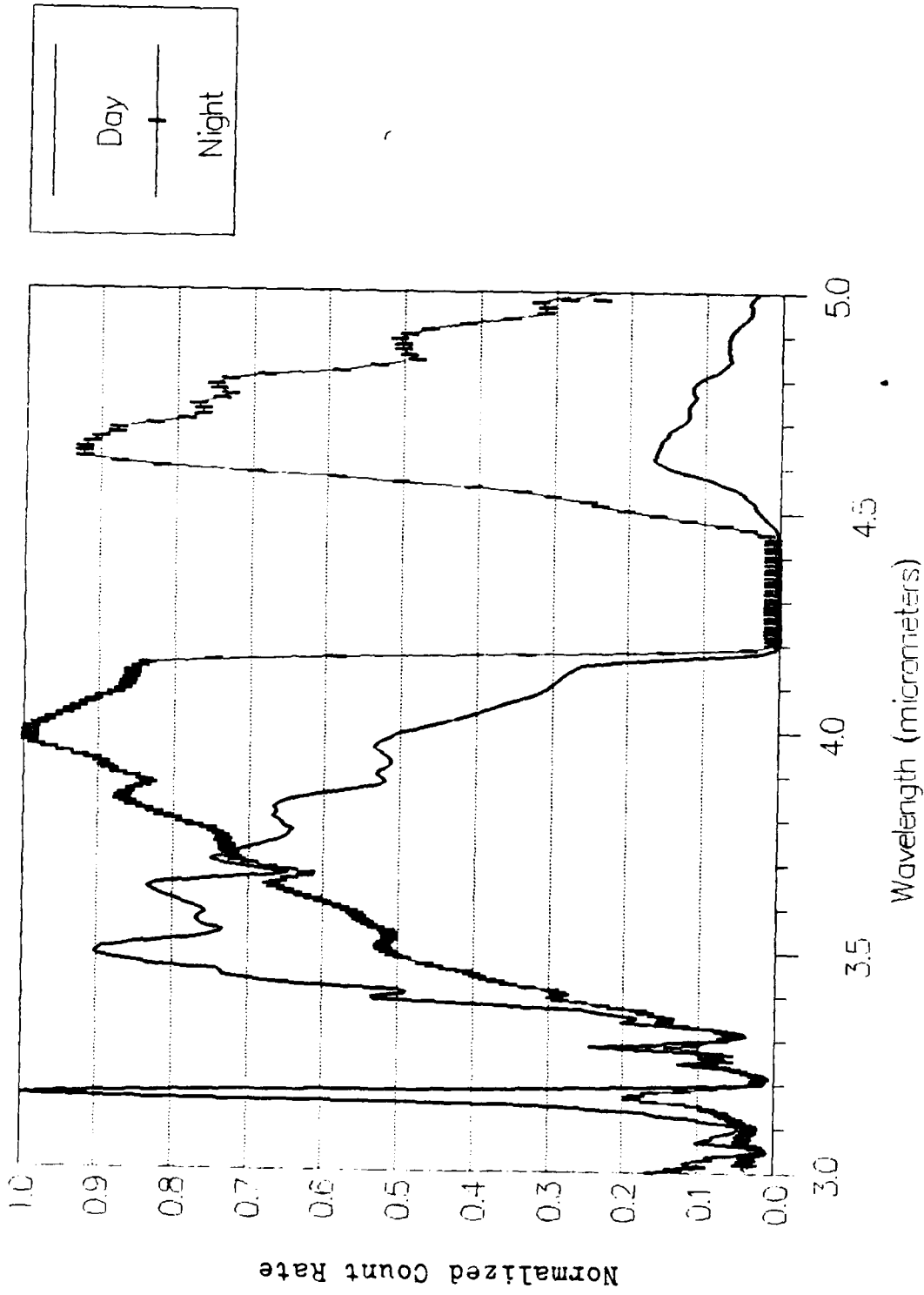


Figure A1. PtSi 288K Scenario, Day vs Night

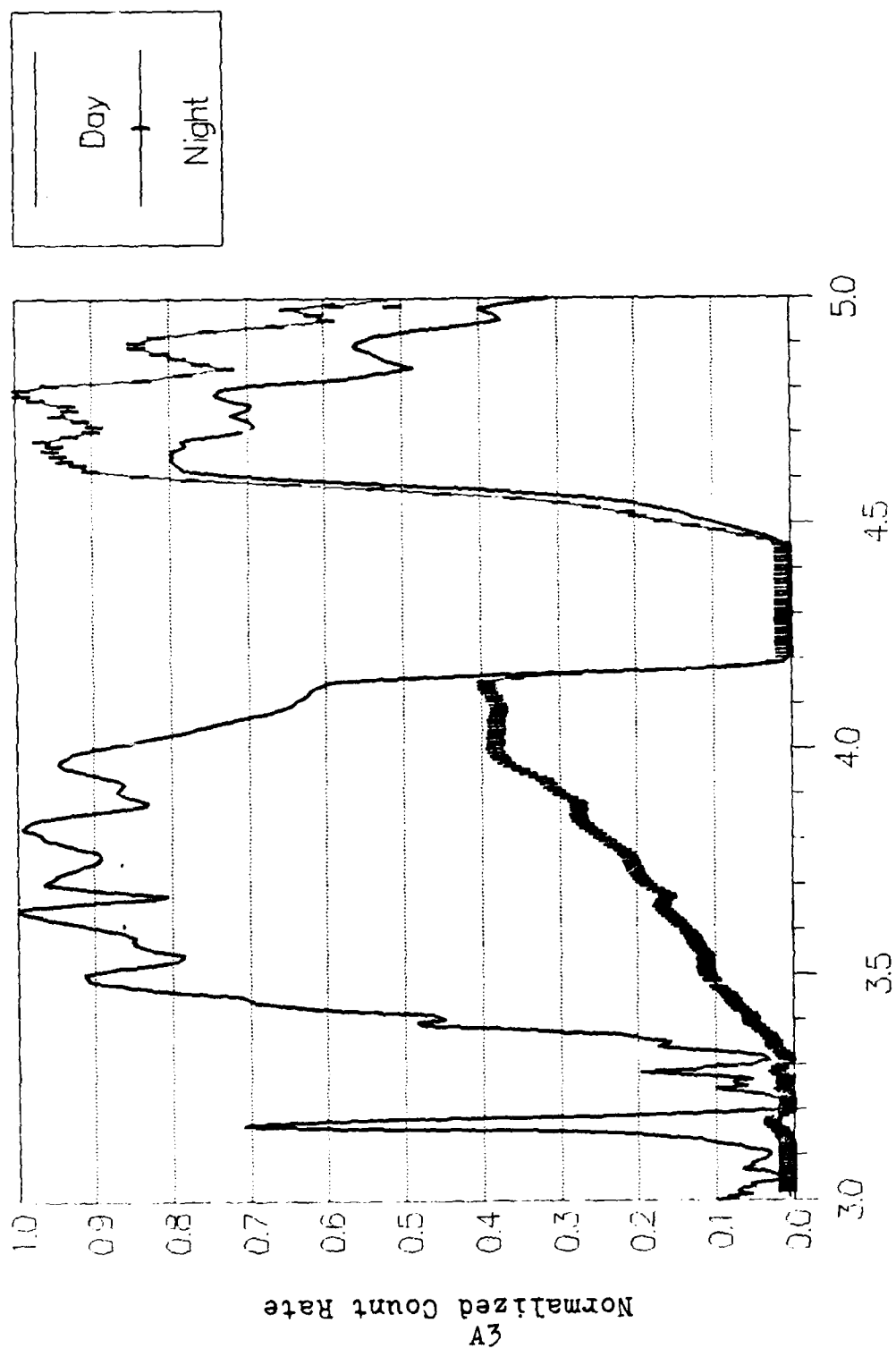


Figure A2. InSb 288K Scenario, Day vs Night

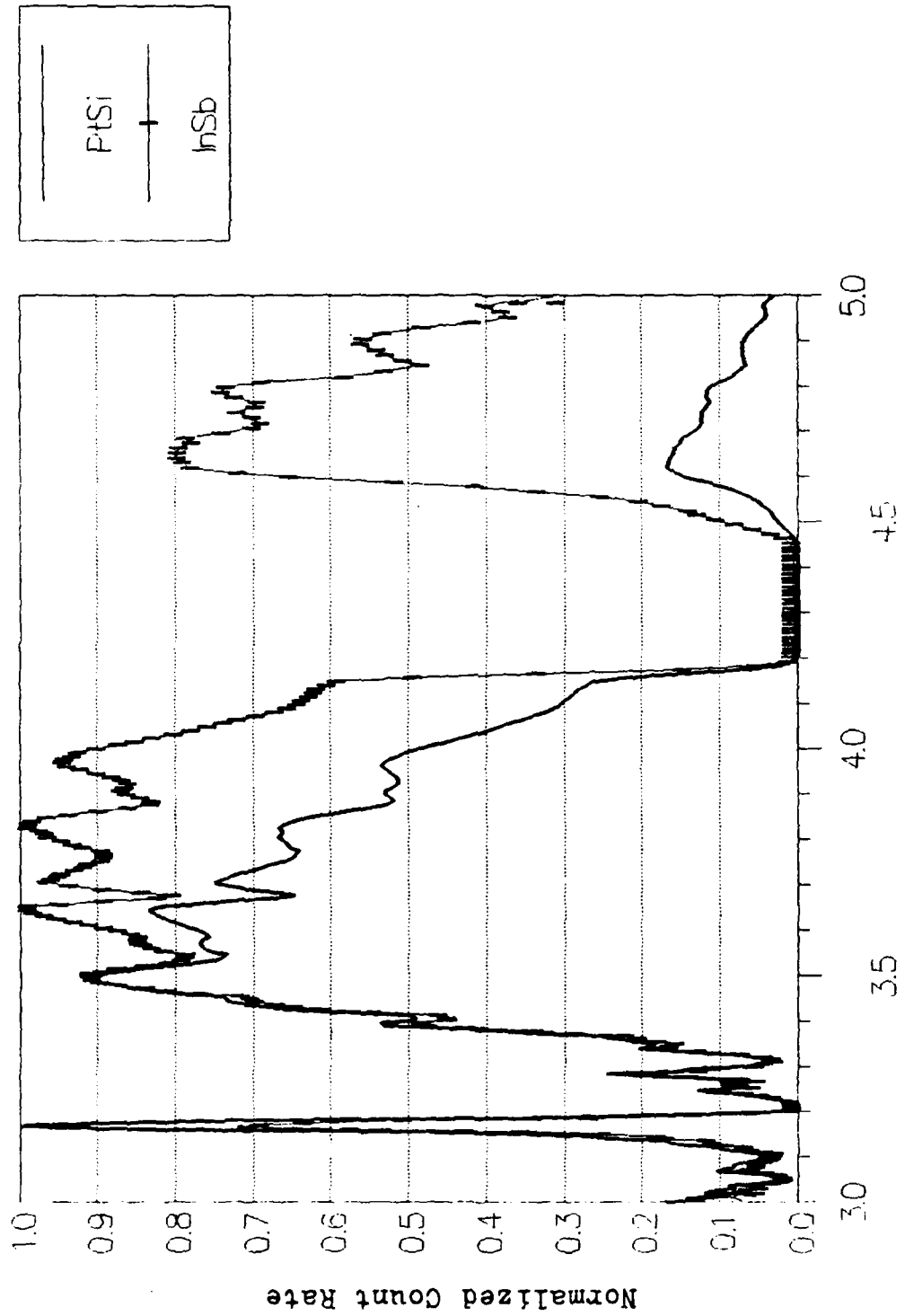


Figure A3. Day 288K Scenario, PtSi vs InSb

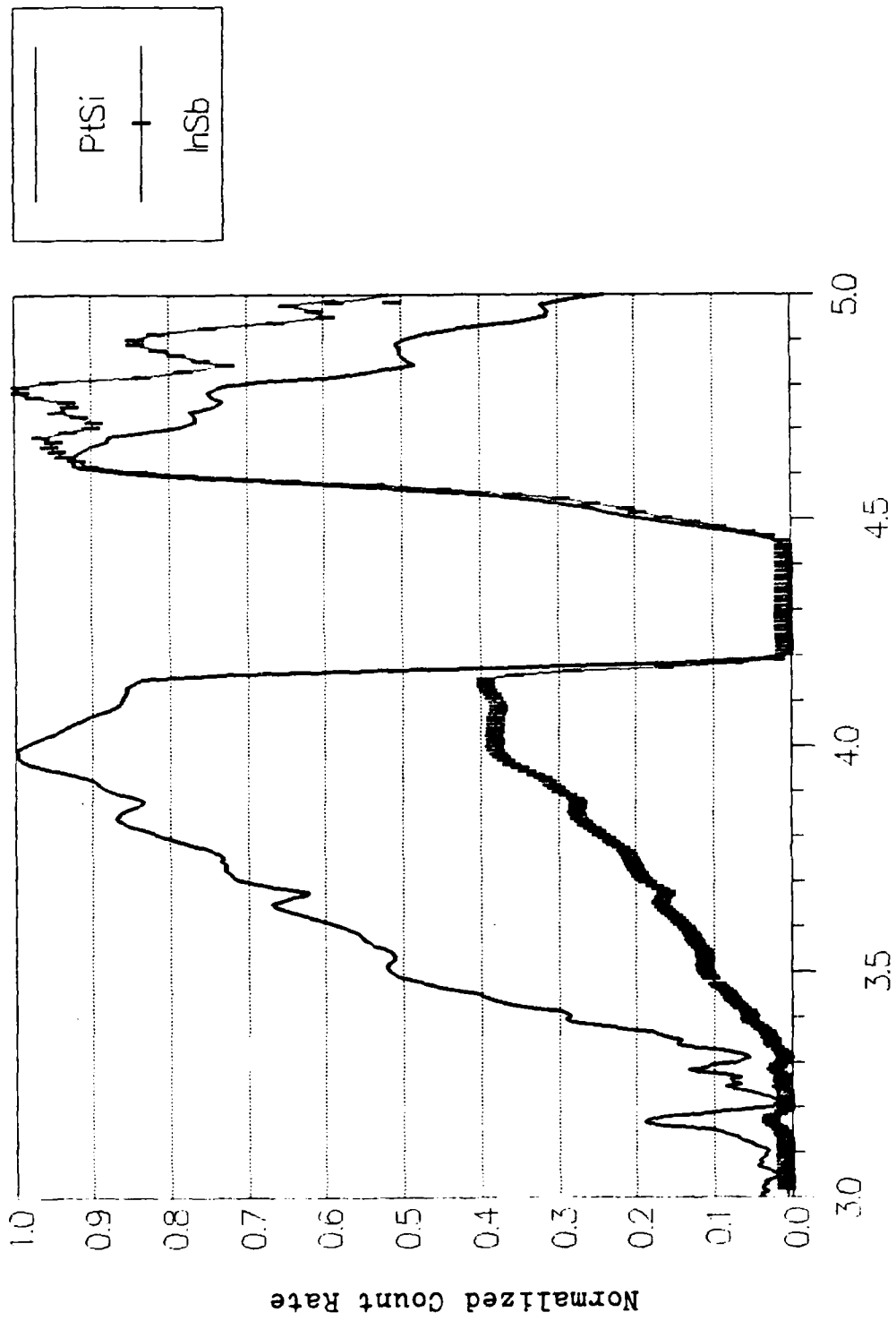


Figure A4. Night 288K Scenario, PtSi vs InSb

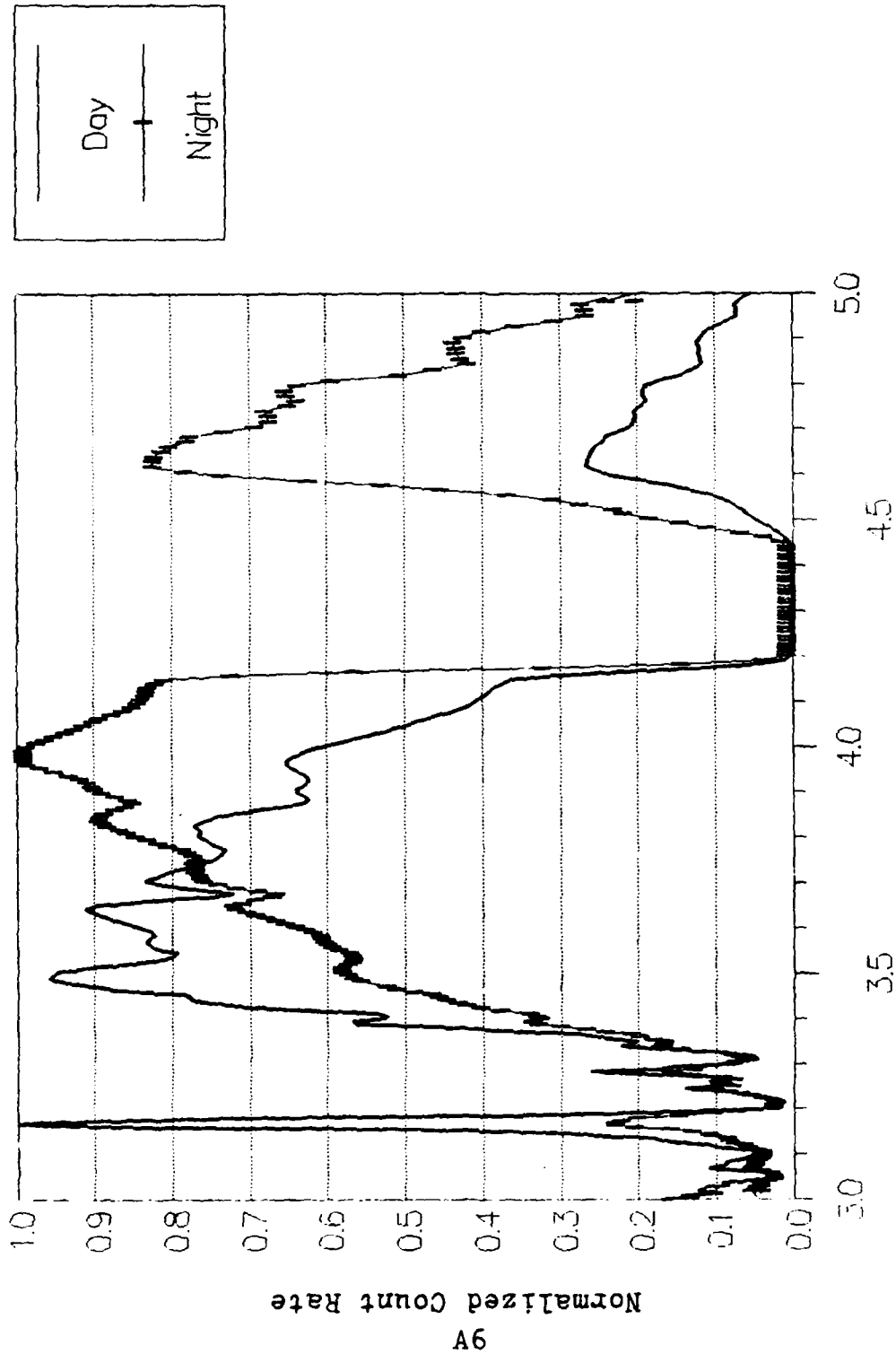


Figure A5. PtS1 308K Scenario, Day vs Night

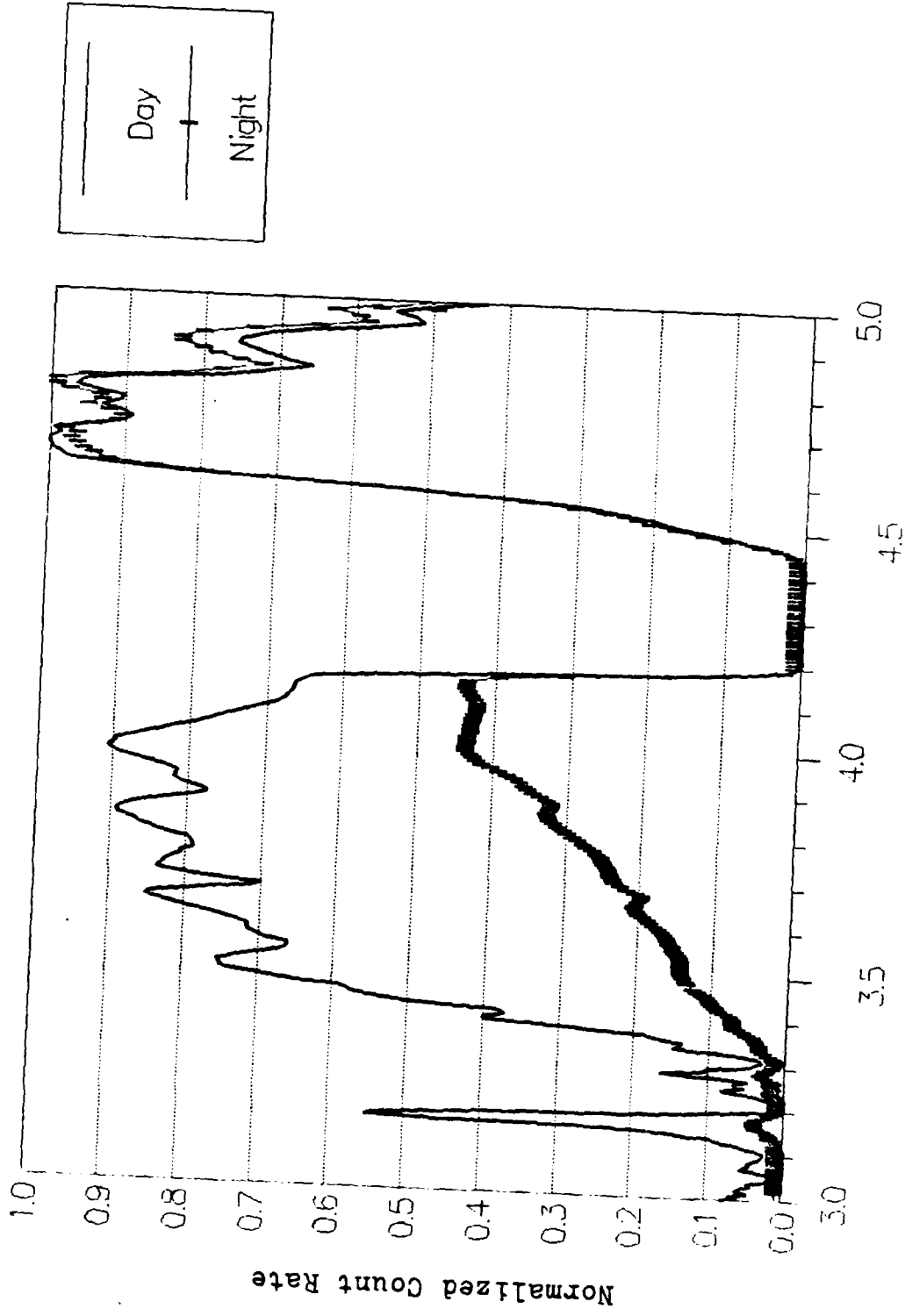
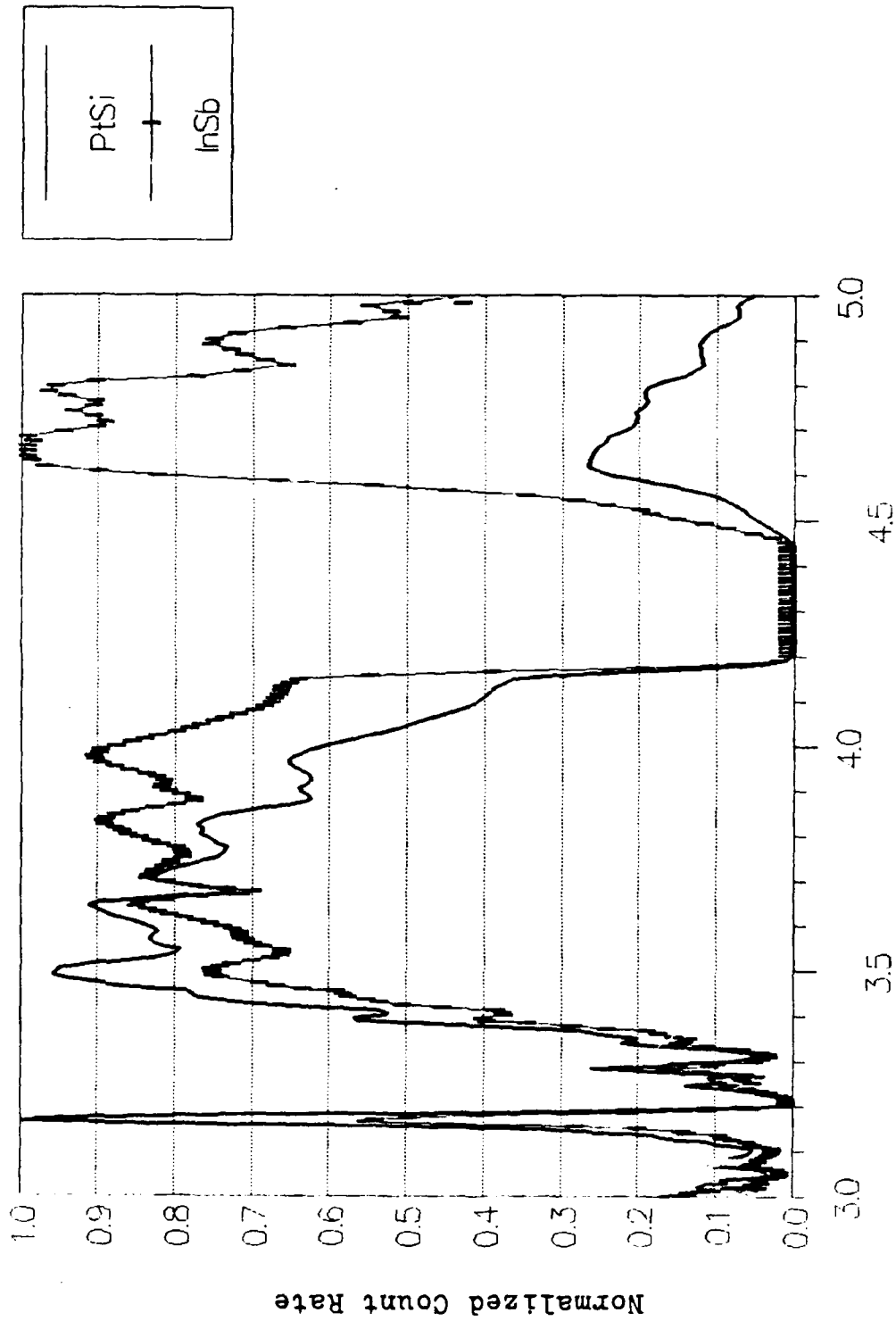


Figure A6. InSb 308K Scenario, Day vs Night



Wavelength (micrometers)

Figure A7. Day 308K Scenario, PtSi vs InSb

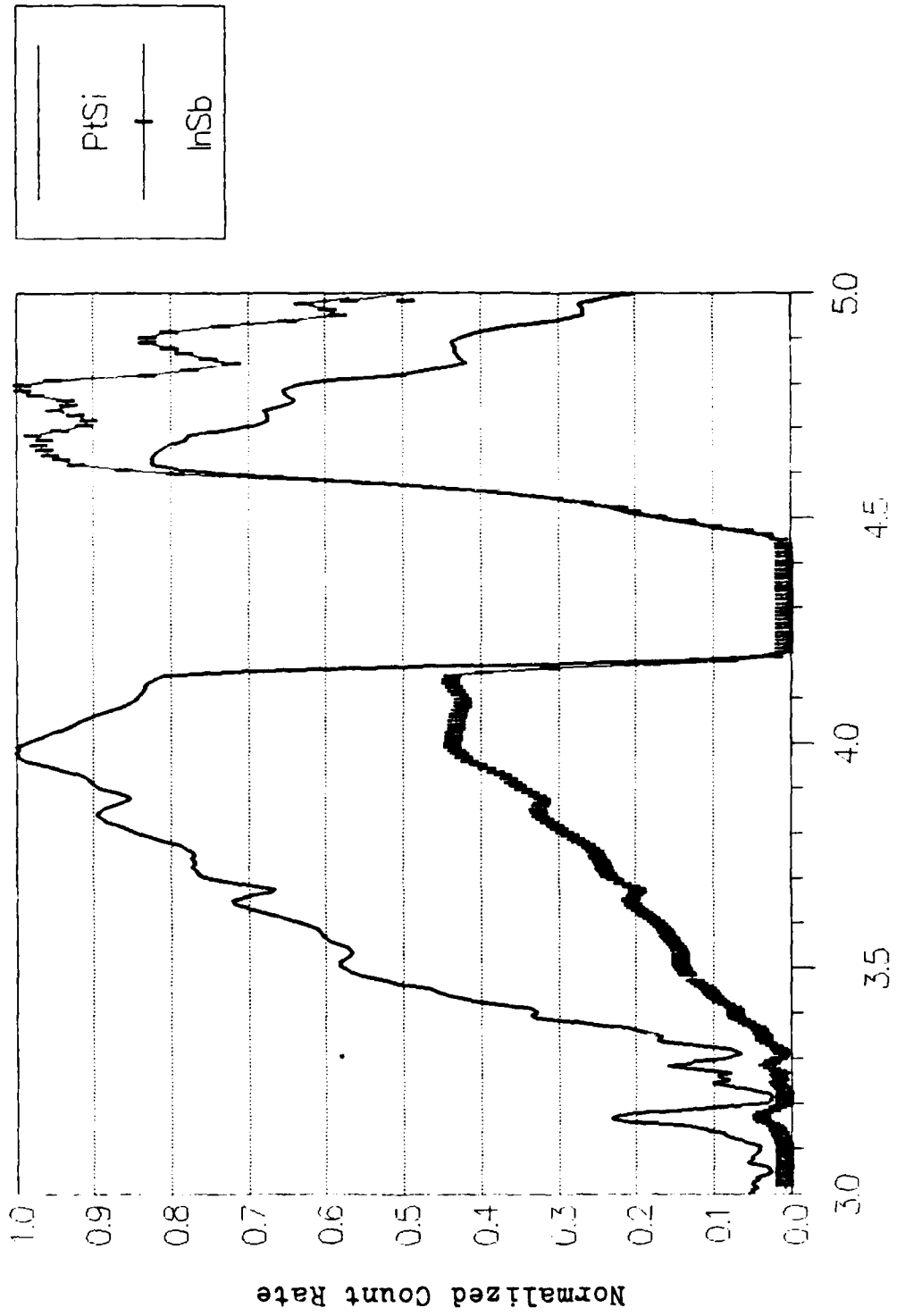


Figure A8. Night 308K Scenario, PtSi vs InSb

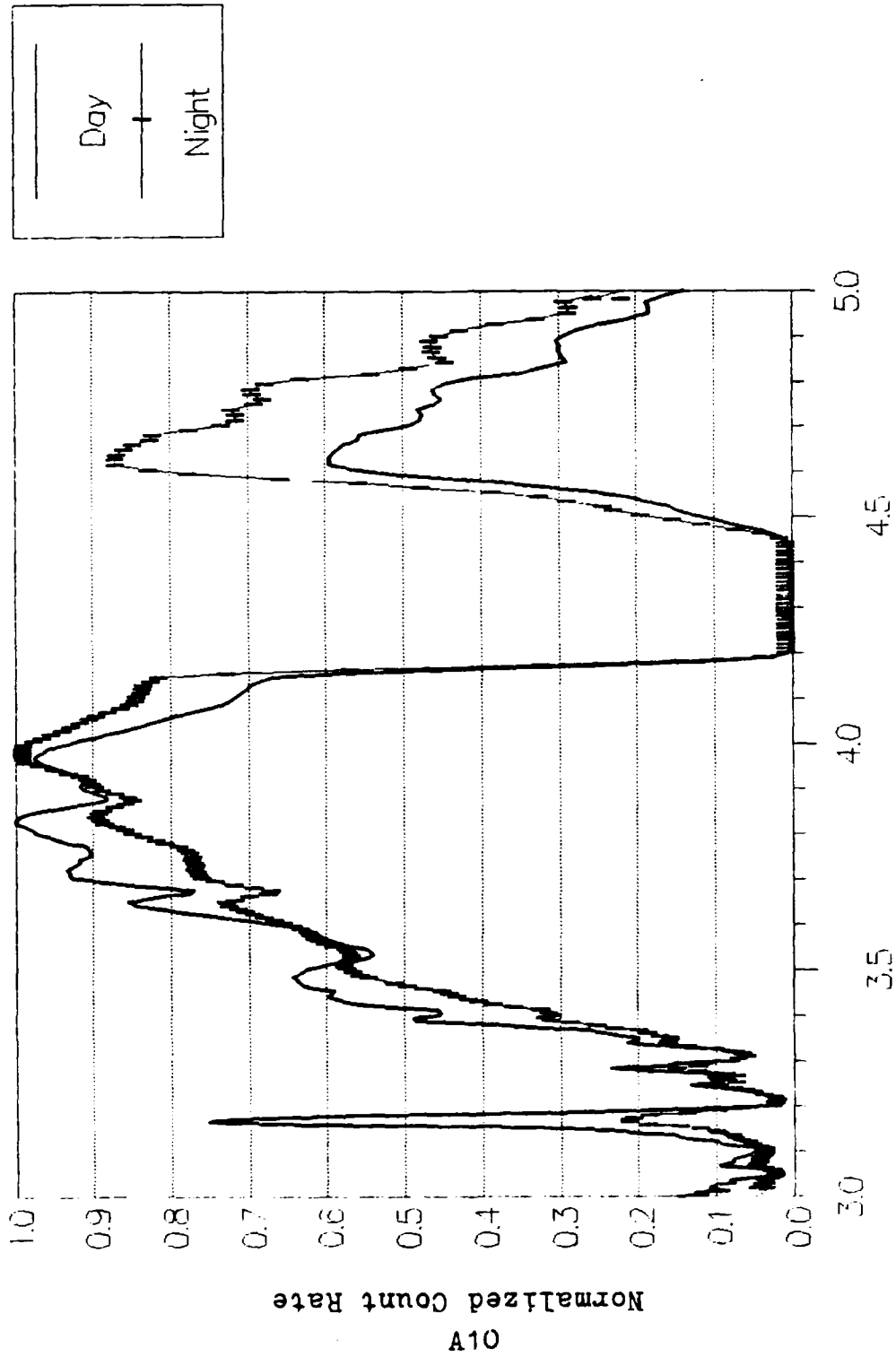


Figure A9. PtSi -1 Standard Deviation Reflectance Scenario, Day vs Night

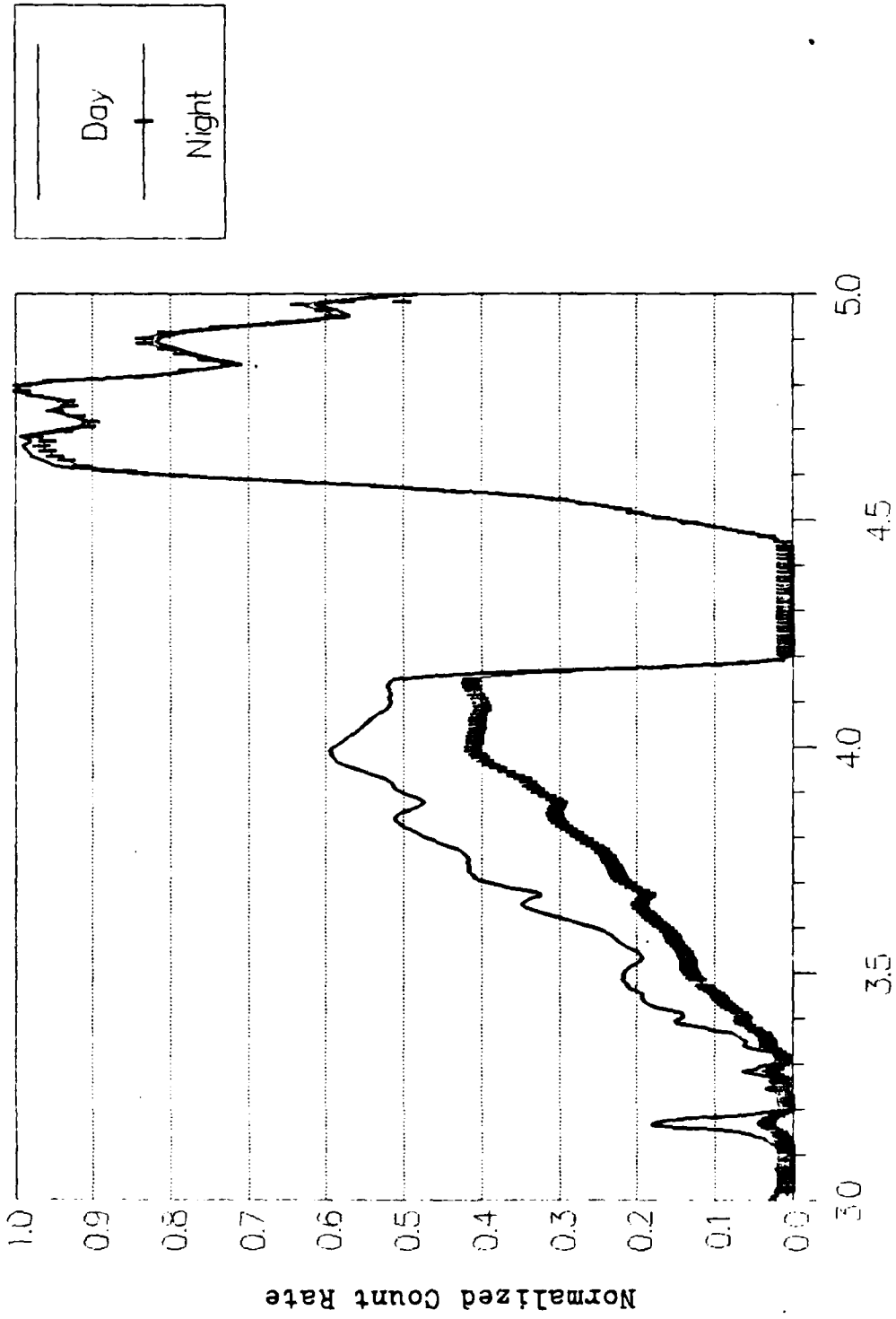


Figure A10. InSb -1 Standard Deviation Reflectance Scenario, Day vs Night

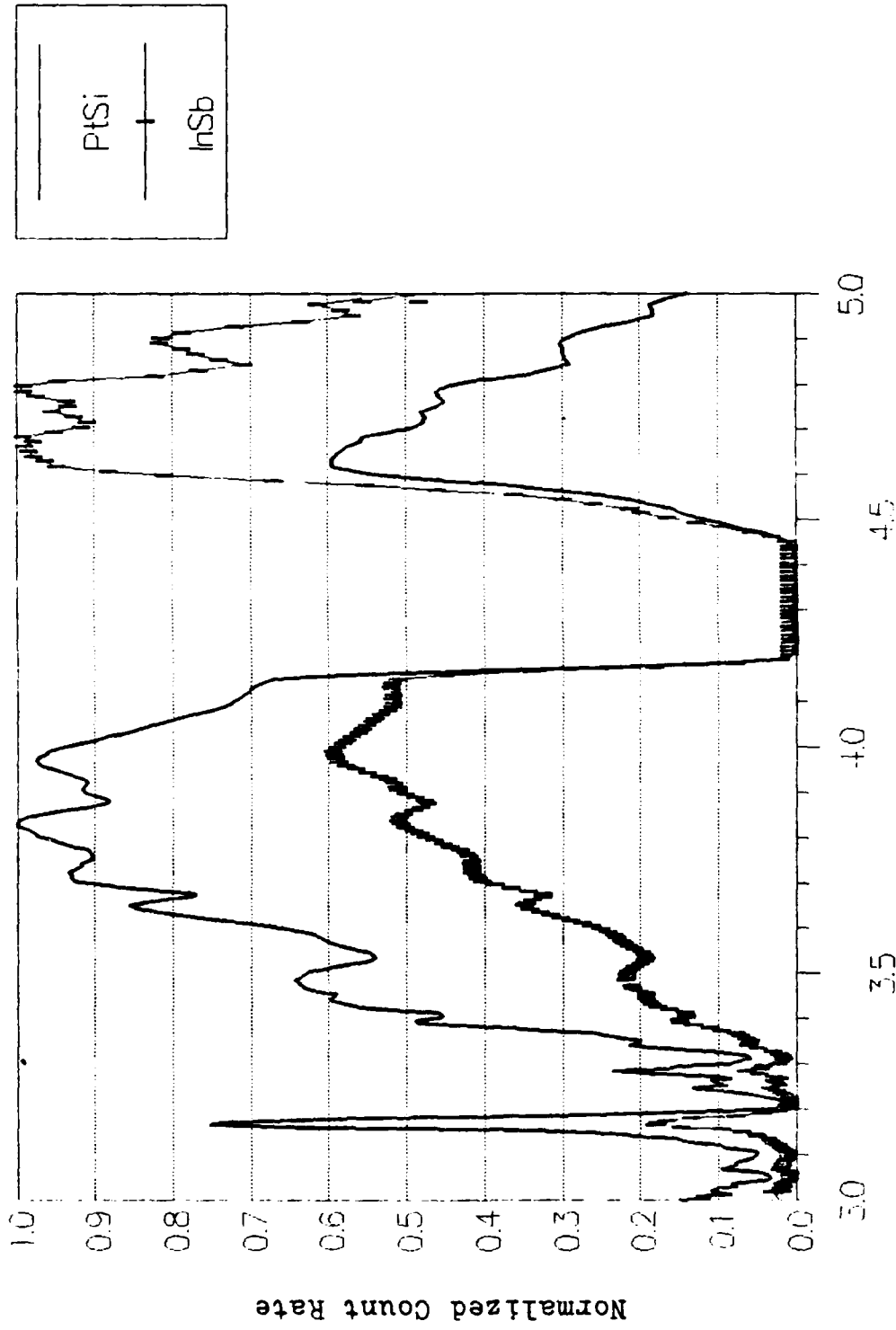


Figure A11. Day -1 Standard Deviation Reflectance Scenario, PtSi vs InSb

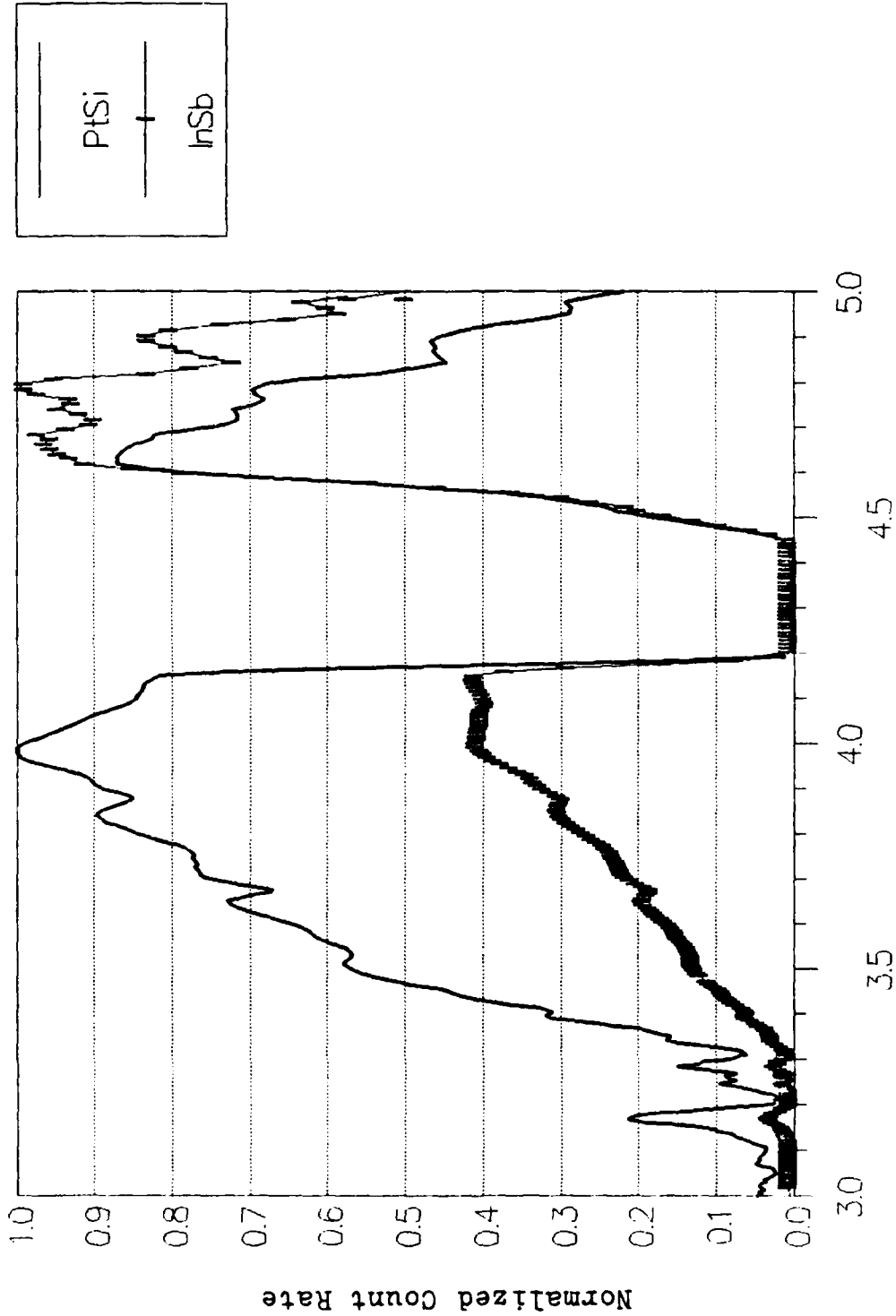


Figure A12. Night -1 Standard Deviation Reflectance Scenario, PtSi vs InSb

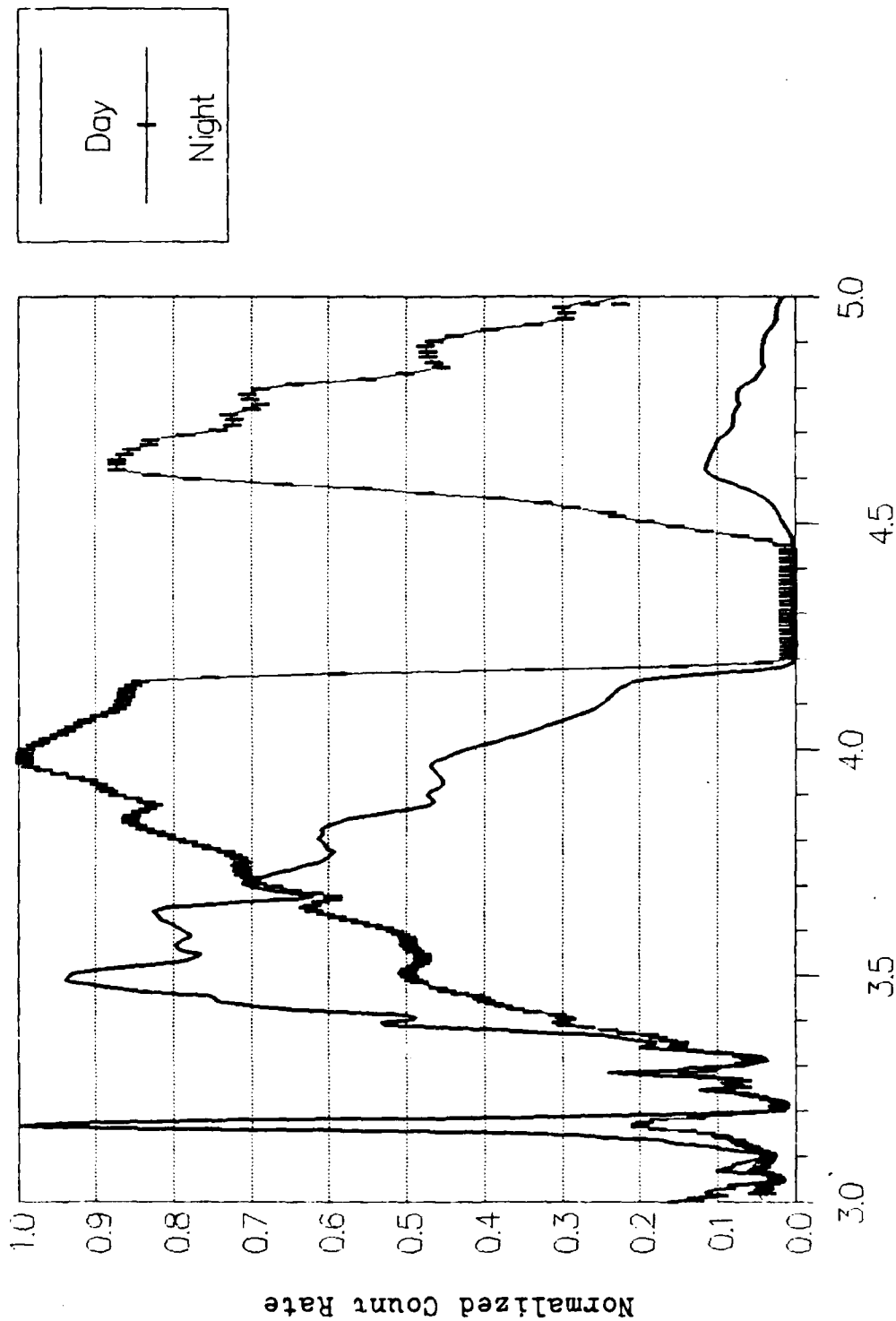


Figure A13. PtSi +1 Standard Deviation Reflectance Scenario, Day vs Night

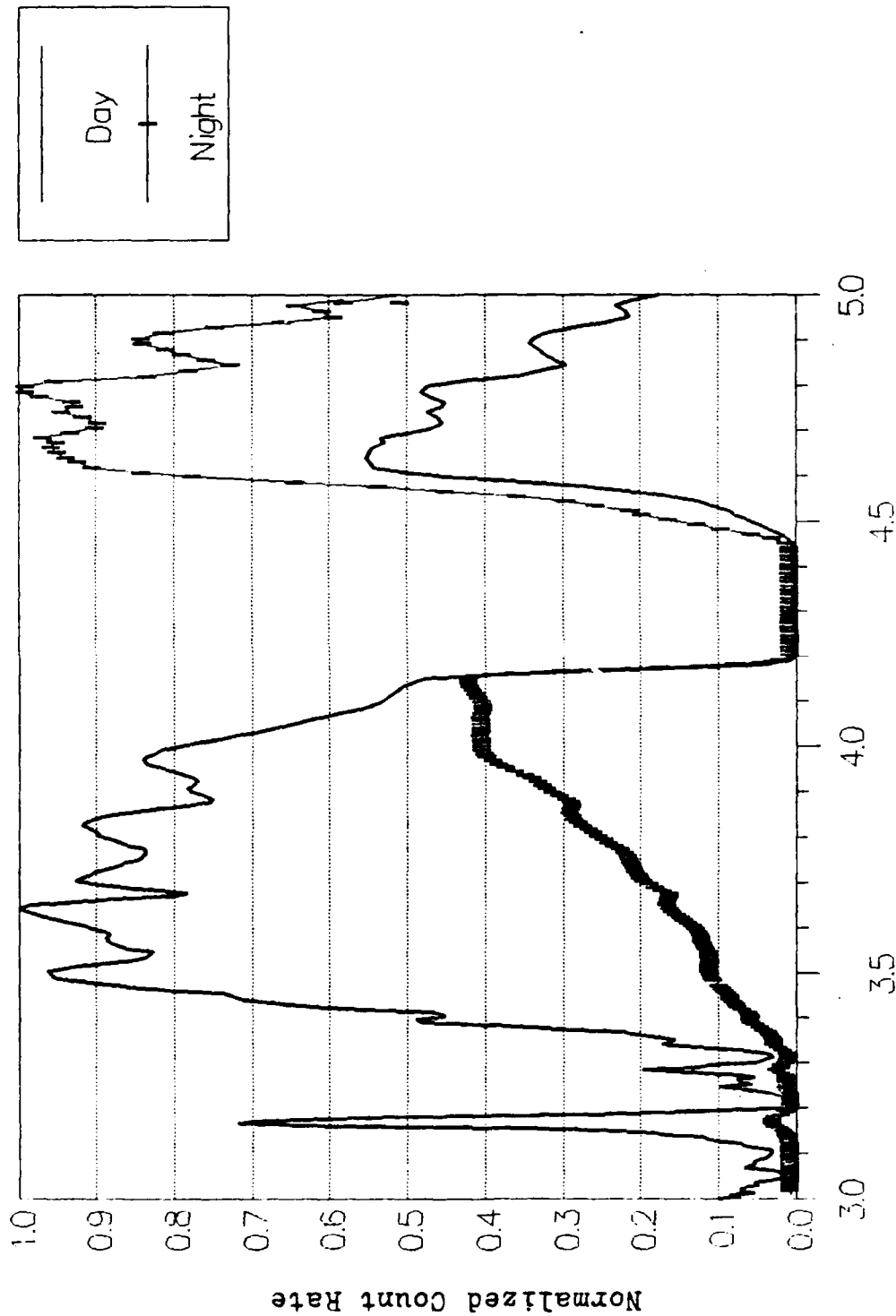


Figure A14. Ir:5b +1 Standard Deviation on Reflectance Scenario, Day vs Night

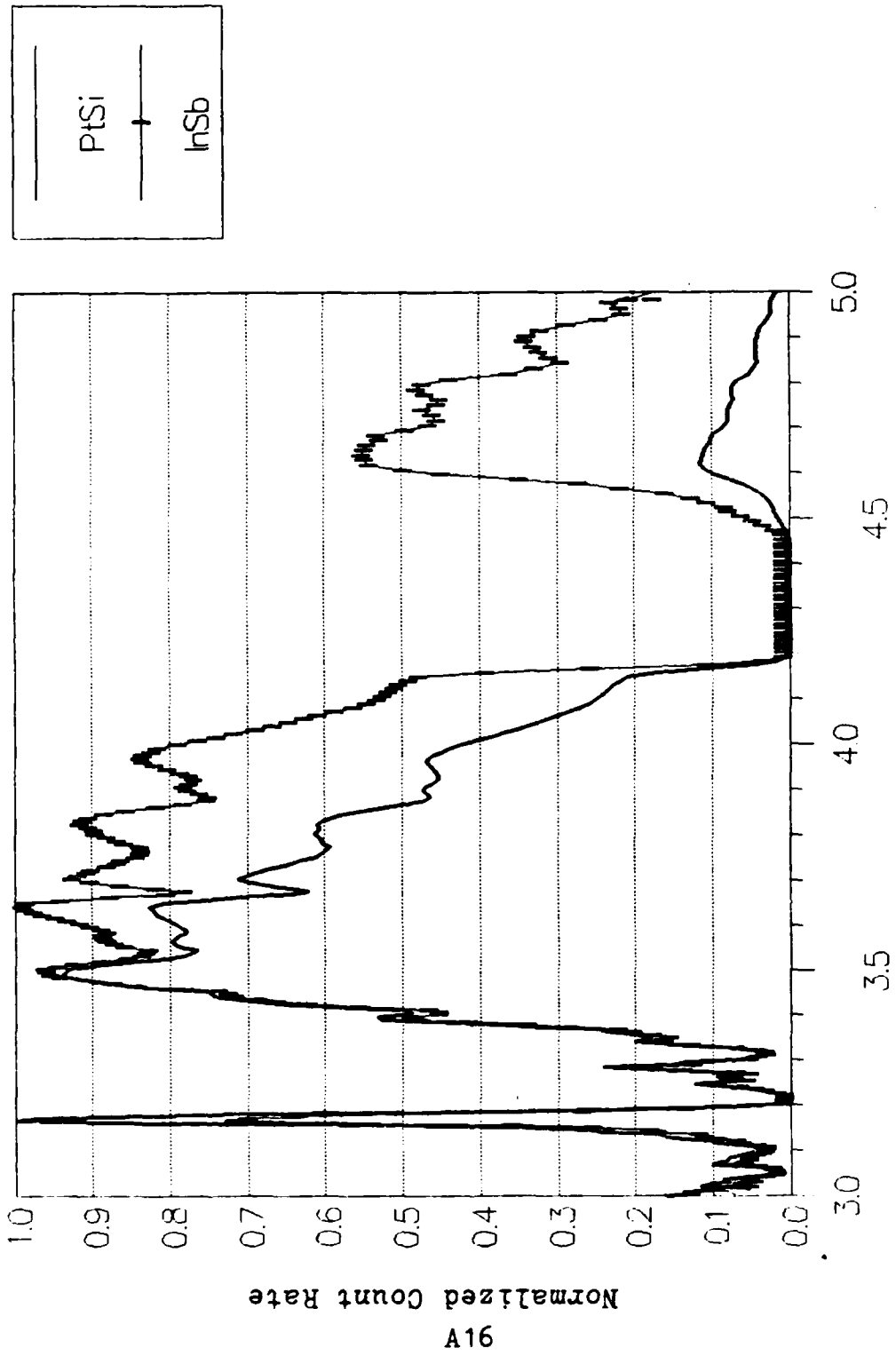


Figure A15. Day +1 Standard Deviation Reflectance Scenario, PtSi vs InSb

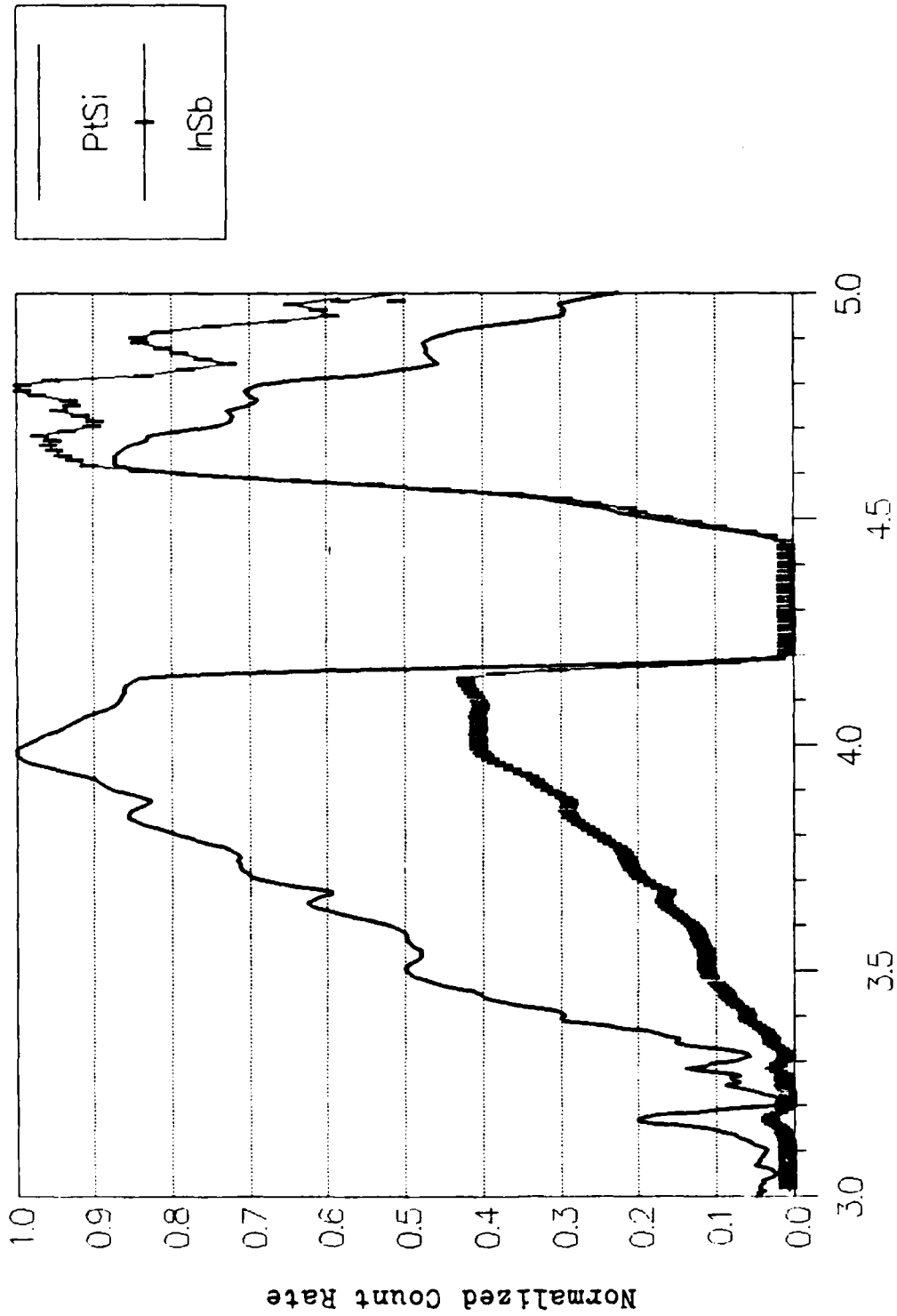


Figure A16. Night +1 Standard Deviation Reflectance Scenario, PtSi vs InSb

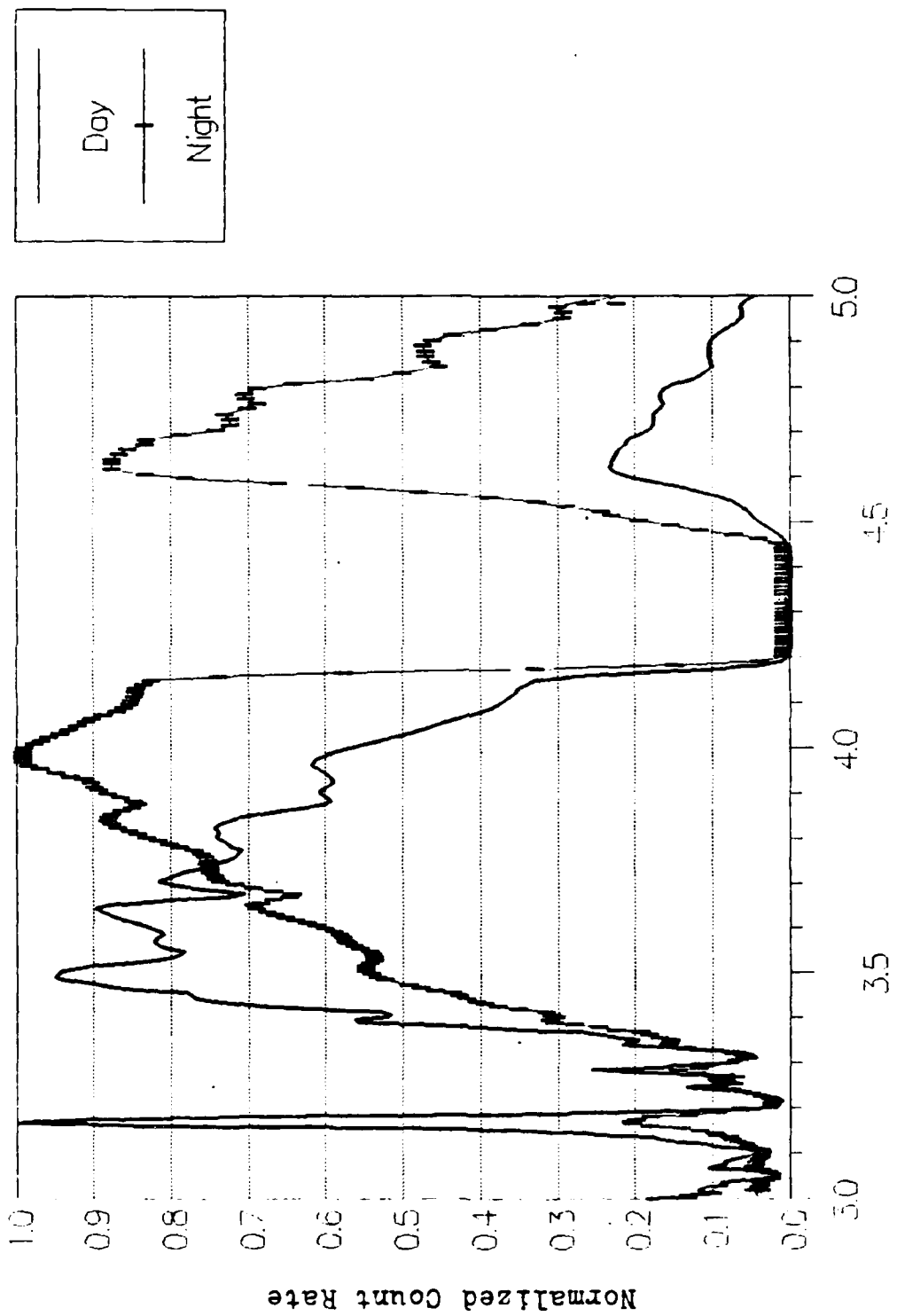


Figure A17. PtSI Rural 5 Km Visibility Scenario, Day vs Night

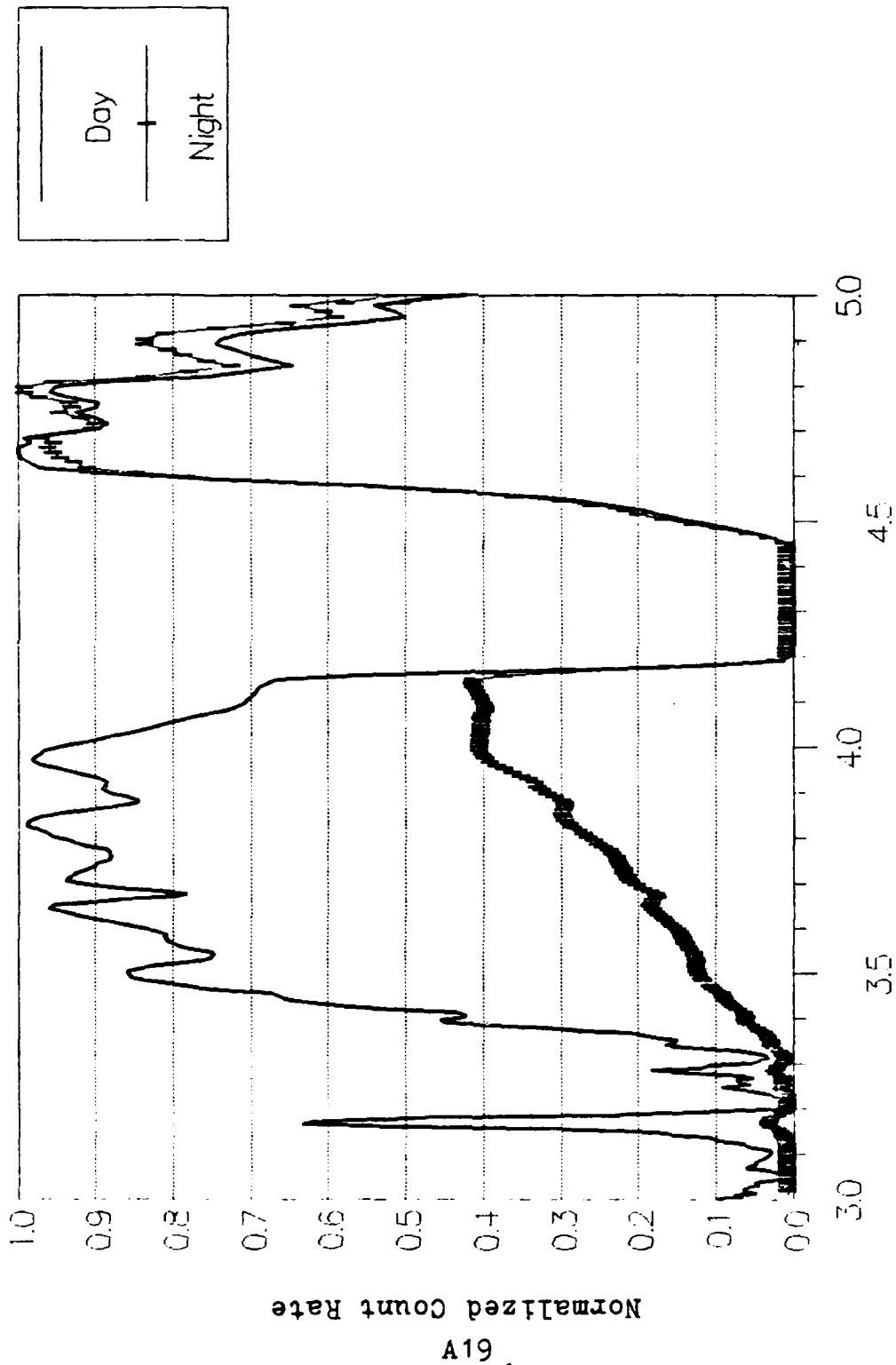


Figure A 18. InSb Rural 5 Km Visibility Scenario, Day vs Night

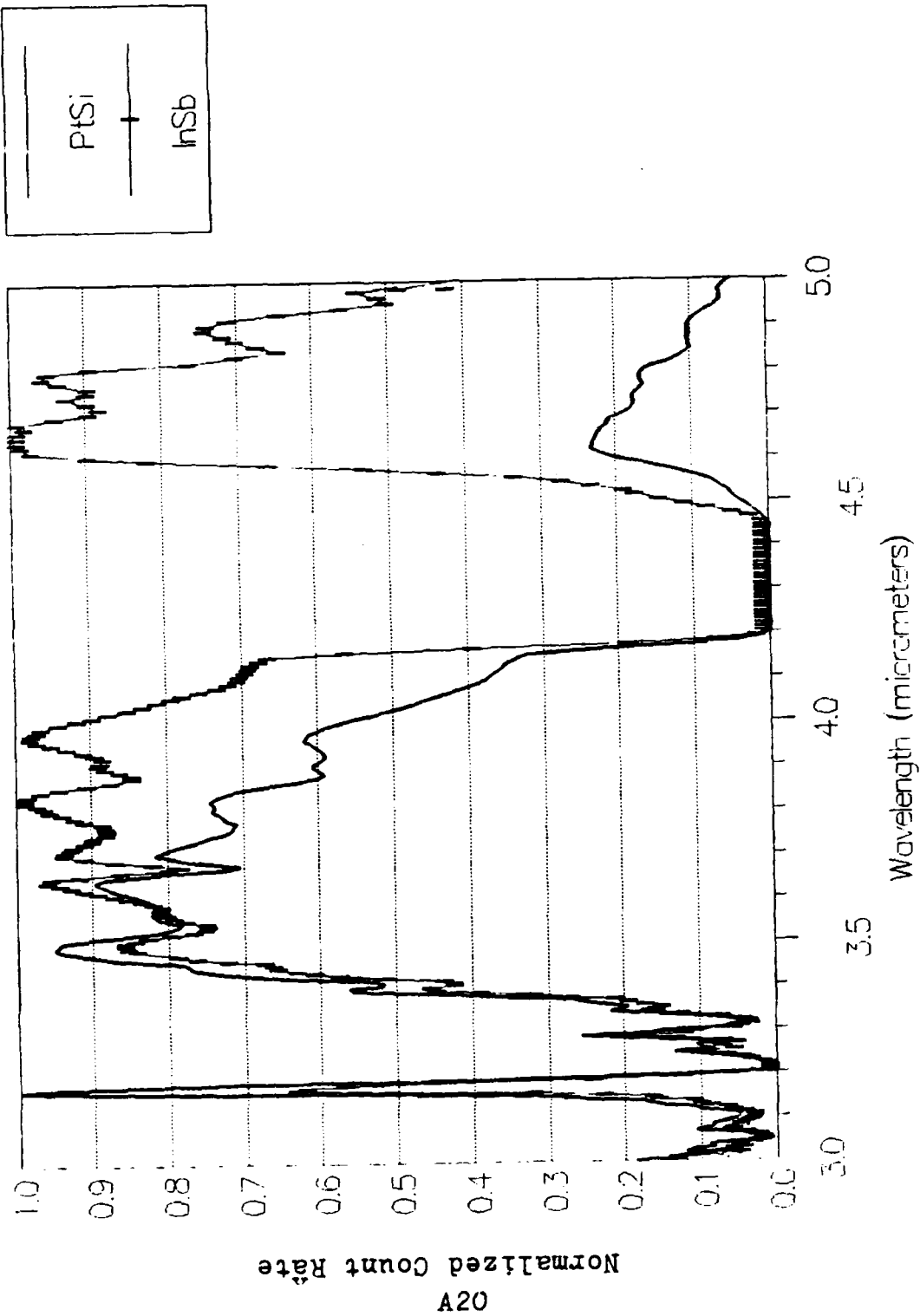


Figure A19. Day Rural 5 Km Visibility Scenario, PtSi vs InSb

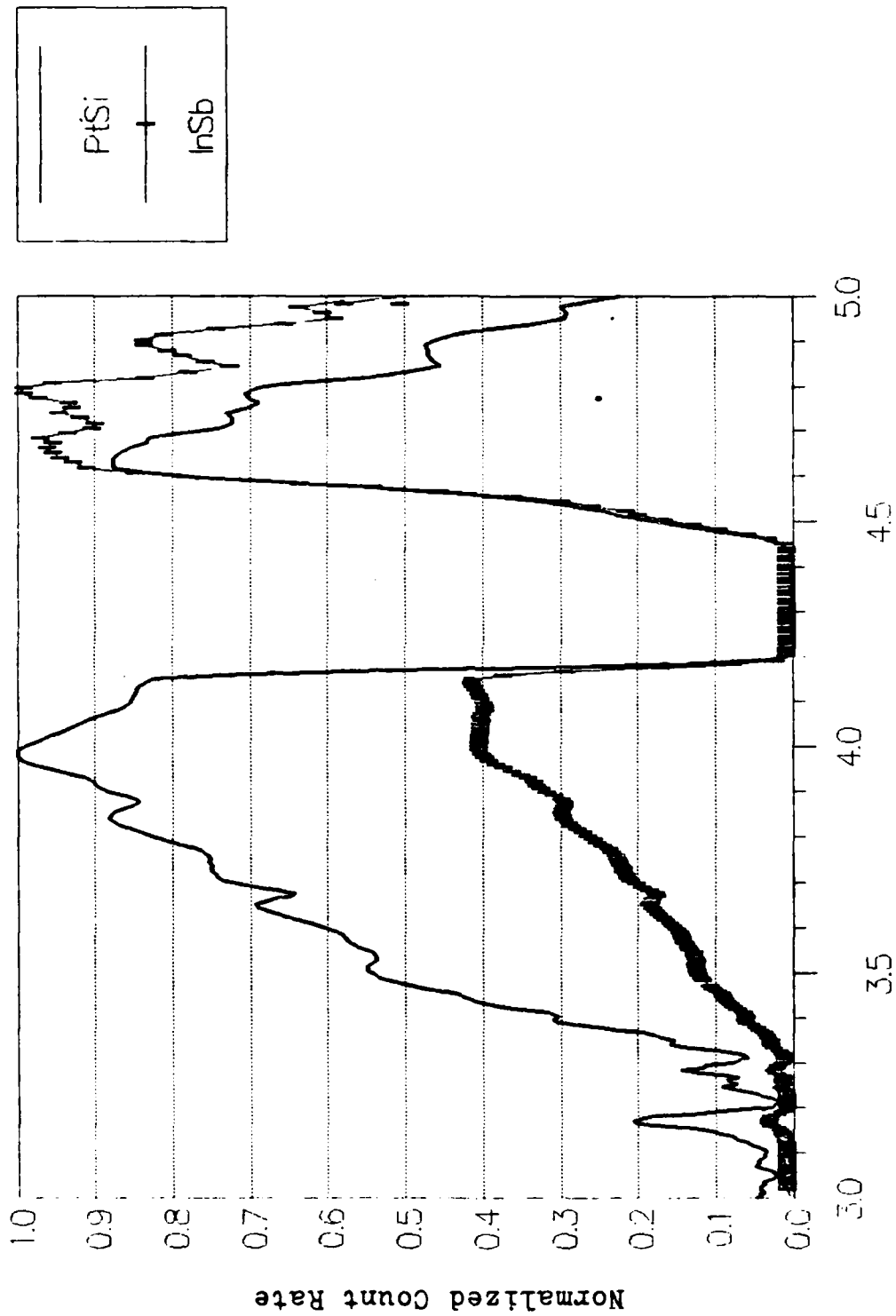


Figure A20. Night Rural 5 Km Visibility Scenario, PtSi vs InSb

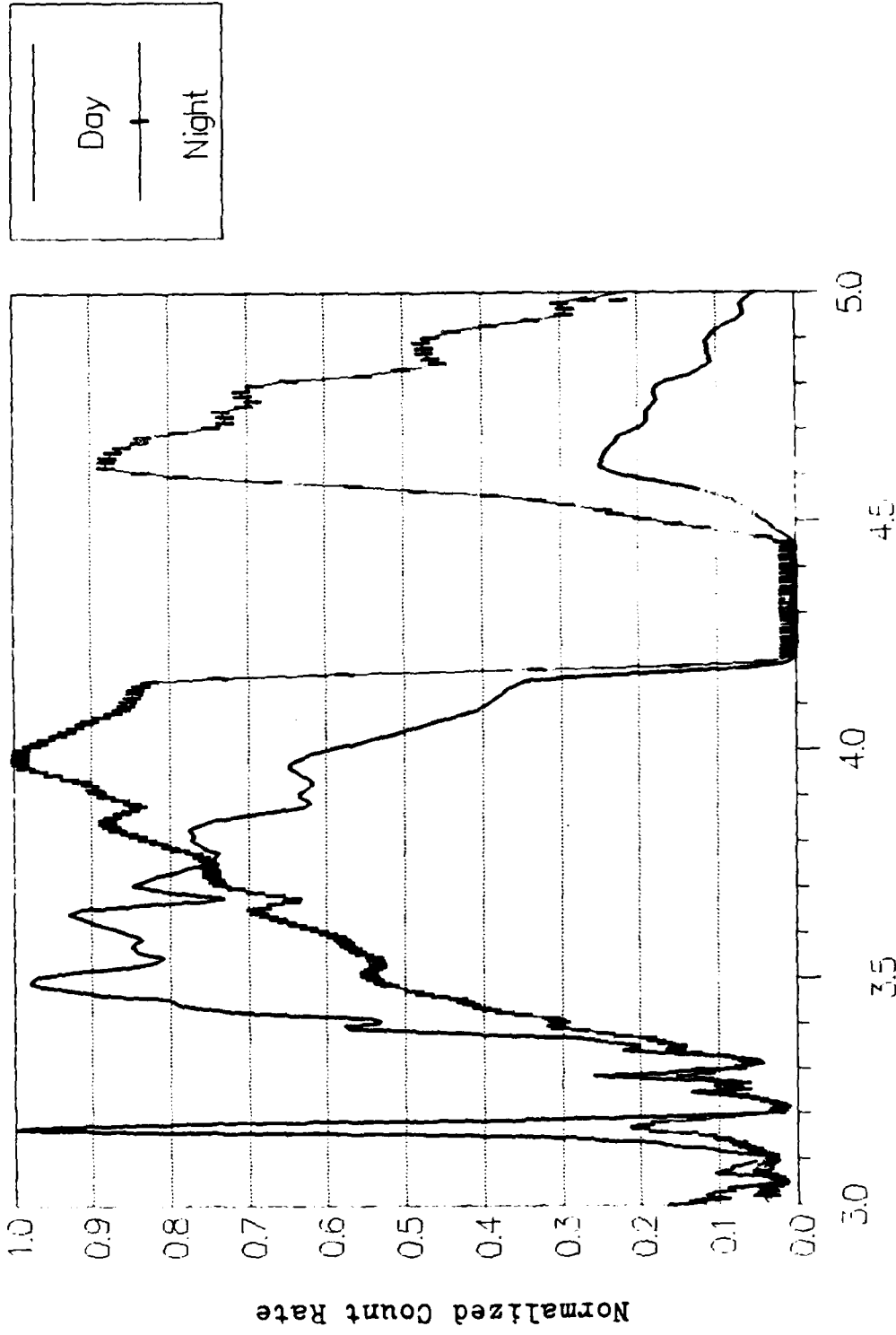


Figure A21. PtSI Urban 5 Km Visibility Scenario, Day vs Night

Day  
Night

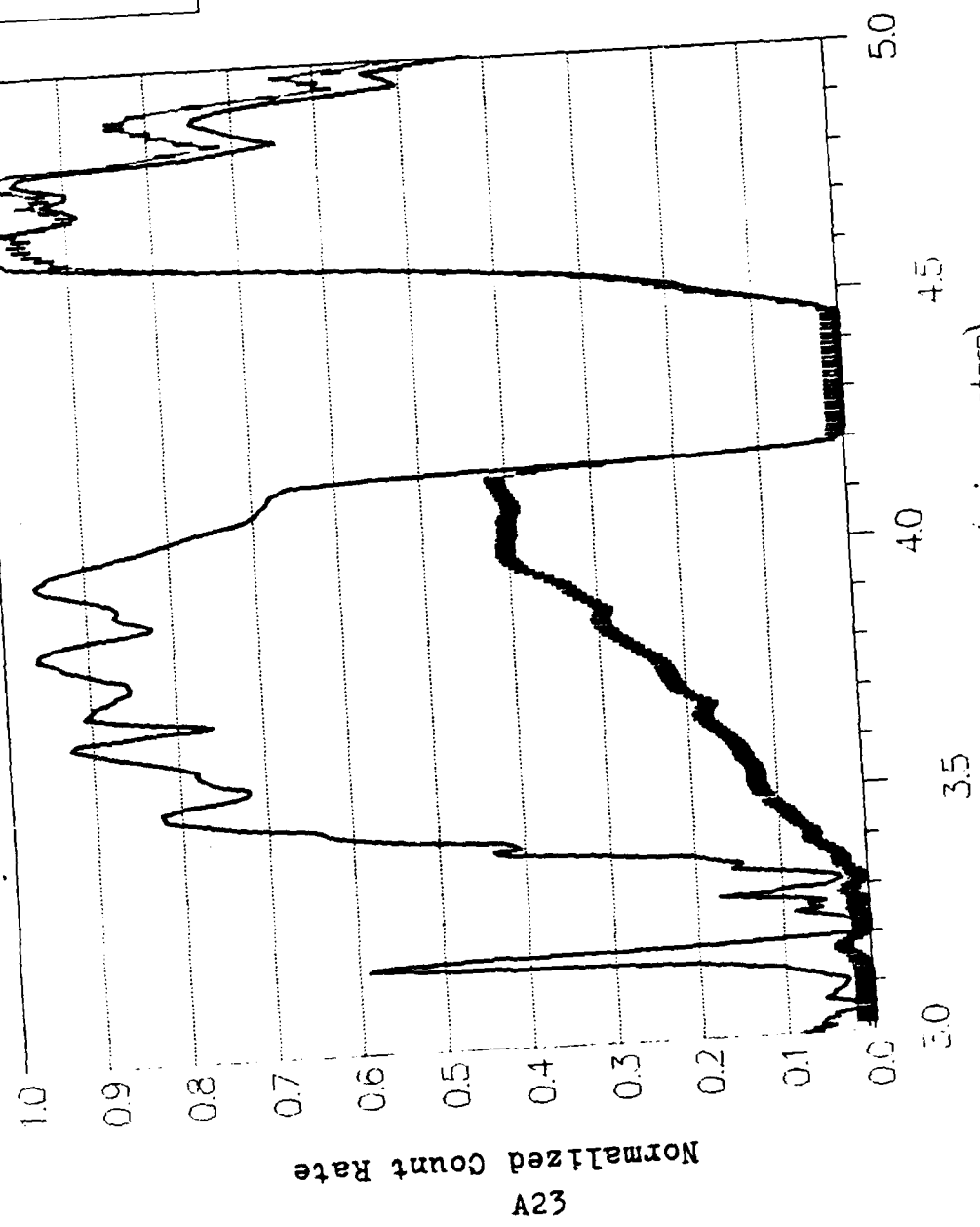


Figure A22. InSb Urban 5 Km Visibility Scenario,  
Day vs Night

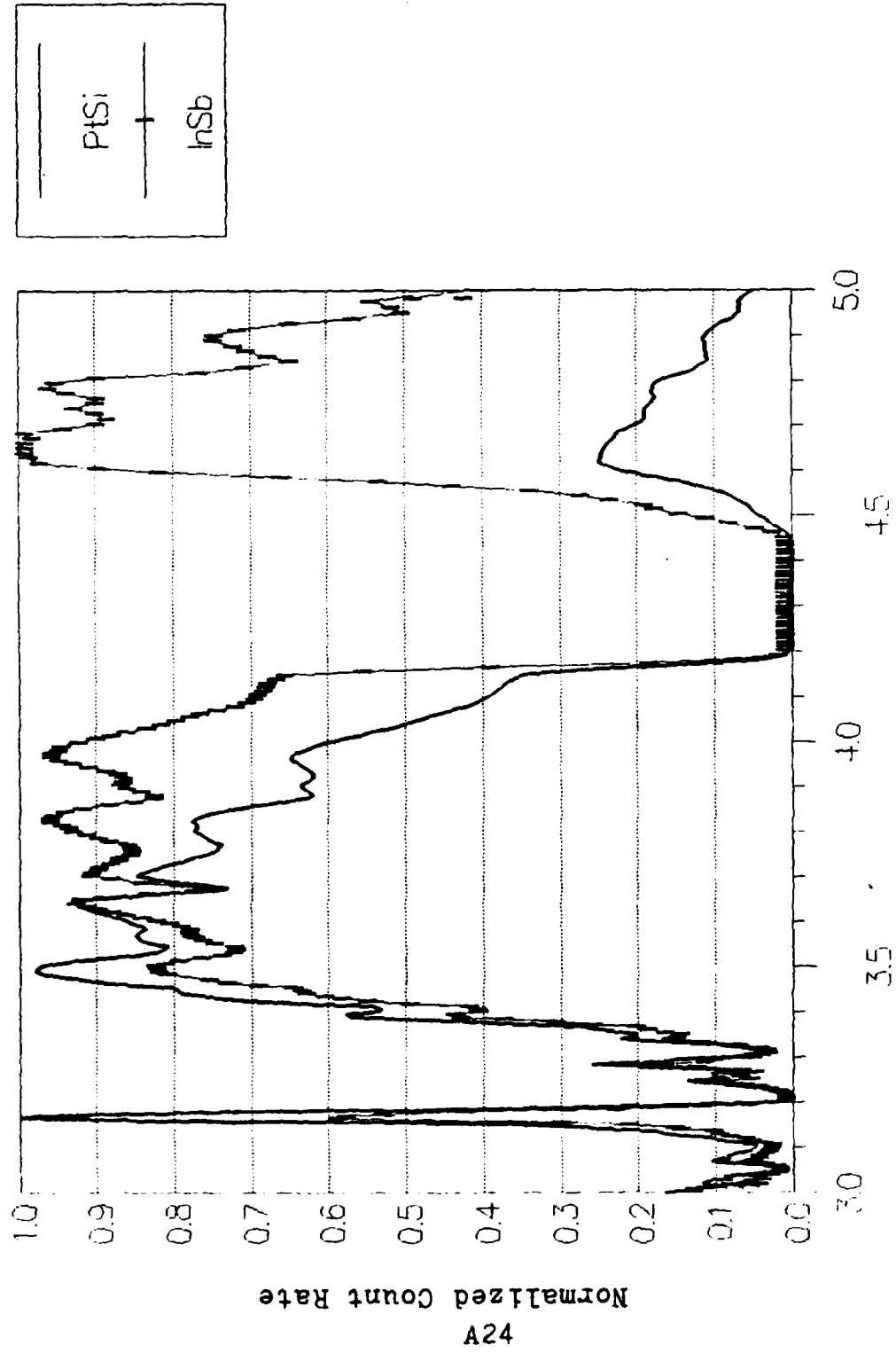


Figure A23. Day Urban 5 Km Visibility Scenario, PtSi vs InSb

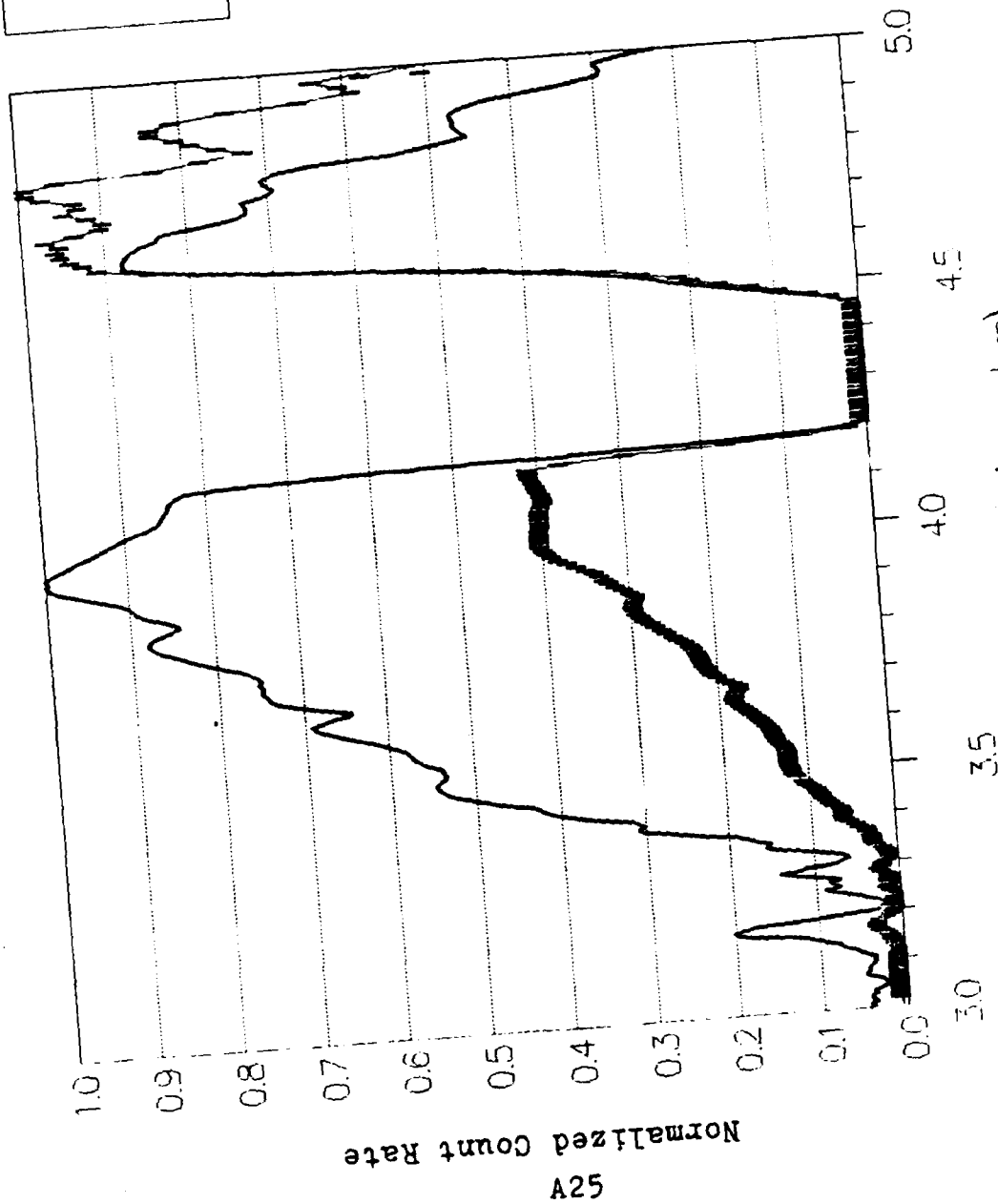
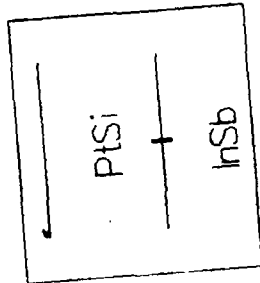
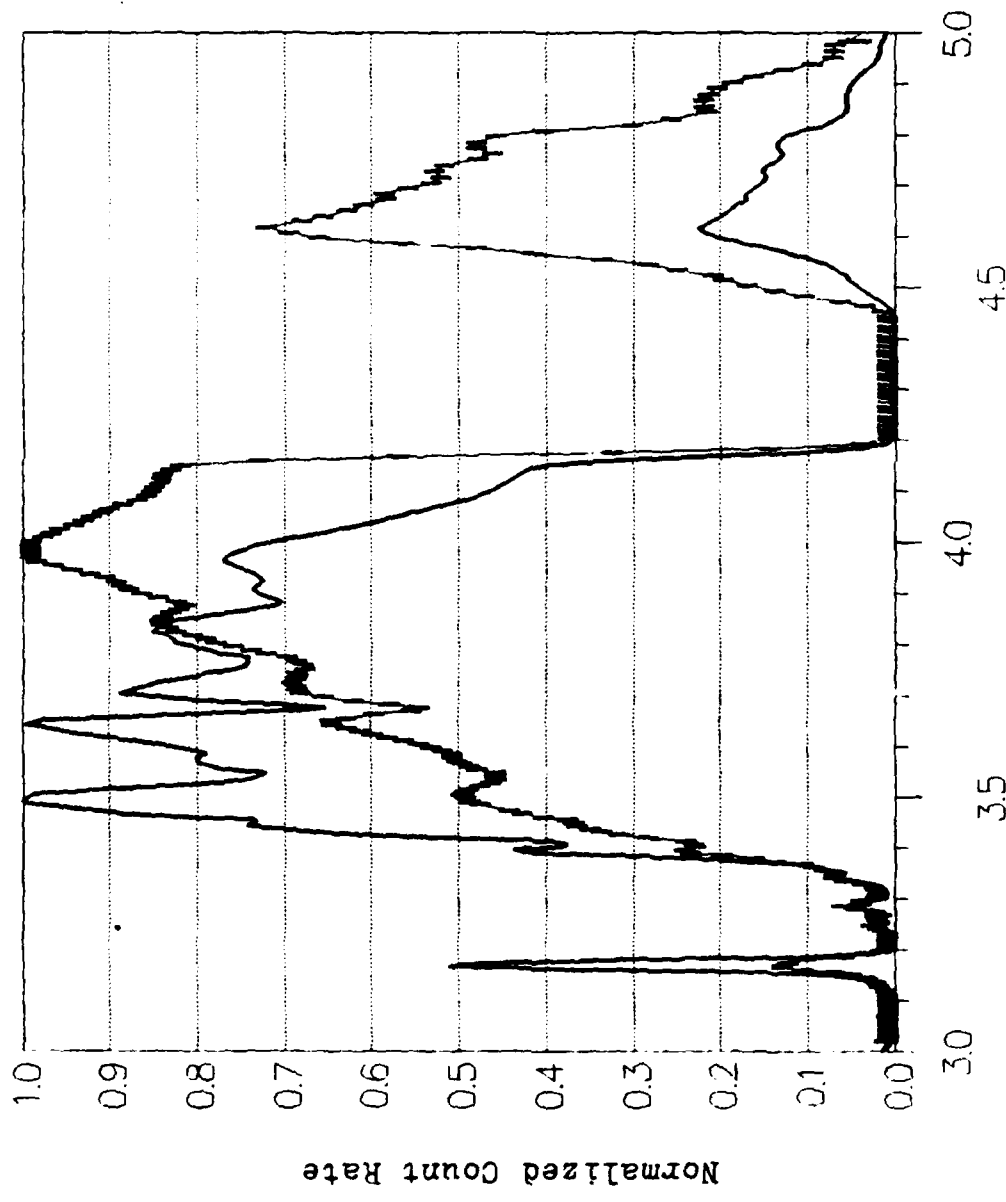


Figure A24. Night Urban 5 Km Visibility Scenario, PtSi vs InSb



Day  
Night

Figure A25. PtSi Increased Humidity Scenario, Day vs Night

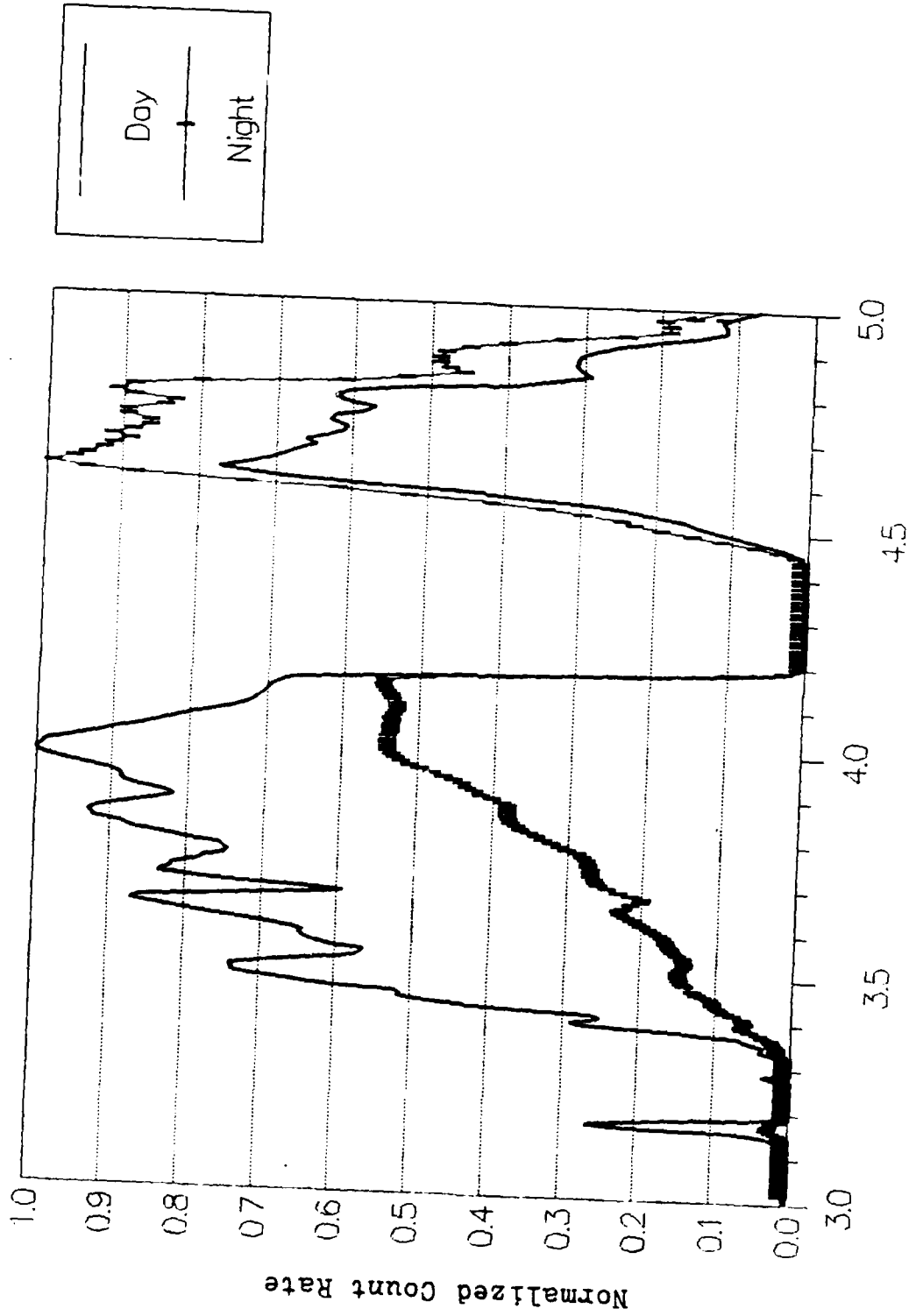


Figure A26. InSb Increased Humidity Scenario, Day vs Night

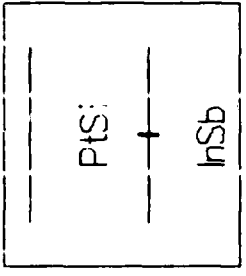
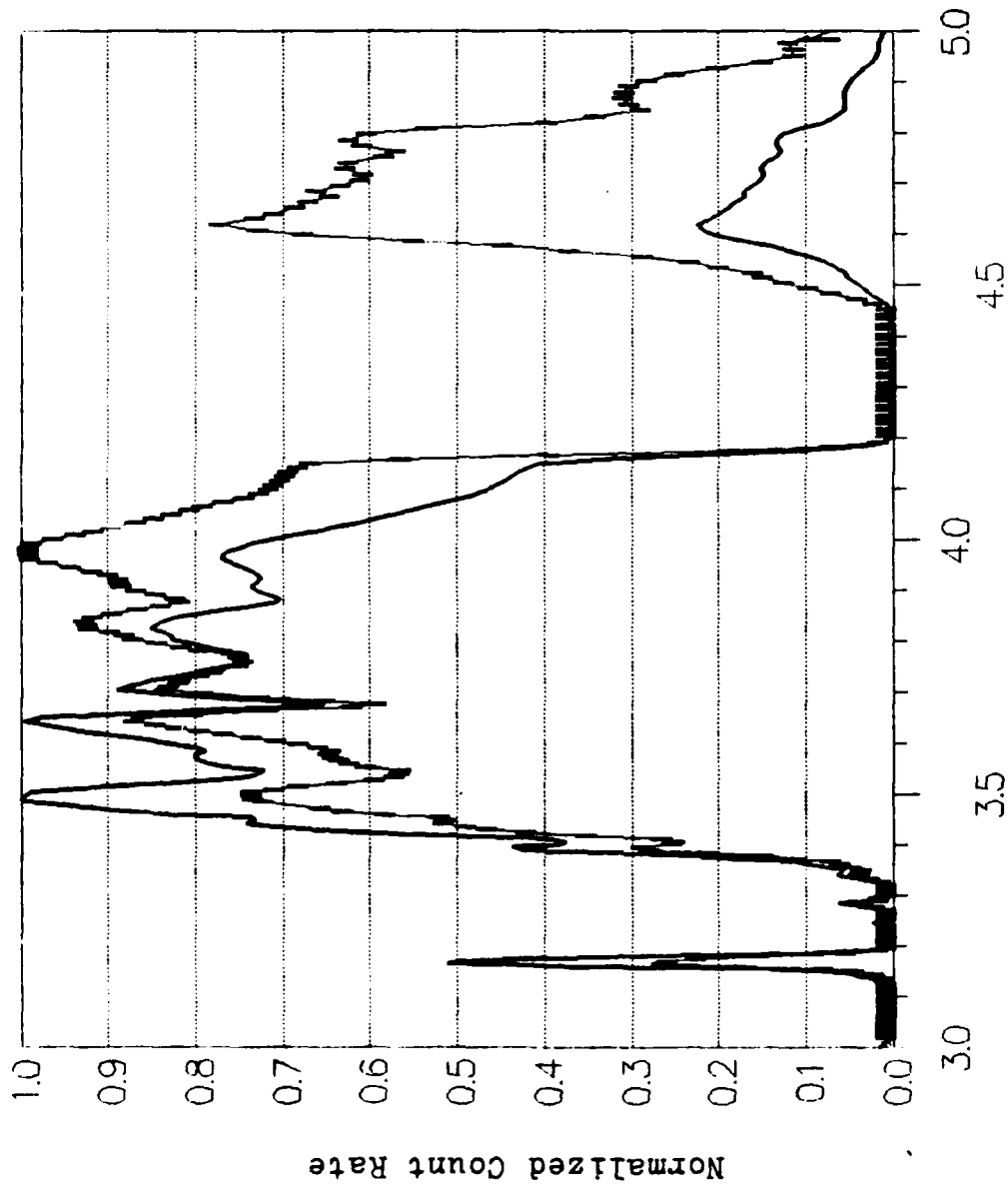


Figure A27. Day Increased Humidity Scenario, PtSi vs InSb

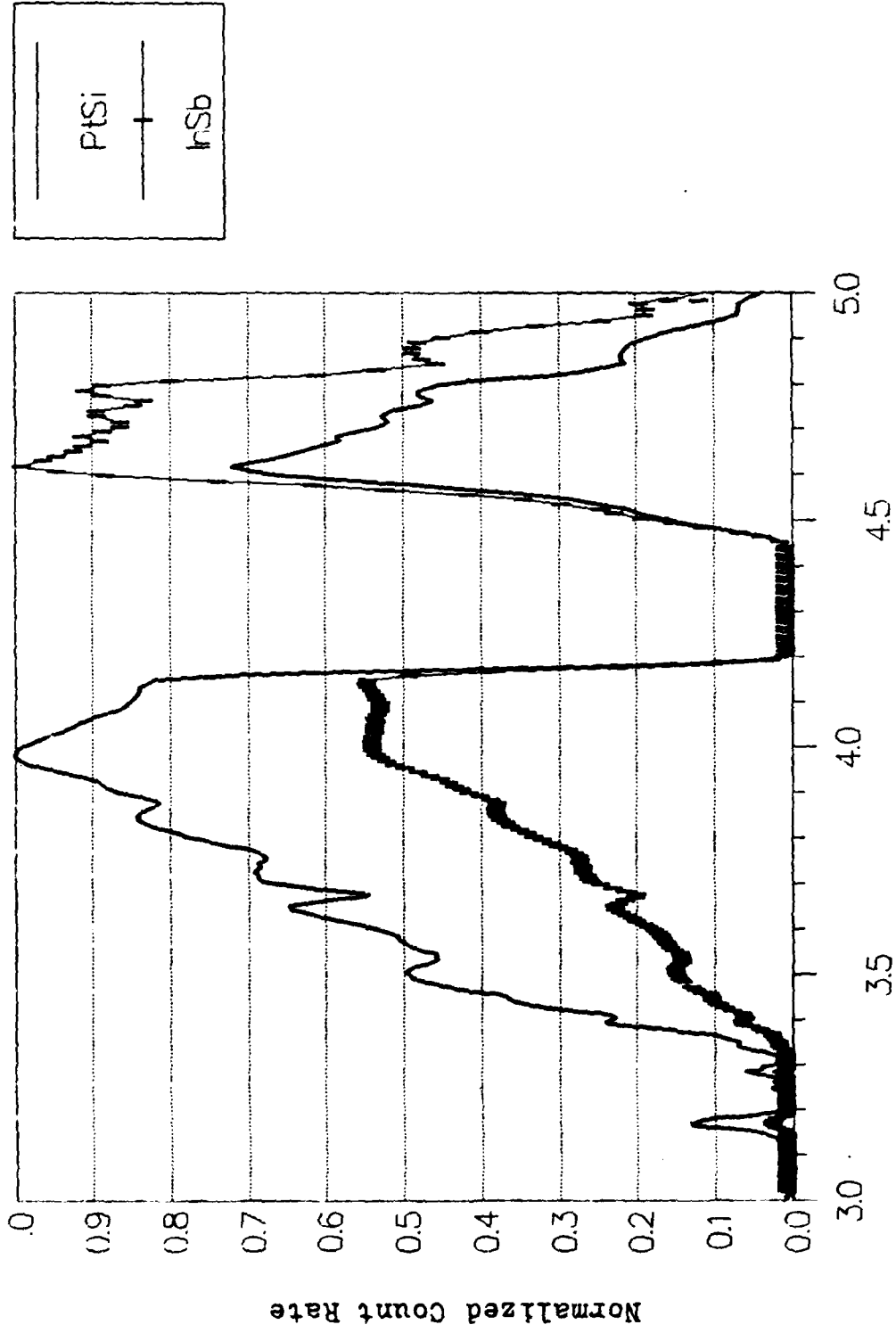


Figure A28. Night Increased Humidity Scenario, PtSi vs InSb

## Bibliography

1. Aquilera, R. "256 x 256 Hybrid Schottky Focal Plane Arrays," Proceedings of the SPIE Conference on Infrared Sensors and Sensor Fusion. 19 - 21 May 1987, Orlando, Florida. Volume 782. 108 - 113. Bellingham, Washington: SPIE, 1987.
2. Bueche, Frederick J. Schaum's Outline of Theory and Problems of College Physics (Seventh Edition). New York: McGraw-Hill Book Company, 1979.
3. Campen, C. F., Jr., et al. Handbook of Geophysics (Second Edition). New York: The Macmillan Company, 1960.
4. Cantella, Michael J. Space Surveillance Application Potential of Schottky Barrier IR Sensors. Contract F192885C0002. Lexington, Massachusetts: Lincoln Laboratory, Massachusetts Institute of Technology, 9 April 1987 (AD - A180848).
5. -----. Senior Staff Member, Space Surveillance Group. Telephone Interview. Lincoln Laboratory, Lexington, Massachusetts, 22 August 1988.
6. Dereniak, Eustace L., and Devon G. Crowe. Optical Radiation Detectors. New York: John Wiley & Sons, 1984.
7. Driscoll, Walter G. (Editor). Handbook of Optics. New York: McGraw-Hill Book Company, 1978.
8. Fairbridge, Rhodes W. (Editor). The Encyclopedia of Atmospheric Sciences and Astrogeology, Encyclopedia of Earth Sciences Series, Volume II. New York: Reinhold Publishing Corporation, 1967.
9. Hertling, David R., and R. C. Rearick. Real Time Math Model For Infrared. June 1983 - September 1985. Contract F300281C0185. Atlanta, Georgia: Georgia Institute of Technology, January 1986 (AD - A168133).
10. Hines, C. O., et al. Physics of the Earth's Upper Atmosphere. Englewood Cliffs, New Jersey: Prentice-Hall, Inc., 1965.

11. Hudson, Richard D., Jr., and Jacqueline W. Hudson. "The Military Applications of Remote Sensing By Infrared." Proceedings of the IEEE. Volume 63. 104 - 128. New York: IEEE Press, 1975.
12. Joyce, Richard R. "Indium Antimonide Detectors for Ground-Based Astronomy," Proceedings of the SPIE Conference on Infrared Detectors. 25 - 26 August 1983, San Deigo, California. Volume 443. 50 - 58. Bellingham, Washington: SPIE, 1984.
13. Kneizys, F. X., et al. Atmospheric Transmittance/Radiance: Computer Code LOWTRAN 6. Hanscom AFB, Massachusetts: Air Force Geophysics Laboratory, 1 August 1983 (AD - A137786).
14. Kosonocky, Walter F., and Hamam Elabd. "Schottky - Barrier Infrared Charge - Coupled Device Focal Plane Arrays," Proceedings of the SPIE Conference on Infrared Detectors. 25 - 26 August 1983, San Deigo, California. Volume 443. 50 - 58. Bellingham, Washington: SPIE, 1984.
15. Lange, Maj James J., and Lt Col Howard E. Evans. Class handout distributed in PHYS 521, Space Surveillance. School of Engineering, Air Force Institute of Technology (AU), Wright - Patterson AFB, Ohio, May 1985.
16. Lintz, Joseph, Jr., and David S. Simonett. Remote Sensing of Environment. Reading, Massachusetts: Addison-Wesley Publishing Company, Inc., 1976.
17. McKinnon, George P. (Editor). Fire Protection Handbook (Fourteenth Edition). Boston: National Fire Protection Association, 1976.
18. Mooney, Jonathan M., et al. "PtSi Internal Photoemission; Theory and Experiment," Proceedings of the SPIE Conference on Infrared Sensors and Sensor Fusion. 19 - 21 May 1987, Orlando, Florida. Volume 782. 108 - 113. Bellingham, Washington: SPIE, 1987.

19. Pellegrini, P. W., et al. "A Comparison of Iridium Silicide and Platinum Silicide Photodiodes," Proceedings of the SPIE Conference on Infrared Sensors and Sensor Fusion. 19 - 21 May 1987, Orlando, Florida. Volume 782. 108 - 113. Bellingham, Washington: SPIE, 1987.
20. Richards, W. G., and P. R. Scott. Structure and Spectra of Molecules. New York: John Wiley & Sons, 1985.
21. Roberts, C. Grady. "HgCdTe Charge Transfer Device Focal Planes," Proceedings of the SPIE Conference on Infrared Detectors. 25 - 26 August 1983, San Deigo, California. Volume 443. 50 - 58. Bellingham, Washington: SPIE, 1984.
22. Sabins, Floyd F., Jr. Remote Sensing, Principles and Interpretation. New York: W. H. Freedman & Company, 1987.
23. Shepherd, Freeman D., Jr. "Schottky Diode Based Infrared Sensors," Proceedings of the SPIE Conference on Infrared Detectors. 25 - 26 August 1983, San Deigo, California. Volume 443. 50 - 58. Bellingham, Washington: SPIE, 1984.
24. Touloukian, Y. S., et al. Thermal Radiative Properties - Coatings. New York: IFI/Plenum Data Corporation, 1972.
25. Sutton, George, P. Rocket Propulsion Elements, An Introduction to the Engineering of Rockets (Fifth Edition). New York: John Wiley & Sons, 1985.
26. Valley, Shea L. (Scientific Editor). Handbook of Geophysics and Space Environments. New York: McGraw-Hill Book Company, 1965.
27. Wolfe, William L. (Editor). Handbook of Military Infrared Technology. Washington, D. C.: Office of Naval Research, 1978.
28. Wolfe, William L., and George J. Zissis (Editors). The Infrared Handbook. Washington, D. C.: Office of Naval Research, 1978.

Vita

Capt Neil F. Schoon was born [REDACTED]  
[REDACTED] He graduated from Manson Community High School in 1975 and received an appointment to the U. S. Air Force Academy. He graduated from the Academy in May 1979 with the degree of Bachelor of Science in Astronautical Engineering. Upon graduation, he was assigned to the Air Force Satellite Control Facility, Onizuka AFS, California. There he served as a Satellite Command Engineer, a Satellite Operations Director, and an Assistant Manager of Spacecraft Operations. In 1984, he was assigned to the Foreign Technology Division, Wright-Patterson AFB, Ohio. There he served as the Deputy Branch Chief of the Operations Analysis Branch with technical duties of determining future foreign spacecraft requirements until entering the School of Engineering, Air Force Institute of Technology in May 1987.

[REDACTED]

## REPORT DOCUMENTATION PAGE

Form Approved  
OMB No. 0704-0188

1a. REPORT SECURITY CLASSIFICATION UNCLASSIFIED		1b. RESTRICTIVE MARKINGS	
2a. SECURITY CLASSIFICATION AUTHORITY		3. DISTRIBUTION / AVAILABILITY OF REPORT Approved for public release; distribution unlimited	
2b. DECLASSIFICATION / DOWNGRADING SCHEDULE		4. PERFORMING ORGANIZATION REPORT NUMBER(S) AFIT/GSO/ENP/88D-4	
5. MONITORING ORGANIZATION REPORT NUMBER(S)		6a. NAME OF PERFORMING ORGANIZATION School of Engineering	
6b. OFFICE SYMBOL (If applicable) AFIT/ENP		7a. NAME OF MONITORING ORGANIZATION	
6c. ADDRESS (City, State, and ZIP Code) Air Force Institute of Technology Wright-Patterson AFB, Ohio 45433-6583		7b. ADDRESS (City, State, and ZIP Code)	
8a. NAME OF FUNDING / SPONSORING ORGANIZATION AF Wright Aeronautical Laboratories		8b. OFFICE SYMBOL (If applicable) AARI	
9. PROCUREMENT INSTRUMENT IDENTIFICATION NUMBER		8c. ADDRESS (City, State, and ZIP Code) Wright-Patterson AFB, Ohio 45433-6543	
10. SOURCE OF FUNDING NUMBERS		PROGRAM ELEMENT NO	
PROJECT NO		TASK NO	
WORK UNIT ACCESSION NO		11. TITLE (Include Security Classification) AN ANALYSIS OF PLATINUM SILICIDE AND INDIUM ANTIMONIDE FOR REMOTE SENSORS IN THE 3 TO 5 MICROMETER WAVELENGTH BAND	
12. PERSONAL AUTHOR(S) Neil F. Schoon, B.S., Capt, USAF			
13a. TYPE OF REPORT MS Thesis		13b. TIME COVERED FROM _____ TO _____	
14. DATE OF REPORT (Year, Month, Day) 1968 December		15. PAGE COUNT 115	
16. SUPPLEMENTARY NOTATION			
17. COSATI CODES		18. SUBJECT TERMS (Continue on reverse if necessary and identify by block number)	
FIELD	GROUP	SUB-GROUP	Infrared Detection Indium Antimonides Infrared Surveillance Infrared Reconnaissance
17	05	01	
19. ABSTRACT (Continue on reverse if necessary and identify by block number)  Thesis Advisor: James J. Lange, Maj, USAF Adjunct Professor Department of Engineering Physics			
20. DISTRIBUTION / AVAILABILITY OF ABSTRACT <input checked="" type="checkbox"/> UNCLASSIFIED/UNLIMITED <input type="checkbox"/> SAME AS RPT. <input type="checkbox"/> DTIC USERS		21. ABSTRACT SECURITY CLASSIFICATION UNCLASSIFIED	
22a. NAME OF RESPONSIBLE INDIVIDUAL James J. Lange, Maj, USAF		22b. TELEPHONE (Include Area Code) (513) 255-6144	
		22c. OFFICE SYMBOL AFWAL/AART	

Approved for release in  
accordance with AFR 190-1  
12 Jan 1989  
S. J. Lawrence

UNCLASSIFIED

Platinum Silicide and Indium Antimonide are compared as detector materials in a space based remote sensor using the 3 to 5 micrometer wavelength band. The comparison is based on a scaled count rate involving the material's quantum efficiency, a target's reflected solar and thermal emittances, the atmospheric transmission, and the wavelength. The comparison is made using a baseline scenario and seven sensitivity analysis scenarios. The baseline scenario uses a target at 298°K and a vertical line-of-sight from the target to the remote sensor in space. The atmospheric transmission is calculated using the 1962 U. S. Standard atmospheric model resident in LOWTRAN 6, with a 23 kilometer rural visibility and no cloud cover. A sensitivity analysis was performed by varying the target temperature, target reflectance, and finally the atmospheric properties.

UNCLASSIFIED